Doshisha University
Graduate School of Science and Engineering

Spectroscopy Study of Hydrogen Particle Reflection at Helium-Induced Fuzzy Tungsten Surface

Kenta Doi

Submitted in part fulfilment of the requirements
for the degree of Doctor of Engineering at
Doshisha Univeristy, November 2017

Synopsis

In this study, the author developed a measurement technique to detect hydrogen atoms reflected from a metal surface based upon the Doppler-spectroscopy of hydrogen Balmer-α (Hα) emission. The developed measurement technique is a promising method to investigate the hydrogen particle reflection properties in low incident particle energy range, which has been considered difficult. The author applied the developed method into practice to clarify the effects of helium (He) induced tungsten (W) surface nanostructure upon the low energy hydrogen particle reflection.

Hydrogen particle reflection property at divertor plates is one of the important parameters to determine the fusion reactor operational performance. The velocity distribution of the reflected particles and reflection coefficients are tabulated for several computational studies such as the boundary-plasma models. The ITER (International Thermonuclear Experimental Reactor) organization has announced the use of W as the divertor material. While plasma-wall interaction between hydrogen plasma and W has been one of the main research topics for last several decades, very few experimental data on the reflection properties of hydrogen particle at the W wall have been collected especially in low incident particle energy range; numerical simulations only provide the database of the reflection coefficients and velocity distributions in low particle energy range. Recently, He-plasma bombardment on a W target maintained at high surface temperature of above 1000 K was found to result in the formation of a surface nanostructure – so-called W-fuzz. The W-fuzz is literally observed as fuzz-like fibriform structure. Fusion reactor operations can potentially satisfy the condition for the formation of W-fuzz on the divertor surface. To date, the effects of the W-fuzz formation upon the W sputtering yield have been reported. However, no literature can still be found for its effects upon the particle reflection.

So far, the measurements of energy and angular distributions of the reflected particles at a solid surface relies on the particle method where an ion beam at kinetic energy larger than 1 keV is injected onto a sample surface and a magnetic momentum analyzer detects the ions reflected from the sample surface. This study clarified a decrease of ion reflection coefficient due to the W-fuzz surface structure by applying the particle method based upon an ion beam based test stand apparatus. A W-fuzz sample reduced the ion reflection coefficient by 1/3 of that of a flat reference W sample without any surface structure. The measurements were performed under the injection of hydrogen (H^+) ions at kinetic

energy of 1 keV onto the W samples. In reality, however, the kinetic energy of particles incident onto the divertor plates is expected to be below several 100 eV. The particle method cannot be applied to the measurement of particle reflection properties in this low energy range due to the low ion beam transport efficiency. Ion beams diverge due to the space-charge effects; thus the ion beam flux is barely maintained for accurate reflected ion property measurements at low particle energy. In addition, most of particles are known to be reflected from a metal surface as neutrals, which may affect the divertor plasma condition more largely than reflected particles in the form of ions. Indeed, it has been reported that neutral hydrogen atoms reflected from the divertor potentially heat the boundary plasma by carrying the energy from the sheath. Data on properties of reflected particles in the form of neutrals need to be collected sufficiently.

In this study, the author proposes a spectroscopic-measurement technique to detect the reflected atoms from a plasma-facing solid wall surface in low incident particle energy range. A high resolution optical spectrometer observes a Doppler-broadened spectral component of Hα emissions originating from the reflected atoms. The spectroscopy is performed in the vicinity of a target surface under magnetized plasma bombardment. A negative bias potential applied on the target accelerates ions incident onto the surface directly from the plasma across the sheath. This method eliminates the difficulty of low energy ion beam transport by shortening the beam transport distance. However, the spectroscopic method accompanies another problem of low signal-to-noise ratio due to large background signals from the plasma. Background emissions due to the plasma excitation erase the extremely faint signal of the reflected atoms. The observation at the plasma-peripheral region, outside of the magnetized plasma column, was found to significantly enhance the signal-to-noise ratio by reducing the large background. The reflected hydrogen atoms were found to be excited to the $n = 3$ level by collisions with local H_2 molecules when traversing plasma or plasma peripheral region after the reflection. This fact allowed for the significant signal-to-noise ratio enhancement by removing the line of sight from the plasma-existing region to the outer region. The contribution from the reflected atoms accounts for 10% of the central background peak with the line of sight at the plasma periphery, while the signals of the reflected atoms appear at bottom of the central peak with intensity only less than 1% of the central peak in the plasma existing region.

The developed measurement technique clarified that the W-fuzz also reduces the particle

reflection coefficient of hydrogen particles reflected as neutrals even in low incident particle range of 200–300 eV. The continuous plasma bombardment onto the W-fuzz samples resulted in the fuzz layer destruction. The time evolution of the Doppler-broadened Hα emission spectra was investigated during the continuous plasma bombardment. The W-fuzz sample was found to reduce the particle reflection coefficient by 1/2 of the flat W surface by comparing the Doppler-spectral intensities obtained before and after the fuzz layer destruction. In this study, the relative change in the particle reflection coefficient due to the W-fuzz was investigated as described above. On the other hand, the quantitative modeling studies require the absolute value of particle reflection coefficient as an input parameter. The hydrogen particle reflection coefficient in the absolute unit can be estimated from the observed relative change and the absolute value previously reported. For example, it is known that the hydrogen particle reflection coefficient of W for hydrogen incidence at 300 eV is $\sim$0.6. The observed relative change suggests that the W-fuzz sample reduces the hydrogen particle reflection coefficient to $\sim$0.3 at the incident particle energy of 300 eV. This estimated value can be useful information in sensitivity studies to address the effects of nanostructured W surface upon the divertor plasma condition.

要旨

本研究では、低粒子エネルギー領域における金属表面からの反射水素原子を水素原子バルマーアルファ (Hα) 発光ドップラー分光計測によって検出する実験系を構築し、ヘリウムによるタングステン表面の微細構造化が水素粒子反射特性に与える影響を調査した。 核融合炉排気系に設置されるダイバータでの水素粒子反射特性は炉の稼働性能を決定する大きな要素である。 反射粒子の速度分布関数や反射係数は境界領域プラズマモデルに入力定数として用いられる。 現在南仏カダラッシュで建設が進む国際熱核融合実験炉ITERでは、ダイバータ材料としてタングステンの使用が決定された。 水素プラズマとタングステン固体壁との相互作用に関する研究は古くから存在するが、低エネルギー領域に対しては水素粒子反射特性のデータベースは数値シミュレーションに基づいて提供されているのみである。 また、近年、ヘリウムプラズマの照射効果によってタングステン表面に微細構造物が形成されることが明らかとなった。 表面温度が1000 K以上の高温状態でヘリウムを照射すると現れるその表面構造はFuzzと名付けられ、名前の通りナノメートルサイズの繊維状の構造物が樹木状に生い茂っているような姿で観測される。 この構造物は核融合炉ダイバータ表面にも形成される可能性がある。 タングステン表面Fuzz構造化がスパッタ収率に与える影響はすぐに調査されたが、水素粒子反射特性に与える影響についてはこれまでのところ報告がない。

従来より、1 keV以上の入射エネルギーに対する反射粒子のエネルギー・角度分布計測はイオンビームを用いた実験に基づいて行われている。 イオンビームを固体試料表面に入射し、反射イオンのエネルギー・角度分布を磁気質量分析器により計測する。 本論文ではこのイオンビームに基づく計測手法を粒子法と名付ける。 本研究では、タングステン表面がFuzz構造化することによって水素イオン反射強度が低下することを粒子法により明らかにした。 1 keVの水素イオンを表面に入射した場合には、Fuzz表面構造化タングステンからの反射イオン強度は表面構造を持たないタングステンからの強度と比較して1/3程度まで低下した。 核融合炉ダイバータプラズマは数100 eV以下の比較的低温になることが予測されるが、粒子法では数100 eV以下の低エネルギー領域における計測が困難である。 低エネルギー領域ではイオンビームへの空間電荷効果が顕著になるため、十分なイオンビーム量を確保することが難しい。 加えて、金属表面に入射するイオンの大半は中性原子として反射することが知られており、主に中性反射原子が核融合炉ダイバータプラズマへ影響を与えることが予測される。実際に、ダイバータ入射時にシースで加速されたイオンが中性粒子として反射しダイバータプラズマの温度を上昇させることが報告されていることからも中性原子として反射する粒子の速度分布や反射係数を調査する必要がある。

本研究では、先ず低粒子エネルギー領域での固体壁からの中性反射原子の検出手法の開

発を行った。 磁化水素プラズマ中に負バイアスを印加した金属試料を曝し、反射原子からのHα発光スペクトルドップラー成分を検出する手法を考案した。 イオンはプラズマから直接シースを経て試料表面へ加速され入射するため、イオン輸送距離を短縮することができ、空間電荷効果によるイオンビーム発散の問題を解決することができる。 一方、反射水素原子からのHα発光は微弱であることから、背景プラズマからの高強度発光による低信号対雑音比が問題となる。 本研究ではプラズマ周辺部を観測することにより信号対雑音比を大幅に向上することに成功した。 本研究によって、反射水素原子はプラズマ周辺領域の水素分子との衝突によって$n = 3$へ励起されHα発光ドップラー成分を形成することが明らかになった。 この事実を応用し、観測視線をプラズマから外すことで背景プラズマからの信号を抑えた反射原子からの微弱信号の検出が可能となった。 反射原子からの信号は背景信号の1%未満の強度であったのに対し、本研究で開発した手法では10%程度まで向上した。

表面がFuzz構造化したタングステン試料からの水素粒子反射特性の計測を上記のHαドップラー分光計測に基づく手法で行った結果、200 - 300 eVの入射粒子エネルギー領域では、反射する水素原子の量 (粒子反射係数) が表面構造を持たないタングステンと比較して1/2程度まで減少することが明らかになった。 Fuzz表面構造化タングステン試料へのプラズマの定常照射によって、表面のFuzz層は除去される。 この事実より、照射中はHαドップラースペクトルの時間変化を計測し、Fuzz層が存在する計測開始時のスペクトル強度とFuzz層が除去された後のスペクトル強度を比較することで、粒子反射係数の低下を相対的に評価した。実際の境界領域プラズマモデルでは反射係数の絶対値が必要であるが、過去に報告されているデータから今回のFuzz試料の反射係数の絶対値を見積もることができる。表面構造を持たないタングステンからの水素粒子反射係数は数値シミュレーションにより、300 eVの水素粒子入射において~0.6ということが明らかになっている。 ここから、Fuzz試料は粒子反射係数を1/2に低下させるという実験結果を考慮して、Fuzz試料からの水素反射係数は300 eVの水素粒子入射では~0.3となることが見積もられる。 今後、この結果をもとに核融合炉ダイバータプラズマのモデル計算を行うことでダイバータ表面Fuzz層形成によるダイバータプラズマへの影響を調査することが可能になる。

Acknowledgements

I would like to express my special thanks to my supervisor, Prof. Motoi Wada, for the encouragement and guidance he has provided throughout six years since I entered Plasma Physics Laboratory in 2012. I have been extremely lucky to practice a doctrine in Plasma Physics Laboratory, where I can gain any worthwhile experiences he has prepared for me. I would also like to thank Prof. Mamiko Sasao and all the members of Plasma Physics Laboratory for the supports and worthwhile discussions.

I must express my thanks to Dr. Hitoshi Yamaoka of RIKEN SPring-8 Center. This dissertation would not have been possible without the advice and constructive discussions provided by him in spite of being extremely busy on his own research projects. I must also express my thanks to Dr. Heun Tae Lee of Osaka University. The experimental results presented in this dissertation would not have been obtained without tungsten samples provided by him.

I would like to thank Advanced Doctoral Program in Global Resource Management for providing not only the scholarship, but also opportunities to broaden my horizons throughout extremely worthwhile discussions on interdisciplinary topics with interesting people.

Thanks to my family, especially mother and father, for the support and encouragement.

Lastly but most importantly, I must express my special gratitude to my wife Satomi. Thank you always for your support, encouragement and understanding.

Contents

List of Tables

List of Figures

Chapter 1

Introduction

1.1 General Structure of a Nuclear Fusion Reactor

Over 50 years after the first concept of a nuclear fusion reactor, tokamak, was proposed, the development of fusion power plants now progresses to the phase of technical verification [1]. The ITER (International Thermonuclear Experimental Reactor) project [2] involves international cooperation among seven members – China, the European Union, India, Japan, Korea, Russia and United States to demonstrate the feasibility of fusion power. The ITER is currently under the construction in Cadarache in southern France, and the first plasma ignition is planned in the end of 2025. Finally, the project aims to produce the output power 10 times larger than the input for plasma heating throughout the deuterium-tritium (DT) plasma burning campaign to be launched in 2035.

Figure 1.1 shows the general structure of ITER [3]. The reactor mainly consists of a torus-shaped vacuum vessel and electromagnet coils. Extremely high temperature DT plasma hotter than ∼100 million kelvin is produced by plasma heating based upon microwave and neutral beam injection. The intense magnetic field produced by superconductive coils confines the heated plasma in the core region of the vacuum vessel; the magnetic confinement of the high temperature plasma prevents the wall damage due to the heat. The DT fusion reactions in the core region of the reactor produce neutrons at

the kinetic energy of 14.1 MeV as follows:

$$^{2}_{1}\mathrm{D} + ^{3}_{1}\mathrm{T} \rightarrow ^{4}_{2}\mathrm{He}\ (3.5\ \mathrm{MeV}) + ^{1}_{0}\mathrm{n}\ (14.1\ \mathrm{MeV}). \tag{1.1}$$

The blanket is designed to convert the kinetic energy of the fusion-produced neutrons into the thermal energy and to heat water in the tubes at the inside of the blanket for the power generation at steam turbines. On the other hand, the kinetic energy of the fusion-produced α particles ($^{4}_{2}$He) is delivered to the fuel DT plasma for self-sustaining fusion reactions [4, 5]. Once the fuel plasma absorbs the energy from the α particles, the low energy helium (He) particles, so-called He ash, need to be exhausted from the reactor because the accumulation of He ashes in the reactor core results in a decrease of the DT reaction rate by reducing the plasma temperature [6].

The divertor plays an important role in the efficient exhaust of impurities including the He ash by neutralizing projectiles at the surface [7, 8]. The ionized He ashes tend to accumulate in the reactor by being trapped by the magnetic field. It is known that

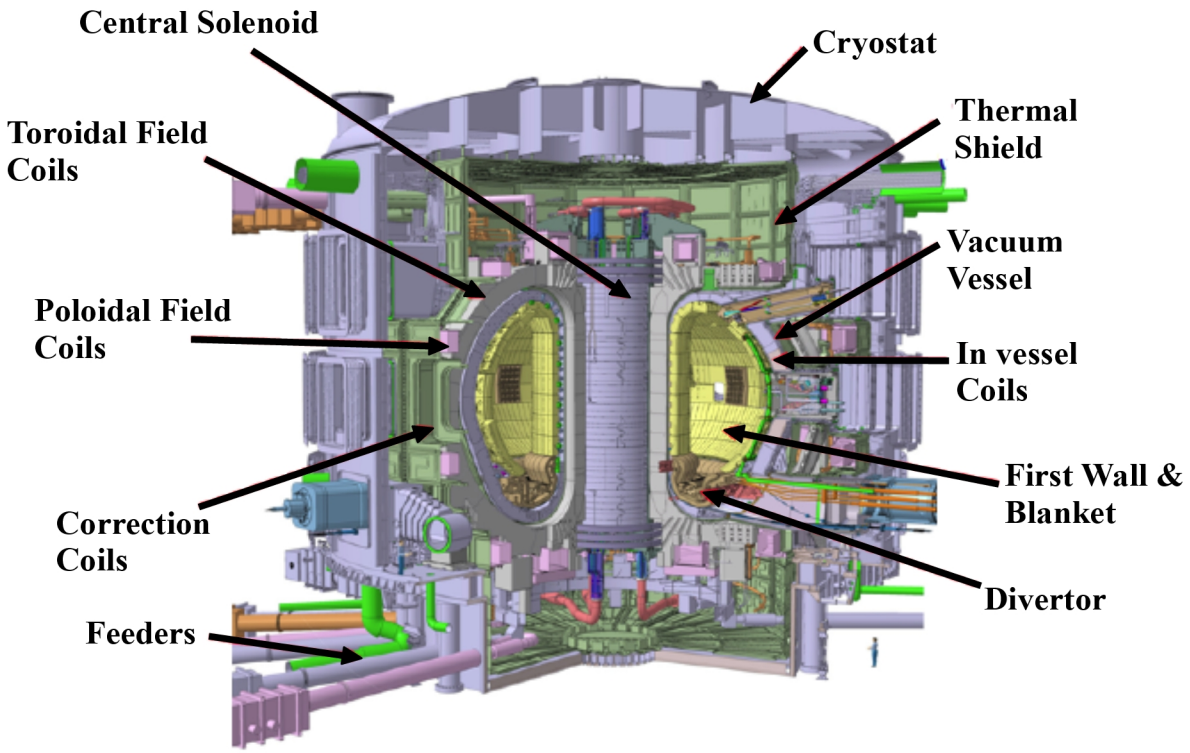

Figure 1.1. General structure of ITER. This image was originally compiled by the ITER Organization [3].

the fusion plasma periodically causes violent particle flow from the core to the divertor, so-called Edge Localized Mode (ELM) [9]. The ELM contributes to the transport of the He ashes from the core to the edge region, while there are huge concerns over the surface damage of the divertor due to the bursty thermal flux [10, 11]. The transported impurity ions including He ashes are neutralized at the divertor surface, and exhausted as neutrals from the reactor. The magnetic field is configured to guide the ionized particles to the divertor surface; the magnetic field lines intersect the divertor surfaces as shown in Fig. 1.2 [12]. The divertor surface is inclined with respect to the magnetic field in order to disperses the intense heat flux to larger area of the divertor surface. Additionally, gas impurities such as Ar, N_2 or Ne are intentionally seeded to the divertor region to reduce the heat flux by radiative cooling. The idea of the gas impurity seeded divertor is called the radiative divertor [13].

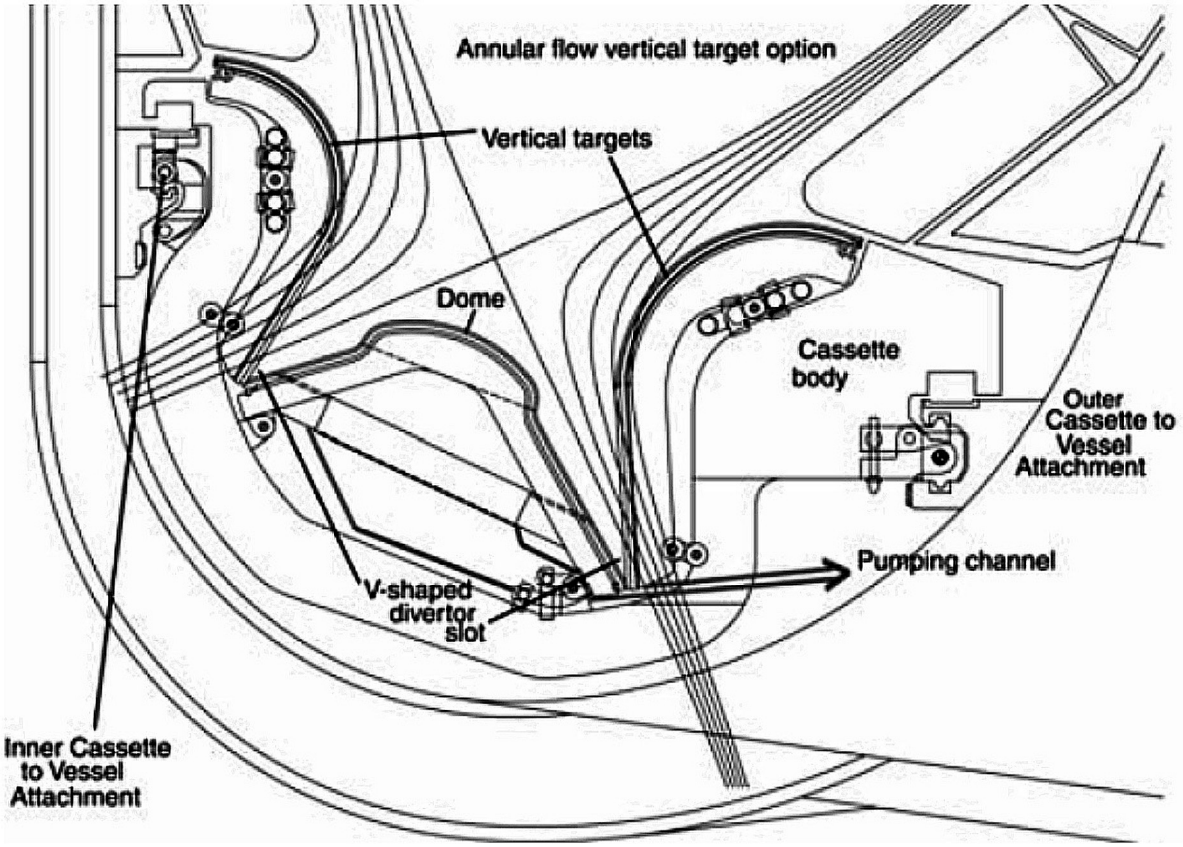

Figure 1.2. Structure of divertor and magnetic field configuration in the divertor region. The magnetic field lines are illustrated by the solid lines intersecting divertor targets. This figure was originally compiled by G Janeschitz [12].

1.2 Plasma-Wall Interaction at Divertor

When a metal surface contacts with a plasma, particles of both plasma and wall material interact with each other. This phenomenon is so-called plasma-wall interaction (PWI). As shown in Fig. 1.3, PWI involves complex particle processes. In a fusion reactor, theoretically, the divertor is the only one component directly facing the plasma. The PWI at the divertor surface determines the overall operational performance of a reactor. For example, sputtering results in the formation of impurities and damage of the divertor surface. The intrusion of the impurities into the core plasma causes a decrease of the plasma temperature by radiative cooling, which decreases the DT fusion reaction rate. Hydrogen particles reflected from divertor plates affect fundamental plasma-boundary processes including fuel recycling [14].

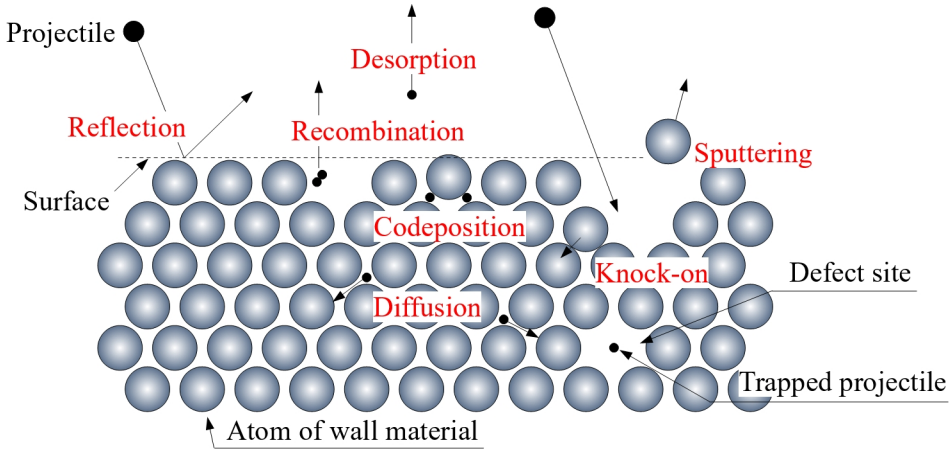

Figure 1.3. Fundamental processes in plasma-wall interaction.

Tungsten (W) is well known as a primary candidate for the divertor material because of its high melting point and low sputtering rate. The ITER organization has determined the use of full-W-divertor, in which all plasma-facing parts of the divertor are literally made of W [15]. Therefore, PWI between W and hydrogen/helium has been studied widely by many fusion researchers. It has been reported that He-plasma bombardment on W at high surface temperature potentially causes the formation of surface structures. Figure 1.4 shows the He-induced W surface structures together with corresponding He-ion bombardment conditions [16]. There are two types of He-induced W surface structures reported so far: He bubble and fibriform nanostructure so-called W-fuzz [17, 18]. The

He-ion bombardment onto W at the surface temperature higher than ∼2000 K normally results in the formation of He bubble. A SEM image of a typical He bubble structure is given in Fig. 1.4(b)-(iv). On the other hand, the He-ion bombardment at lower surface temperature of 1000 - 2000 K forms the W-fuzz nanostructure as shown in Fig. 1.4(b)-(ii). Figure 1.4(c) shows a cross-sectional image of a W-fuzz surface observed by a TEM. Fibriform nanostructures of several dozen nanometer in diameter are fuzzily localized in the surface layer. These W surface structures are potentially formed on the divertor surface because the normal reactor operation can satisfy the conditions for the surface structure formation shown in Fig. 1.4(a). The particle energy in the divertor region is expected to be below several 100 eV. In spite of massive efforts on the heat management including the radiative plasma cooling with seeded gas and a well-designed water-cooling system,

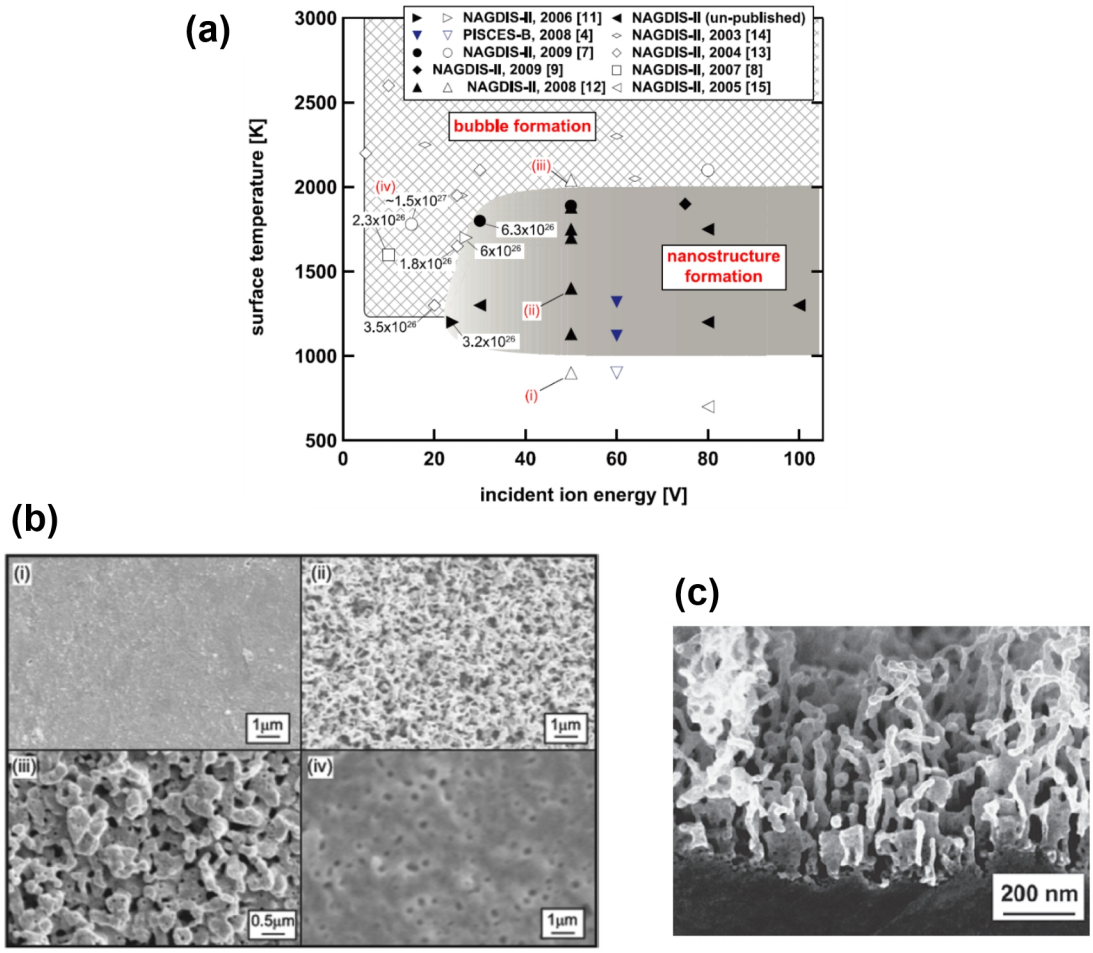

Figure 1.4. W surface structures formed by He-ion bombardment: (a) Conditions for the formation of He bubble and W-fuzz surface structures and (b) SEM images of corresponding surface structures. (c) A TEM cross-sectional image of a W-fuzz surface. All images here were originally compiled by S Kajita [16].

the surface temperature of the W divertor plate surface can be increased high enough for the nanostructure formation due to the high heat flux from the plasma estimated to be up to 20 MWm^{-2} in the ITER nuclear burning operation [15, 19]. Expectedly, the surface-structure formation on the divertor surface would change the properties of PWI processes. To date, the effects of the W-fuzz surface upon the sputtering yield have been examined. It has been reported that the W-fuzz surface reduces the sputtering yield [20]. On the other hand, no literature has reported its effects upon the particle reflection so far.

1.3 Scope of This Study

The particle reflection property at the W divertor plate has been one of the main research topics in the fusion research community because it determines terms for fusion reactor operational performance [14]. Energy and particle reflection coefficients of hydrogen particles are tabulated for several computational studies such as the edge-plasma simulation models, hydrogen recycling and impurity transport analysis [21]. So far, the hydrogen reflection at a flat W without any surface structure has been investigated widely by both experiments and numerical simulations [22, 23]. However, very few data exist for hydrogen reflection at plasma-modified surfaces including W-fuzz and He-bubble. This work aims to develop a measurement technique for the hydrogen reflection in low incident particle energy range and to clarify the effects of the W surface morphology upon the low energy hydrogen reflection.

To date, the measurement of the particle reflection properties relies on the particle method using ion beam based test stand apparatuses [24], where an ion sensitive detector is employed to detect reflected hydrogen ions (both H^+ and H^-) produced by H^+ ion beam injection onto a solid sample. In this study, the hydrogen ion reflection at W including samples with He-induced surface structures was investigated at the incident particle energy of 1 keV by utilizing the particle method (refer to Chapter 3 and Chapter 4 about the general structure of the ion beam based test stand apaaratus and the experimental results, respectively) [25]. However, the space charge effect on the ions restricts the ion beam transport especially in low energy; the low energy ion beam diverges during the transport.

The experimental investigation using the ion beam apparatus is limited in relatively high incident particle energy range larger than 1 keV.

The experimental characterizations of the reflected neutral particles at lower incident energy are indispensable because most of particles are backscattered at a metal surface as neutral atoms [26, 27], and the energy of the incident particles onto the divertor is expected to be lower than several 100 eV. It is known that neutral hydrogen particles reflected from the divertor plates can heat the edge-plasma by carrying the energy from the sheath [28]. The edge-plasma heating due to the energetic reflected particles strongly influences the plasma-boundary conditions, which in turn affects all the boundary processes including sputtering. Such effects are considered especially important in ITER because of the anticipated strong ion-neutral coupling effects due to the large incident ion flux. In this study, a new measurement technique based upon Doppler spectroscopy of hydrogen Balmer-α (Hα) emission is proposed for the experimental characterizations of the low energy neutral hydrogen atoms reflected at a metal surface. A metal target is inserted into a magnetized hydrogen plasma, and a high resolution optical spectrometer observes the Doppler-broadened Hα emission spectra originating from the reflected hydrogen atoms. A negative bias applied onto the target in the plasma controls the incident ion energy; H^+ ions in the plasma are accelerated across the sheath. The ion acceleration in the short distance of sheath can minimize the space-charge effect on the incident ions. The developed measurement technique was applied to the experimental investigation of the effects of the W surface morphology, *i.e.*, W-fuzz, upon the hydrogen reflection in the incident particle energy range less than 300 eV.

Later in Chapter 2, the fundamental processes in plasma-wall interaction are summarized. Chapter 3 provides the detailed structure of the ion beam based test stand apparatus used for the measurements of hydrogen ion reflection properties. Chapter 4 discusses the experimental results of the hydrogen ion reflection at W surfaces measured by the particle method using the ion beam based test stand apparatus. From the measurements based on the particle method, it has been clarified that the W-fuzz surface reduces the hydrogen ion reflection coefficient. Before starting the discussion on the Doppler-spectroscopic

measurement of hydrogen reflection, the fundamentals required to understand the optical spectroscopic measurement are given in Chapter 5 and Chapter 6. Chapter 5 gives the physics of light emissions in plasma, and Chapter 6 describes the basic principles of optical spectrometers. Chapter 7 provides the details on a magnetized plasma bombardment device designed for the Doppler-spectroscopic measurement together with the plasma parameter characterizations. Chapter 8 introduces the newly developed measurement technique based upon the Doppler spectroscopy of Hα emission. Chapter 9 discusses the properties of hydrogen atoms reflected from the W-fuzz surface investigated by the spectroscopic measurement method. Finally, Chapter 10 provides the conclusions.

References

[1] G. Brumfiel, "Just around the corner," *Nature*, vol. 436, no. 7049, pp. 318–320, Jul. 2005.

[2] N. Holtkamp, "An overview of the ITER project," *Fusion Eng. Des.*, vol. 82, no. 5-14, pp. 427–434, Oct. 2007.

[3] ITER Organization, *ITER 2009 Baseline: Plant Description (PD)*, R. Reichle and J. How, Eds., ITER Organization, Route de Vinon-sur-Verdon, St. Paul-lez-Durance Cedex, France, Oct. 2009.

[4] Ya. I. Kolesnichenko, "The role of alpha particles in tokamak reactors," *Nucl. Fusion*, vol. 20, no. 6, pp. 727–780, Jun. 1980.

[5] S. J Zweben, R. V. Budny, D. S Darrow, S. S. Medley, R. Nazikian, B. C. Stratton, E. J. Synakowski, and G. Taylor for the TFTR Group, "Alpha particle physics experiments in the Tokamak Fusion Test Reactor," *Nucl. Fusion*, vol. 40, no. 1, pp. 91–149, Jan. 2000.

[6] D. Reiter, H. Kever, G. H. Wolf, M. Baelmans, R. Behrisch, and R. Schneider, "Helium removal from tokamaks," *Plasma Phys. Controlled Fusion*, vol. 33, no. 13, pp. 1579–1600, Nov. 1991.

[7] R. Parker, G. Janeschitz, H. D. Pacher, D. Post, S. Chiocchio, G. Federici, and P. Ladd, "Plasma-wall interactions in ITER," *J. Nucl. Mater.*, vol. 241-243, pp. 1–26, Feb. 1997.

[8] A. S. Kukushkin, H. D. Pacher, V. Kotov, G. W. Pacher, and D. Reiter, "Finalizing the ITER divertor design: The key role of SOLPS modeling," *Fusion Eng. Des.*, vol. 86, no. 12, pp. 2865–2873, Dec. 2011.

[9] H. Zohm, "Edge localized modes (ELMs)," *Plasma Phys. Controlled Fusion*, vol. 38, no. 2, pp. 105–128, Feb. 1996.

[10] H. Zohm, "The physics of edge localized modes (ELMs) and their role in power and particle exhaust," *Plasma Phys. Controlled Fusion*, vol. 38, no. 8, pp. 1213–1223, Aug. 1996.

[11] J. W. Connor, "A review of models for ELMs," *Plasma Phys. Controlled Fusion*, vol. 40, no. 2, pp. 191–213, Feb. 1998.

[12] G. Janeschitz, A. Antipenkov, G. Federici, C. Ibbott, A. Kukushkin, P. Ladd, E. Martin, and R. Tivey, "Divertor design and its integration into ITER," *Nucl. Fusion*, vol. 42, no. 1, pp. 14–20, Jan. 2002.

[13] B. J. Braams, "Radiative Divertor Modelling for ITER and TPX," *Contrib. Plasma Phys.*, vol. 36, no. 2-3, pp. 276–281, 1996.

[14] E. Vietzke, M. Wada, and M. Hennes, "Reflection and Adsorption of Hydrogen Atoms and Molecules on Graphite and Tungsten," in *Hydrogen Recycling at Plasma Facing Materials*, C. H. Wu, Ed., Dordrecht: Kluwer Academic, 2000, pp. 51–58.

[15] R. A. Pitts, S. Carpentier, F. Escourbiac, T. Hirai, V. Komarov, S. Lisgo, A. S. Kukushkin, A. Loarte, M. Merola, A. Sashala Naik, R. Mitteau, M. Sugihara, B. Bazylev, and P. C. Stangeby, "A full tungsten divertor for ITER: Physics issues and design status," *J. Nucl. Mater.*, vol. 438, pp. S48–S56, Jul. 2013.

[16] S. Kajita, W. Sakaguchi, N. Ohno, N. Yoshida, and T. Saeki, "Formation process of tungsten nanostructure by the exposure to helium plasma under fusion relevant plasma conditions," *Nucl. Fusion*, vol. 49, no. 9, p. 095005, Sep. 2009.

[17] M. Y. Ye, S. Takamura, and N. Ohno, "Study of hot tungsten emissive plate in high heat flux plasma on NAGDIS-I," *J. Nucl. Mater.*, vol. 241-243, pp. 1243–1247, Feb. 1997.

[18] S. Takamura, N. Ohno, D. Nishijima, and S. Kajita, "Formation of Nanostructured Tungsten with Arborescent Shape due to Helium Plasma Irradiation," *Plasma Fusion Res.*, vol. 1, p. 051, Oct. 2006.

[19] H. D. Pacher, A. S. Kukushkin, G. W. Pacher, V. Kotov, and D. Reiter, "Modelling of the ITER reference divertor plasma," *J. Nucl. Mater.*, vol. 415, pp. S492–S496, Aug. 2011.

[20] D. Nishijima, M. J. Baldwin, R. P. Doerner, and J. H. Yu, "Sputtering properties of tungsten 'fuzzy' surfaces," *J. Nucl. Mater.*, vol. 415, pp. S96–S99, Aug. 2011.

[21] D. M. Manos and G. M. McCracken, "Probes for Plasma Edge Diagnostics in Magnetic Confinement Fusion Devices," in *Physics of Plasma-Wall Interactions in Controlled Fusion*, D.E. Post and R. Behrisch, Eds., New York, London: Plenum Press, 1984, pp. 135–209.

[22] W. Eckstein and H. Verbeek, "Reflection of light ions from solids," *Nucl. Fusion*, vol. 24, pp. S12–S28, 1984.

[23] W. Eckstein, "Reflection," *IPP-REPORT*, IPP 17/12, Aug. 2009.

[24] S. Kato, N. Tanaka, M. Sasao, M. Kisaki, K. Tsumori, M. Nishiura, Y. Matsumoto, T. Kenmotsu, M. Wada, H. Yamaoka, "Angle-resolved intensity and energy distributions of positive and negative hydrogen ions released from tungsten surface by molecular hydrogen ion impact," *J. Nucl. Mater.*, vol. 463, pp. 351–354, Aug. 2015.

[25] K. Doi, Y. Tawada, H. T. Lee, S. Kato, N. Tanaka, M. Sasao, M. Kisaki, M. Nishiura, Y. Matsumoto, T. Kenmotsu, M. Wada, Y. Ueda, and H. Yamaoka, "Reflection properties of hydrogen ions at helium irradiated tungsten surfaces," *Phys. Scripta*, vol. T167, p. 014044, Jan. 2016.

[26] W. Eckstein, F. E. P. Matschke, and H. Verbeek, "Reflection of hydrogen from stainless steel and Nb," *J. Nucl. Mater.*, vol. 63, pp. 199–204, Dec. 1976.

[27] R. S. Bhattacharya, W. Eckstein, and H. Verbeek, "Positive charge fractions of H, D, and He backscattered from solid surfaces," *Surf. Sci.*, vol. 93, no. 2-3, pp. 563–581, Mar. 1980.

[28] A. E. Shumack, "The influence of electric fields and neutral particles on the plasma sheath at ITER divertor conditions," Ph.D. dissertation, Eindhoven University of Technology, Jan. 2011.

Chapter 2

Fundamental Processes in Plasma-Wall Interaction

2.1 Sheath Formation

A contact of plasma to a solid material forms a region with an electrical-potential gradient between the quasineutral plasma body and the negatively charged wall surface – so-called the plasma sheath. The plasma shields the wall potential in a relatively short distance of the plasma sheath due to the positive space charge formed by positive ions attracted to the wall vicinity. The sheath thickness approximates several times of the Debye length, $\lambda_D = \sqrt{\epsilon_0 k_B T_e/(n_0 e^2)}$, where ϵ_0 is the vacuum permittivity; k_B is Boltzmann's constant; e is the electron charge; T_e is the electron temperature; and n_0 is the electron density in the quasi-neutral plasma. The Child-Langmuir law gives the analytical formula for the sheath thickness [1, 2, 3]:

$$d = \frac{2^{5/4}}{3} \left(\frac{e\varphi_w}{k_B T_e} \right)^{3/4} \lambda_D, \tag{2.1}$$

where φ_w is the absolute value of the negative bias potential of the wall. For example, the sheath thickness is calculated to be ~ 0.5 mm for the negative biased wall at -300 V in a plasma with $n_0 = 4 \times 10^{11}$ cm^2 and $T_e = 3.0$ eV, where the plasma parameter given above represents the actual values measured in the magnetized hydrogen plasma used for the Doppler-spectroscopic measurements of the hydrogen reflection in this study.

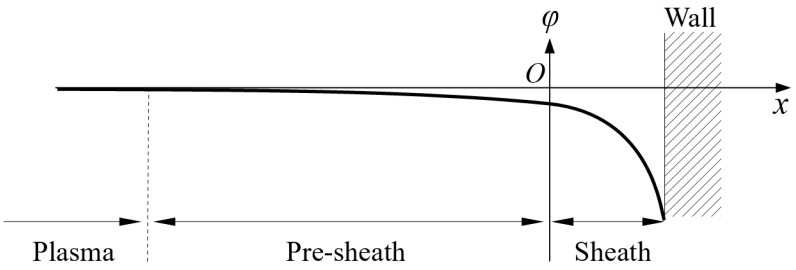

Figure 2.1. Electric-potential curve in the vicinity of a plasma-facing wall surface.

One has to note that Eq. 2.1 is only valid for a collisionless sheath. A schematic model of the potential distribution in the vicinity of a negatively charged plasma-facing wall is illustrated in Fig. 2.1. The potential in the vicinity of the wall surface is given by φ as a function of x. The potential φ monotonically increases in the sheath and finally reaches the quasi-neutral ($\varphi \approx 0$) in the region sufficiently far from the wall. The transition point from non-neutral to quasi-neutral ($x = 0$ in Fig. 2.1) is called the sheath edge. In the region toward the plasma from the sheath edge ($x < 0$), a potential gradient of the order of $|k_B T_e/e|$ exists with longer spatial scale compared to the sheath. This region is so-called presheath. The ions enter the sheath at the ion acoustic velocity, $c_s = \sqrt{k_B T_e/m_i}$, due to the acceleration in the presheath. Alternatively, the ion acoustic velocity is called the Bohm velocity. In energy units, the Bohm velocity corresponds to the half energy of the electron temperature because $m_i {c_s}^2/2 = k_B T_e/2$. The ions entering the sheath from the plasma are actually required to have velocity higher than the Bohm velocity for the stable sheath formation. This requirement is called the Bohm criterion [4, 5].

2.2 Particle Reflection

Ions in a plasma are accelerated across the sheath and incident onto the wall surface with kinetic energy given by the sheath potential gradient. The particle reflection is defined as the direct emission of the incident particles from the solid surface, where the backscattering of the particles takes place in extremely short duration of time. It is known that most of the incident ions are backscattered from the surface as neutral atoms due to the recombination with electrons in the solid material. The proportion of reflected particles in the form of neutral atoms is especially high in low incident particle energy

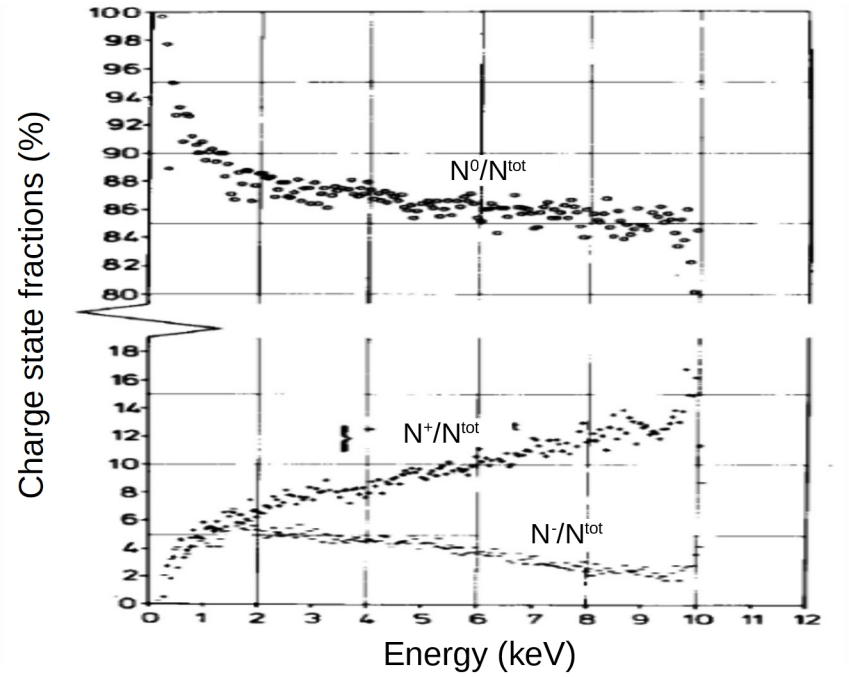

Figure 2.2. Measured charge-state fractions of hydrogen particles reflected from stainless steel under the hydrogen ion (H^+) bombardment at the incident particle energy of 10 keV. This graph was originally compiled by W Eckstein [6].

range. Eckstein *et al.* measured the charge-state fractions of hydrogen particles reflected at stainless steel with hydrogen ion incidence at 10 keV [6]. As shown in Fig. 2.2, more than 90% of the reflected hydrogen particles at low energy less than 1 keV was in the form of neutral atoms, while the reflected neutral atoms still accounted for approximately 85% of the total reflected particles including both negative and positive ions even at ∼10 keV.

The particle reflection is often characterized by two parameters: the particle reflection coefficient R_N and the energy reflection coefficient R_E [7, 8]. The particle reflection coefficient R_N is simply defined as the ratio of the number of particles reflected from the solid surface against the total number of the incident particles:

$$R_N(E_0, \alpha) = \frac{N}{N_0} = \frac{1}{N_0} \int_0^{E_0} dE \int_0^{\pi/2} d\beta \int_0^{2\pi} d\varphi W_r(E_0, \alpha; E, \beta, \varphi) \sin\beta. \tag{2.2}$$

Here α, β and φ represent angles of the incident and reflected particles. As defined in Fig. 2.3, α and β denote the incident and reflection angles with respect to the surface normal, while φ represents the azimuthal angle of the reflected particle. The function in the right side of Eq. 2.2, $W_r(E_0, \alpha; E, \beta, \varphi)$, is the energy distribution function of the

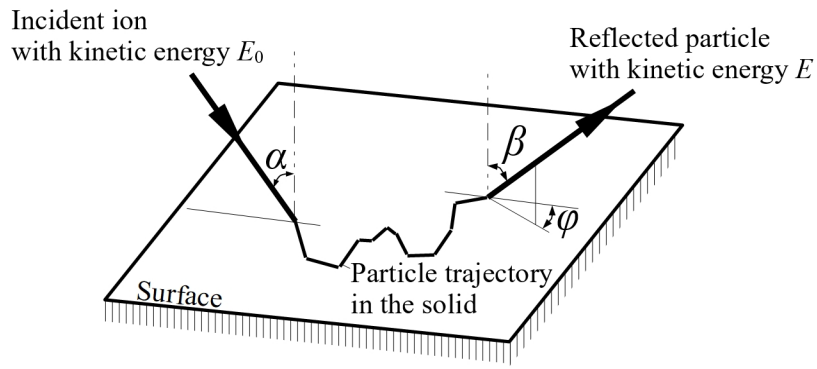

Figure 2.3. Schematic image of particle reflection at a solid surface and definition of angles.

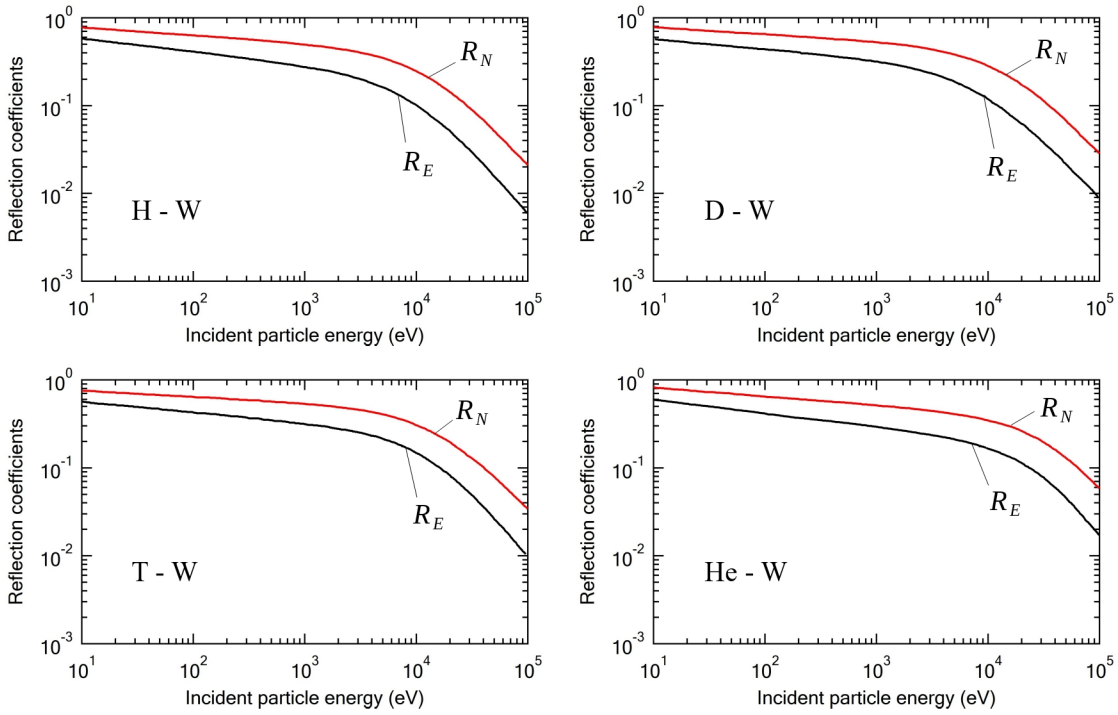

Figure 2.4. Incident particle energy dependence of particle and energy reflection coefficients for several projectile species on W target. These data were compiled by W Eckstein [9] and digitized from Ref. [9].

reflected particle in a unit solid angle, where E and E_0 represent energy of a reflected particle and that of incident particles, respectively. The energy reflection coefficient R_E is defined as the ratio of the average energy of the reflected particles to the incident particle energy:

$$R_E(E_0, \alpha) = \frac{< E_{out} >}{E_0} = \frac{1}{E_0} \int_0^{E_0} dE \int_0^{\pi/2} d\beta \int_0^{2\pi} d\varphi E \cdot W_r(E_0, \alpha; E, \beta, \varphi) \sin\beta. \quad (2.3)$$

To date, data on particle reflection at a flat target surface without any surface structure have been collected widely by numerical simulations. Figure 2.4 shows the incident particle energy dependence of particle and energy reflection coefficients for several species on W target. Graphs in Fig. 2.4 were obtained from line fittings to the calculated values [9]. The reflection coefficients monotonically decrease with increasing the incident particle energy. This trend can be explained by the deeper penetration depth of the projectiles with higher incident particle energy. These high energy particles barely reach the surface again after the penetration into deeper layer compared to lower energy particles.

2.3 Particle Sputtering

Once a projectile enters the inside of a solid wall material, it collides with the constituent atoms of the material by drawing characteristic trajectories. If the colliding projectile has high energy enough to overcome the binding energy of the constituent atom in the material, the target atoms can be sprung out from its original position. The resultant free energetic target atom collides with neighboring target atoms, resulting in the physical sputtering as shown in Fig. 2.5(a). The trajectories of the atoms in the solid material is called collision cascade. Additionally, the projectile itself can also contribute to the physical sputtering by colliding with the target atom in the surface layer as shown in Fig. 2.5(b). The physical sputtering of a material is characterized by sputtering yield defined as ratio of the number of sputtered particles against that of incident particles:

$$Y(E_0, \alpha) = \frac{1}{N_0} \int_0^{E_0} dE \int_0^{\pi/2} d\beta \int_0^{2\pi} d\varphi \sin\beta W_s(E_0, \alpha; E, \beta, \varphi), \tag{2.4}$$

where N_0 is the total number of the incident particle; and $W_s(E_0, \alpha; E, \beta, \varphi)$ is the energy distribution function of the sputtered particle in a unit solid angle. The angles α, β and φ are defined in the same manner as in the reflection as shown in Fig. 2.3.

Figure 2.6 shows energy dependence of sputtering yields of several projectile species on W target reported so far. The data lines in Fig. 2.6 were obtained from fittings to the calculated values [10]. At incident particle energy lower than threshold, no sputtering

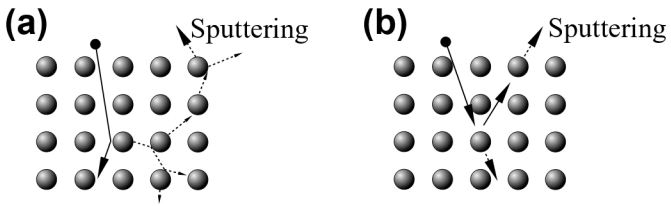

Figure 2.5. Possible collision cascades of a projectile in a solid target resulting in sputtering.

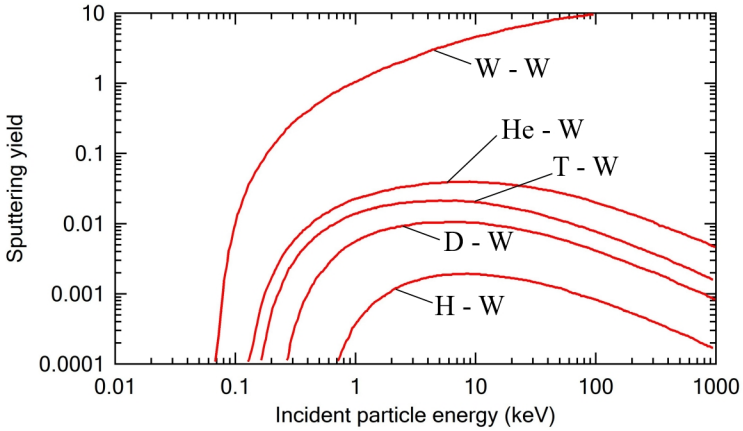

Figure 2.6. Incident particle energy dependence of sputtering yields for several projectile species on W target. These data were compiled by W Eckstein [10] and digitized from Ref. [10].

takes place because the surface binding energy cannot be overcome. The sputtering yield tends to increase with increasing the incident particle energy higher than the threshold. Once it takes the maximum at certain incident particle energy, large penetration depth of the incident particle at higher energy reduces the sputtering yield since the collision cascade is drawn in deeper layer. Previously, the threshold energy of the sputtering for W at normal incidence of hydrogen was estimated to be 443 eV [11], and the incident angle dependence was found small [12]. Several analytical formulas for the sputtering threshold energy under theoretical or fitting treatments are summarized in Ref. [12]. In this study, hydrogen (H^+) ions at kinetic energy less than 1 keV were injected onto W targets for the particle reflection measurements, where the sputtering effect upon the surface morphology was negligible. As shown in Fig. 2.6, the sputtering yield of W for hydrogen (H) particle injection is less than 1×10^{-3} in the incident particle energy range less than 1 keV. One has to note that the Doppler-spectroscopy study of hydrogen reflection was performed in the incident hydrogen particle energy range less than 300 eV, which is actually under the

threshold energy for W sputtering.

There is another particle sputtering mechanism resulted from chemical reaction – so-called chemical sputtering. Chemical sputtering does not take place in PWI of a non-reactive combination of species such as hydrogen and W. However, this effect is important for a reactive combination of species such as hydrogen and graphite, involving the formation of hydrocarbon such as methane. Since chemical sputtering is caused by the chemical reaction on the surface, the sputtering yield does not depend largely on the incident particle energy. It is known that the surface temperature and the particle flux play an important role to determine the sputtering yield [13, 14].

2.4 Particle Diffusion in Wall Material

Once the incident particles reach the maximum depth of the penetration in the wall material, the particles thermally diffuse around the inside of the target material. The particle diffusivity in a solid material exhibits the exponential dependence on the material temperature, T, as given by the diffusion coefficient [15, 16]:

$$D = D_0 \exp\left(-\frac{eE_D}{k_B T}\right), \tag{2.5}$$

where E_D is the activation energy of diffusion. Figure 2.7 shows schematics of the hydrogen diffusion processes in tungsten numerically calculated by S Kato [17]. Larger diffusion was confirmed for higher material temperature [17]. The particle inventory, *i.e.*, the amount of the particle absorbed in a wall material, is saturated during the plasma bombardment because the wall continuously re-emits the absorbed particles reaching the surface due to the diffusion. The saturated concentration of the particles absorbed in a material is known to be lower at higher target temperature due to the higher diffusion as described above.

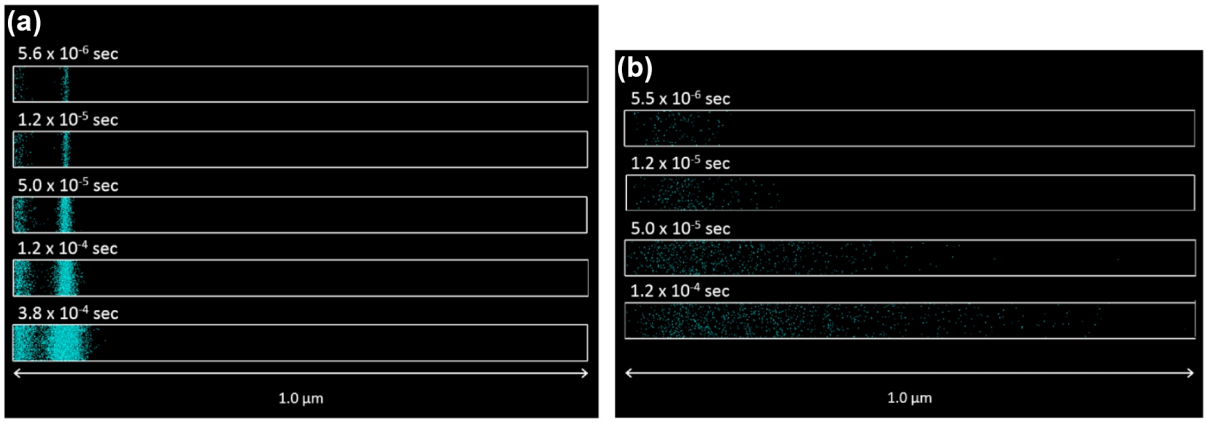

Figure 2.7. Schematic image of hydrogen particle diffusion process in W target as a fuction of time for different target temperatures: (a) 300 K and (b) 1000 K. The diffusion process shown was numerically calculated by S Kato, and the images were taken from his PhD thesis [17].

2.5 Formation of Surface Structures due to Helium Implantation

As briefly mentioned in Chapter 1, the low energy helium bombardment onto a hot W target can create surface structures such as dense micrometer-sized pores, *i.e.*, He bubble, and fibriform nanostructure, *i.e.*, W-fuzz. The He bubble surface structure can be formed as long as the incident He ions overcome the surface barrier energy of W to enter the inside of the bulk W [18]. Therefore, He ion implantation at low energy of 6 eV can even create the surface structure on a W surface, where the energy of 5.5–5.9 eV is considered as the surface barrier energy of W [19]. Near-surface He trapping at defects in the bulk W target is proposed to contribute to the formation of He bubbles [18, 20]. The defect sites in a solid material are known to be induced by knock-on effects due to high energy particles or high target temperature. Since all the reported W surface structure formations so far were actually confirmed under the He bombardment with high target surface temperature, one can deduce that the target temperature especially plays an important role in the creation of defects in W. The proportion of the number of thermally induced defects is

characterized by the target temperature T (K) as follows [21]:

$$C_v = \frac{N_\nu}{N + N_\nu} \sim \exp(-\frac{{E_\nu}^F}{k_B T}), \tag{2.6}$$

where N is the number of total lattice points in the material; N_ν is the number of the defects; and ${E_\nu}^F$ is the defect generation energy. The size and number of the He bubbles tends to increase with increasing the target temperature. Denser defects thermally induced at higher temperature contribute to the formation of denser He bubbles and growth of their size by coalescing neighboring bubbles, while the coalescence of the He bubbles can also result in nanometer-sized W-fuzz under certain condition of the target temperature. As shown in Fig. 1.4, it is known that the He ion implantation in the target temperature region of approximately 1000 - 2000 K creates the W-fuzz [22]. The W-fuzz formation process is illustrated in Fig. 2.8 [22]. It has been deduced that a chain occurrence of the nanometer-sized He bubble coalescence contributes to the formation of W-fuzz structure.

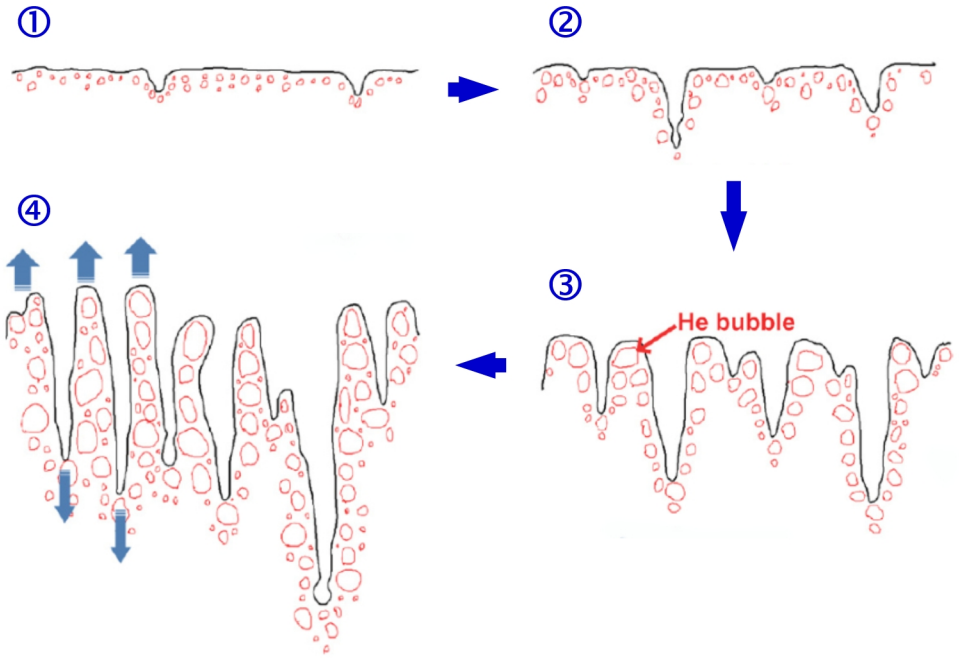

Figure 2.8. Schematic images of W-fuzz formation process. These images were originally compiled by S Kajita [22].

References

[1] C. D. Child, "Discharge From Hot CaO," *Phys. Rev. (Series I)*, vol. 32, no. 5, pp. 492–511, Jan. 1911.

[2] I. Langmuir, "The Effect of Space Charge and Residual Gases on Thermionic Currents in High Vacuum," *Phys. Rev.*, vol. 2, no. 6, pp. 450–486, Dec. 1913.

[3] R. N. Franklin, "The plasma–sheath boundary region," *J. Phys. D. Appl. Phys.*, vol. 36, no. 22, pp. R309–R320, Oct. 2003.

[4] D. Bohm, "Minimum Ionic Kinetic Energy for a Stable Sheath," in *The characteristics of electrical discharges in magnetic fields*, A. Guthrie and R. K. Wakerling, Eds., New York: MacGraw-Hill, 1949, pp. 77–86.

[5] K-U. Riemann, "The Bohm criterion and sheath formation," *J. Phys. D: Appl. Phys.*, vol. 24, no. 4, pp. 493–518, Apr. 1991.

[6] W. Eckstein, F. E. P. Matschke, and H. Verbeek, "Reflection of hydrogen from stainless steel and Nb," *J. Nucl. Mater.*, vol. 63, pp. 199–204, Dec. 1976.

[7] R. Behrisch and W. Eckstein, "Ion Backscattering from Solid Surfaces," in *Physics of Plasma-Wall Interactions in Controlled Fusion*, D.E. Post and R. Behrisch, Eds., New York, London: Plenum Press, 1986, pp. 413–438.

[8] S. Takamura, "Kyoukai ryouiki plasma rikougaku no kiso [Fundamentals of boundary-plasma science and engineering]," Tokyo: Morikita Shuppan, Jan. 2010, p. 165.

[9] W. Eckstein, "Reflection," *IPP-REPORT*, IPP 17/12, Aug. 2009.

[10] W. Eckstein, C. Garcia-Rosales, J. Roth, and W. Ottenberger, "Sputtering data," *IPP-REPORT*, IPP 9/82, Feb. 1993.

[11] W. Eckstein, J. Bohdansky, and J. Roth, "Physical sputtering," in *Atomic and Plasma-Material Interaction Data for Fusion, vol.1 (Supplement to journal Nuclear Fusion)*, R. K. Janev, Ed., Vienna: IAEA, Sep. 1991, pp. 51–61.

[12] W. Eckstein, C. Garciá-Rosales, J. Roth, and J. László, "Threshold energy for sputtering and its dependence on angle of incidence," *Nuclear Inst. and Methods in Physics Research, B*, vol. 83, no. 1–2. pp. 95–109, Oct. 1993.

[13] E. Vietzke and V. Philipps, "Hydrocarbon Formation on Carbon Surfaces Facing a Hydrogen Plasma," *Fusion Technol.*, vol. 15, no. 1, pp. 108–117, Jan. 1989.

[14] J. Roth, R. Preuss, W. Bohmeyer, S. Brezinsek, A. Cambe, E. Casarotto, R. Doerner, E. Gauthier, G. Federici, S. Higashijima, J. Hogan, A. Kallenbach, A. Kirschner, H. Kubo, J. . Layet, T. Nakano, V. Philipps, A. Pospieszczyk, R. Pugno, R. Ruggiéri, B. Schweer, G. Sergienko, and M. Stamp, "Flux dependence of carbon chemical erosion by deuterium ions," *Nucl. Fusion*, vol. 44, no. 11, pp. L21–L25, Nov. 2004.

[15] E. L. Cussler, *Diffusion: Mass Transfer in Fluid Systems (3rd ed.)*, New York: Cambridge University Press, 2009, p. 135.

[16] S. Takamura, "Kyoukai ryouiki plasma rikougaku no kiso [Fundamentals of boundary-plasma science and engineering]," Tokyo: Morikita Shuppan, Jan. 2010, p. 319.

[17] S. Kato, "Nitai syoutotsu kinji ni motodzuita ryuushi-busshitsu sougo sayou no suuchi simulation [Simulation of particle-material interaction based on binary-collision approximation]," Ph.D. dissertation, Doshisha University, Nov. 2015.

[18] D. Nishijima, M. Y. Ye, N. Ohno, and S. Takamura, "Formation mechanism of bubbles and holes on tungsten surface with low-energy and high-flux helium plasma irradiation in NAGDIS-II," *J. Nucl. Mater.*, vol. 329-333, pp. 1029–1033, Aug. 2004.

[19] H. Ullmaier, "The Influence of Helium on the Bulk Properties of Fusion Reactor," *Nucl. Fusion*, vol. 24, no. 8, pp. 1039–1083, Aug. 1984.

[20] D. Nishijima, M. Y. Ye, N. Ohno, and S. Takamura, "Incident ion energy dependence of bubble formation on tungsten surface with low energy and high flux helium plasma irradiation," *J. Nucl. Mater.*, vol. 313-316, pp. 97–101, Mar. 2003.

[21] K. Hyodo and T. Kamiya, "Zairyou no bussei [Physical properties of materials]," Tokyo: Asakura Shoten, 1982, p. 45.

[22] S. Kajita, W. Sakaguchi, N. Ohno, N. Yoshida, and T. Saeki, "Formation process of tungsten nanostructure by the exposure to helium plasma under fusion relevant plasma conditions," *Nucl. Fusion*, vol. 49, no. 9, p. 095005, Aug. 2009.

Chapter 3

Structure of the Ion Beam Based Test Stand Apparatus for Particle Reflection Property Measurement

3.1 Introductory Remarks

One of the most sophisticated experimental techniques to investigate the particle reflection is the particle method using an ion beam based test stand apparatus. Figure 3.1 shows the general structure of the experimental setup used for the measurements of hydrogen ion reflection properties. An ion sensitive detector detects charged particles, *i.e.*, ions, reflected from a sample surface under the ion bombardment. By employing a rotatable structure for the reflected ion detector in a vacuum vessel, the angular distribution as well as the angle-resolved energy distribution of the reflected ions can be measured. This chapter presents the detailed structure of the ion beam based test stand apparatus. The general structure of the apparatus has also been described elsewhere [1, 2, 3].

3.2 Ion Source

The ion source used here is a multicusp ion source (Fig. 3.2). The DC hot cathode discharge based on W filaments produces a hydrogen plasma at the inside of the ion

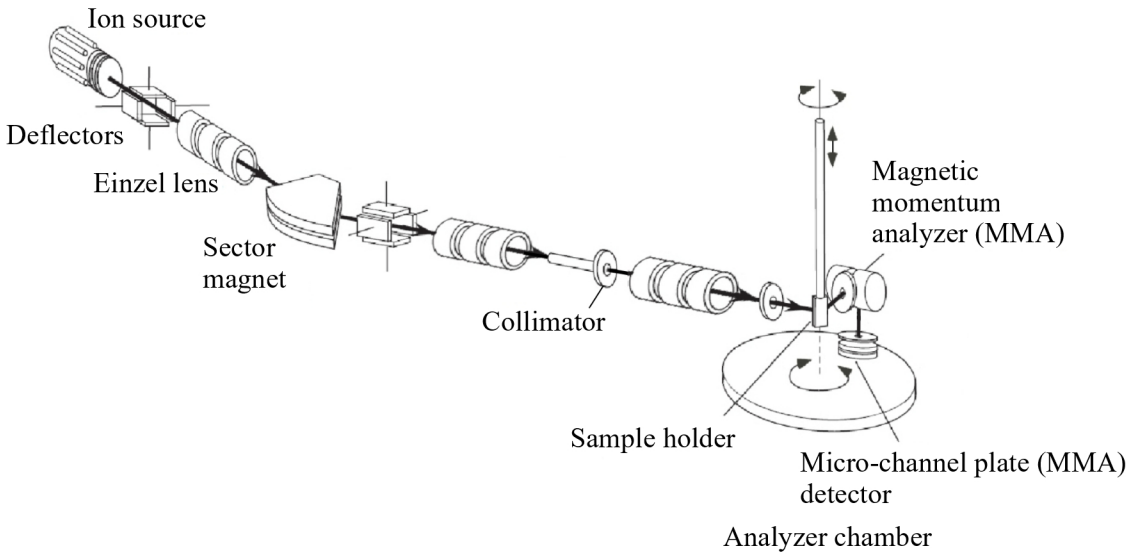

Figure 3.1. Ion beam based test stand apparatus.

source. A multicusp ion source has a characteristic magnetic field configuration as shown in Fig. 3.2(b). This multicusp magnetic field structure is formed by permanent magnets concentrically arranged on the side surface of the ion source. The cusp magnetic field lines efficiently confine primary ionizing electrons and realize the formation of a stable plasma [4].

The voltage applied to the ion source extracts an ion beam from the ϕ6 mm aperture. The acceleration region at the immediate downstream of the ion source has three layers comprised of plasma electrode, deceleration electrode and ground electrode. To extract positive H^+ ions, the ion source body and the plasma electrode are biased at a positive potential, which corresponds to the ion beam energy. The gas pressure is relatively high at the immediate downstream of the ion source because of the residual gas flow into the downstream from the aperture. The extracted ions can ionize these neutral molecules by collisions. Electrons produced by the ion-impact ionization of the neutrals can be attracted by the positive bias potential of the ion source, resulting in the back stream of electrons [5, 6]. The back-streaming electrons potentially destabilize the ion source operation by heating electrodes. A negative bias is applied to the deceleration electrode in order to prevent the back stream of electrons. Figure 3.2(c) shows the potential curve of the region of acceleration and deceleration electrodes. The negative potential formed by the deceleration electrode serves as barrier against the back-streaming electrons [5].

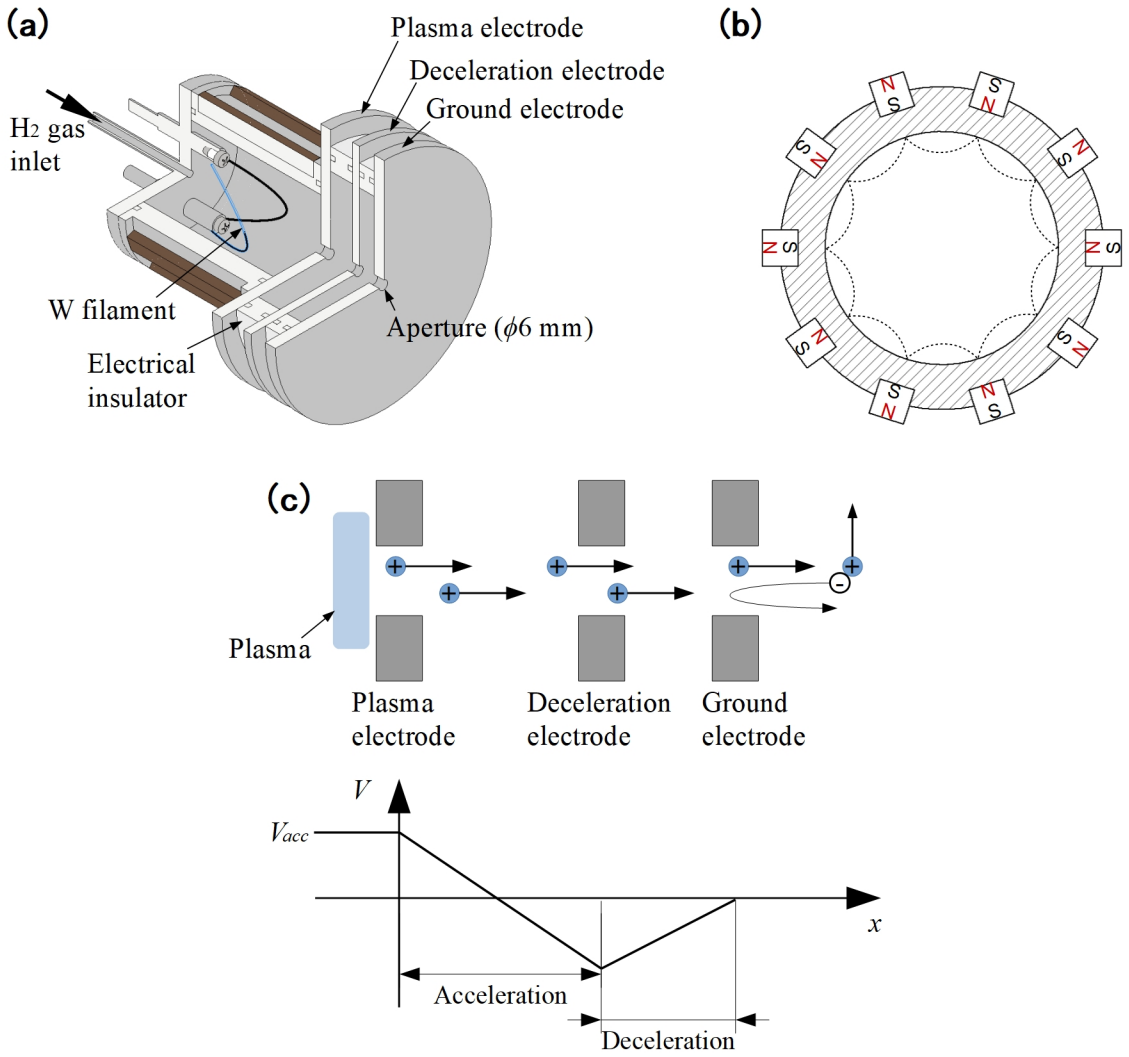

Figure 3.2. A multicusp ion source. (a) An assembly diagram. (b) Multicusp magnetic field configuration in the ion source. (c) The electric potential in the ion acceleration region. The negative potential formed by the deceleration electrode serves as barrier against the back-streaming electrons in order to prevent the destabilization of the ion source operation.

3.3 Ion Beam Transport System

3.3.1 Space-Charge Effect

Once the ion beam is extracted and accelerated, it have to be transported to the target surface with a sufficiently maintained ion flux. However, the ion beam naturally diverges due to its space charge during the transport. Two kinds of forces work on ions in a beam due to beam self-generated electromagnetic fields as shown in Fig. 3.3: (a) Coulomb-force repulsion and (b) Lorentz-force attraction [7]. The electromagnetic force on a beam ion

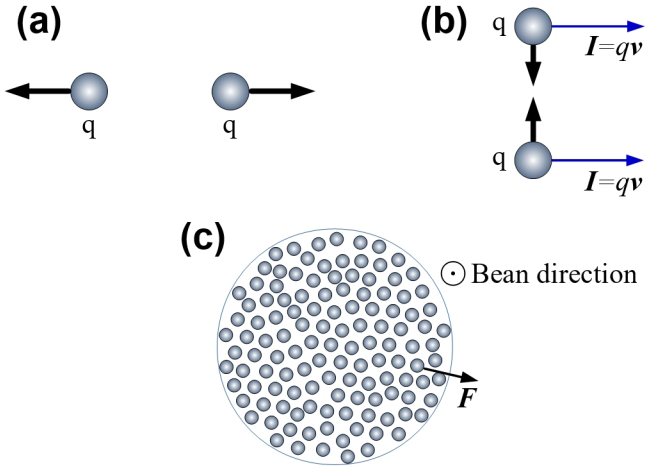

Figure 3.3. Schematic model of space-charge effect [7]. (a) Coulomb force repulsion. (b) Lorentz force attraction. (c) The space charge force on an ion in a beam due to self-generated fields.

can be written as a linear combination of the Coulomb and Lorentz forces in a vector form:

$$\boldsymbol{F} = q(\boldsymbol{E} + \boldsymbol{v} \times \boldsymbol{B}), \tag{3.1}$$

where q is the ion charge; E is the electric field; v is the ion velocity; and B is the magnetic flux density. In the beam divergence direction, *i.e.*, radial direction, one can obtain:

$$F_r = q(E_r + v_z B_\theta) = q(E_r + \beta_z c B_\theta). \tag{3.2}$$

Here, β_z is the proportion of the particle velocity along the beam direction against the light speed, c, as defined in $v = \beta c$. Assuming a beam with a cylindrically uniform distribution, the electric field along the radial direction can be described by:

$$E_r(r) = \frac{1}{\epsilon_0 r} \int_0^r \rho(r') r' dr', \tag{3.3}$$

where $\rho(r')$ represents the beam charge density at r'. On the other hand, the integral of Ampere's law over radial direction gives the magnetic flux density:

$$B_\theta(r) = \frac{\mu_0}{r} \int_0^r J(r') r' dr'. \tag{3.4}$$

Since the beam current density, $J(r')$, can be expressed using the beam charge density as $J(r') = \rho(r')\beta_z c$, Eq. 3.4 can be reformulated to:

$$B_\theta(r) = \frac{\mu_0 \beta_z c}{r} \int_0^r \rho(r') r' dr'. \tag{3.5}$$

From Eq. 3.3 and 3.5, one can obtain:

$$B_\theta(r) = \epsilon_0 \mu_0 \beta_z c E_r(r) = \frac{\beta_z}{c} E_r(r). \tag{3.6}$$

Accordingly, one can reformulate Eq. 3.2 to:

$$F_r = qE_r(1 - {\beta_z}^2). \tag{3.7}$$

Hence, it can be concluded that an ion beam normally diverges due to the space charge for an ion beam with $\beta_z << 1$. The space-charge effect becomes more significant especially for an ion beam at low energy because of the long transport time due to the slow velocity; more ions can be lost from a low-energy beam during the transport of same distance compared to higher energy ion beam.

3.3.2 Einzel Lens

An einzel (electrostatic) lens [8] reduces the beam emittance (divergence) by electrostatically focusing the ion beam without affecting the energy of the accelerated ion beam. The einzel lens is comprised by three electrodes as shown in Fig. 3.4. A positive voltage is applied to

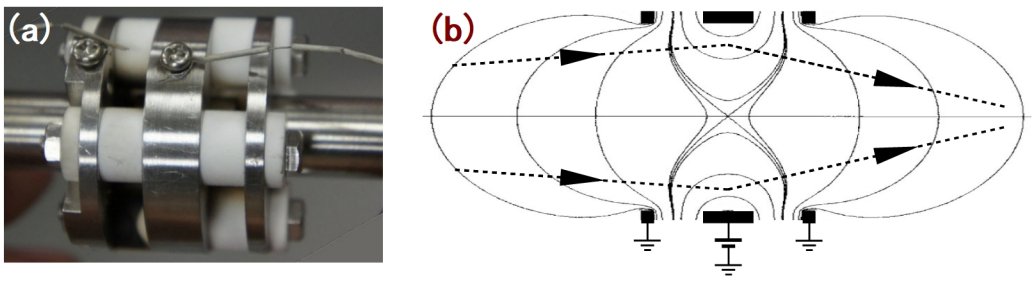

Figure 3.4. (a) A photograph and (b) a schematic drawing of the electric field in an einzel lens.

the middle electrode, while others at the both ends are grounded. Figure 3.4(b) shows a schematic image of the electric field produced by the einzel lens. It basically works like a concavoconvex lens for the ion beam.

3.3.3 Deflector

In addition to the einzel lens, deflectors are also equipped to the ion beam transport system in order to maximize the ion beam flux. Deflectors utilized in this study consist of two sets of two parallel electrodes, four electrodes in total. Positive and negative voltages are applied to each of the parallel electrodes to form an electric field, which slightly bends the ion beam in order to adjust the beam direction. In this study, voltages applied to both lenses and deflectors are adjusted by maximizing the actual ion beam current on the target surface while extracting the ion beam.

3.3.4 Sector Magnet

In the hydrogen ion beam extraction, all of atomic and molecular ions, *i.e.*, H^+, $H_2{}^+$ and $H_3{}^+$, including impurities such as O^+ and N^+ are extracted from the aperture. The sector magnet equipped on the beam transport system separates ions according to the Lorentz-force law: $F = qv \times B$. The magnetic-flux density, B, and the momentum of the ion, $\mu = mv$, have a directly proportional relation:

$$\mu = qrB, \tag{3.8}$$

where q and r represent the electron charge of the ion and the radius of the bent ion path, respectively. Thus, a specific ion species can be selected for the ion bombardment of a solid sample by adjusting the magnetic field intensity.

3.4 Magnetic Momentum Analyzer for Detection of Reflected Ions

The transported H^+ ion beam is injected onto a solid sample surface, and the ions backscattered from the surface are detected by a magnetic momentum analyzer (MMA). Both the target holder and MMA can be rotated in the vacuum vessel, allowing for the measurement of angle-resolved reflected particle intensity and velocity distributions. Figure 3.5 shows the structure of the MMA. A cone-shaped concave accommodates the target holder with high physical alignment precision by matching the cone-shaped protuberance of the bottom of the target holder with the concave of the MMA as shown inf Fig. 3.5(a). The beam incident angle with respect to the target surface can be adjusted by rotating the target. Water-cooled parallel coils form the magnetic field to separate ions in accordance with both charge and momentum by scanning the electricity. The entrance and exit slits of the MMA collimate the ions reflected from the surface to obtain higher angle and velocity resolutions. A micro-channel plate (MCP) detector, F4655 of Hamamatsu Photonics, detects the ions selected by the electromagnets. The incident ions produce secondary electrons at the surface of MCP, and the produced electron current is amplified due to the avalanche effects.

Figure 3.6 shows an example of the spectra of reflected ions measured by the MMA. Both reflected H^+ and H^- ions can be measured by a single scan of the analyzer coil voltage from negative to positive. The analyzer coil voltage is calibrated to the energy in the unit of electronvolt (eV) by $E = (0.114 * |V| + 0.555)^2$. The uncertainty of the energy is of the order of 20 - 30% of the reflected particle energy.

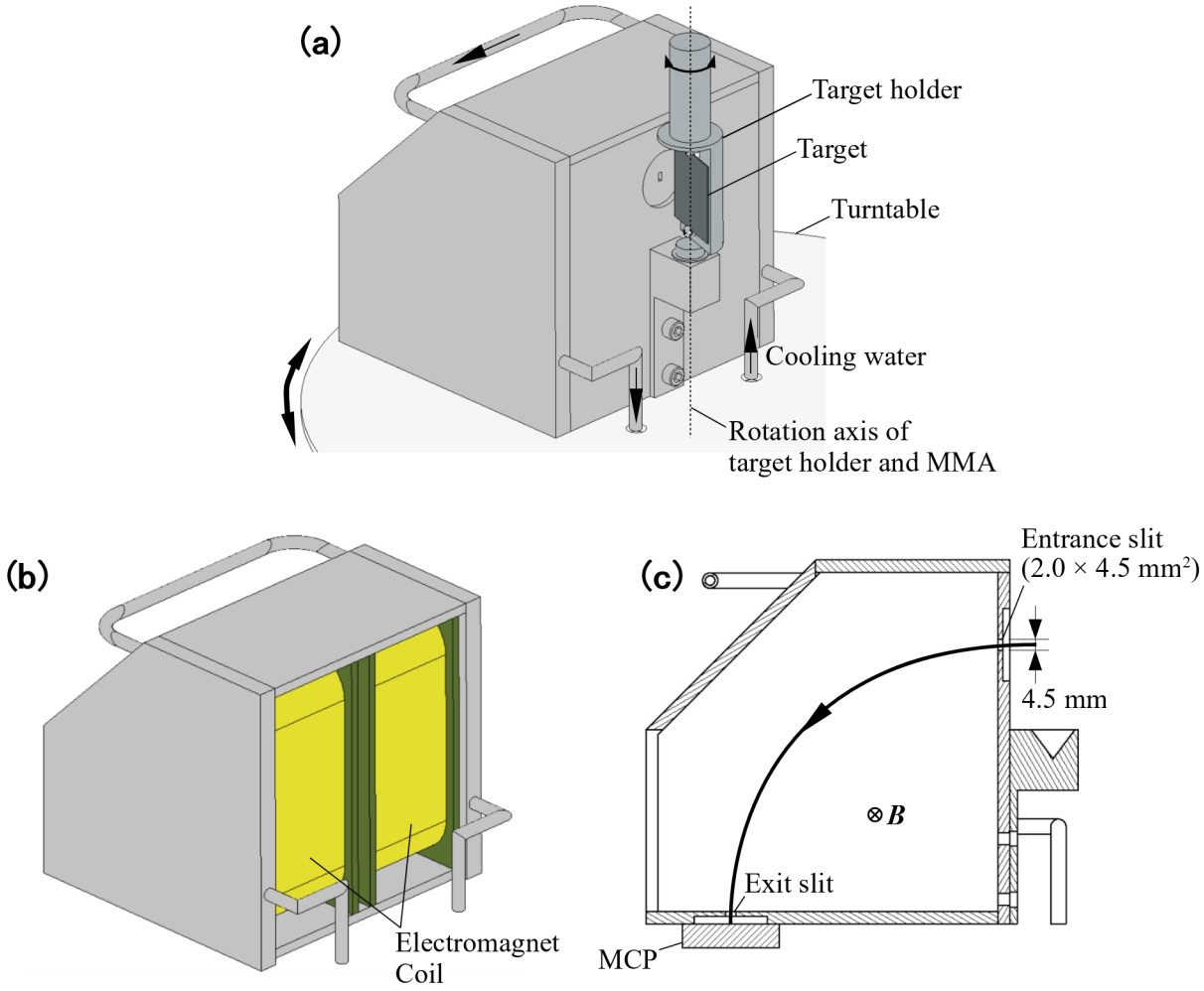

Figure 3.5. Schematic drawings of the magnetic momentum analyzer (MMA).

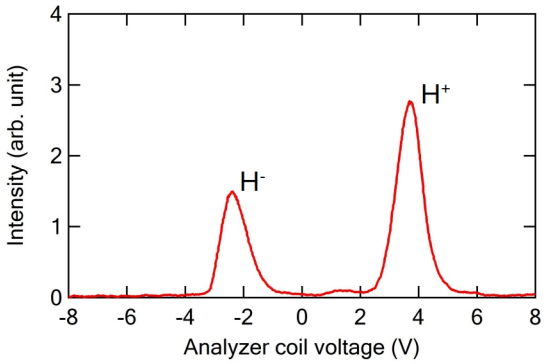

Figure 3.6. An example of spectra of reflected ions measured by MMA.

References

[1] H. Yamaoka, Y. Matsumoto, M. Nishiura, K. Nishimura, M. Sasao, and M. Wada, "Angular resolved energy distributions of low energy light ions reflected from a polycrystalline Mo surface," *J. Nucl. Mater.*, vol. 337–339, pp. 942–945, Mar. 2005.

[2] H. Yamaoka, Y. Matsumoto, M. Nishiura, K. Tsumori, H. Sugawara, S. Takeuchi, K. Shinto, M. Sasao, and M. Wada, "Development of an angular-resolved momentum analyzer system to study particle reflections from solid surfaces," *Rev. Sci. Instrum.*, vol. 77, no. 3, pp. 3–6, Mar. 2006.

[3] S. Kato, "Nitai syoutotsu kinji ni motodzuita ryuushi-busshitsu sougo sayou no suuchi simulation [Simulation of particle-material interaction based on binary-collision approximation]," Ph.D. dissertation, Doshisha University, Nov. 2015.

[4] K. N. Leung, "Multicusp ion sources (invited)," *Rev. Sci. Instrum.*, vol. 65, no. 4, pp. 1165–1169, Apr. 1994.

[5] J. Ishihara, " Ion gen kougaku [Ion source engineering]," Tokyo: Aionikusu, May 1986, p. 188.

[6] C. Hu, M. Wu, Y. Xie, Y. Xu, X. Li, and C. Jiang, "Preliminary analysis of backstreaming electrons on the source plasma region of ion sources for the EAST-NBI," *Plasma Sci. Technol.*, vol. 19, no. 4, p. 045602, Apr. 2017.

[7] N. Chauvin, "Space-Charge-Effect," in *CERN Yellow Report CERN-2013-007*, R. Bailey, Ed., 2014, pp. 63–83.

[8] D. W. O. Heddle, *Electrostatic Lens Systems*, London: IOP Publ., 2000, p. 63.

Chapter 4

Hydrogen Ion Reflection at Nanostructured Tungsten Surfaces

4.1 Introductory Remarks

Reflection properties of hydrogen ions at W surfaces including He bubble and W-fuzz samples were investigated by using the ion beam based test stand apparatus in order to clarify the effects of the surface morphology upon the particle reflection. This chapter presents the measured results of hydrogen ion reflection properties at the He-irradiated W surfaces together with the preparation processes and FE-SEM characterizations of the samples. This chapter has also been published as Ref. [1].

4.2 Preparation of Nanostructured W Samples

The W samples were prepared and provided by Dr. H T Lee of Osaka University. Two types of He-modified W surfaces were prepared in following manners. First, 0.3-mm thick polycrystalline W samples (99.95% purity, Nilaco) were prepared for the He-ion bombardments. The total area of the prepared poycrystalline W was 20×24 mm^2. A mixed beam of D + He ions at 300 V acceleration was implanted onto the W surface maintained at 800 K. The flux of 5×10^{19} D-particles m^{-2}s^{-1} (2% He) struck the surface for the duration of 1000 s. The resultant structure of dense network of nano-bubbles localized

within 20 nm of the surface (see Fig. 4.1(a)) is called He bubble [2]. Another polycrystalline W was exposed to a pure He plasma at −150 V target bias for the duration of 3000 s. The He fluence onto the W surface in this He-bombardment experiment was 6-9×10^{24} He-particles m^{-2}. The surface was maintained at ∼1200 K during the bombardment. This pure He-plasma bombardment resulted in the formation of fibriform nanostructure – so-called W-fuzz. The untreated smooth W (W-reference) was also prepared for the comparison of hydrogen ion reflection properties.

Figure 4.1 shows surface images of the prepared samples. The presence of nanostructures can be visually confirmed on the FE-SEM images of both D + He ions or He-plasma bombarded W samples. One has to note that each FE-SEM images were obtained in

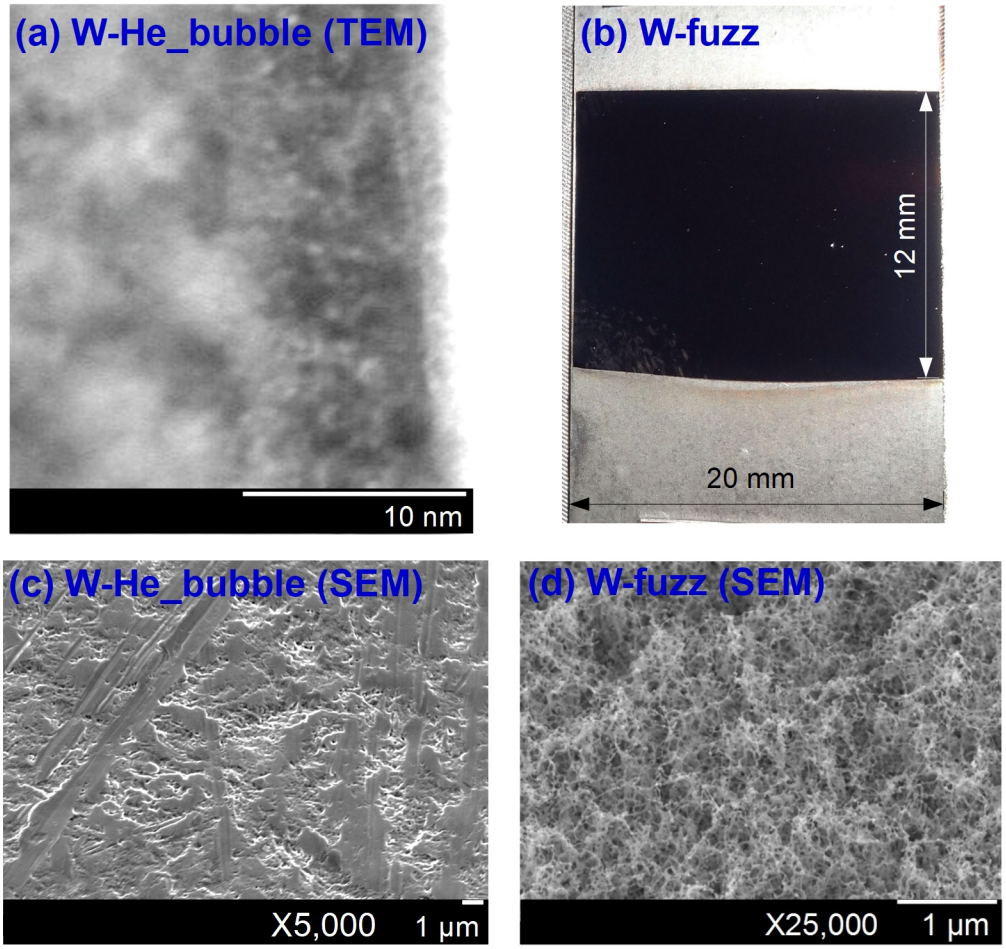

Figure 4.1. Surface images of the nanostructured W samples: (a) TEM image of W-He_bubble sample [2], (b) photograph of W-fuzz sample, and SEM images of (c) W-He_bubble sample and (d) W-fuzz sample. One has to note that the absolute scales on each SEM images are different. The SEM images were observed with 45° tilt angle.

different magnifications. On the surface of the W-He_bubble sample, small pore-like structures appeared due to the He-bubble formation near the surface layer (see the SEM image in Fig. 4.1(c)). Figure 4.1(b) shows a photograph of the surface of the W-fuzz sample. The fuzz structure is localized in the area of 20×12 mm^2 on the W surface; it appears black to the human eye due to its extremely low reflectance for the visible light. The He-bubbles and pore-like structures on the W-He_bubble sample cannot be confirmed visually by the naked eyes. Therefore, a photograph of W-He_bubble sample is not included in Fig. 4.1.

4.3 Experiment

In this study, positive hydrogen ions (H^+) at 1 keV were injected onto the prepared W samples, and the angular and energy distributions of the reflected ions were measured. Angle-resolved intensity and energy distributions of both backscattered H^+ and H^- ions were detected by the MMA (magnetic momentum analyzer) with a single scan. The mean reflected particle energy was estimated from the peak position of the Gaussian-shaped energy distribution of the reflected ions measured by the MMA, where the uncertainty of the energy was of the order of 20-30% of the reflected particle energy. The detailed features of the experimental setup are described in Chapter 3.

4.4 Results and Discussion

Figure 4.2 shows two-dimensional (2D) contour intensity maps of H^+ and H^- ions backscattered from W surfaces including W-He_bubble and W-fuzz. All of these angular distributions of reflected ions were measured under the injection of H^+ ion beam at 1 keV energy onto the W-sample surfaces. The intensity in an arbitrary unit is shown as a function of incident angle (α) and reflection angle (β), where these angles are with respect to the target plane as defined in Fig. 4.2(b). The solid lines correspond to specular reflection. The intensity of reflected H^- ions was always half of that of reflected H^+ ions among all samples. The intensity of reflected ions decreased in the following order: W-reference

(polycrystalline W), W-He_bubble and W-fuzz. The W-fuzz remarkably reduced the reflection intensity as small as about 30% of that from W-reference. The results suggest that these surface structures make the ion reflection coefficient smaller due to increasing the number of collisions of projectiles at the inside of samples. The angular distributions of reflected ions from modified surfaces were broader than that from W-reference.

Classical trajectory Monte Carlo simulations using ACAT code [3] were also performed. In the simulations, hydrogen atoms were injected onto a bulk W target. The incident energy of hydrogen atoms was set to be 1 keV. The ACAT code classically simulates trajectories of incident and recoiled atoms without discriminating ions from neutral atoms. On the other hand, the MMA detects reflected particles only in the form of ions in the

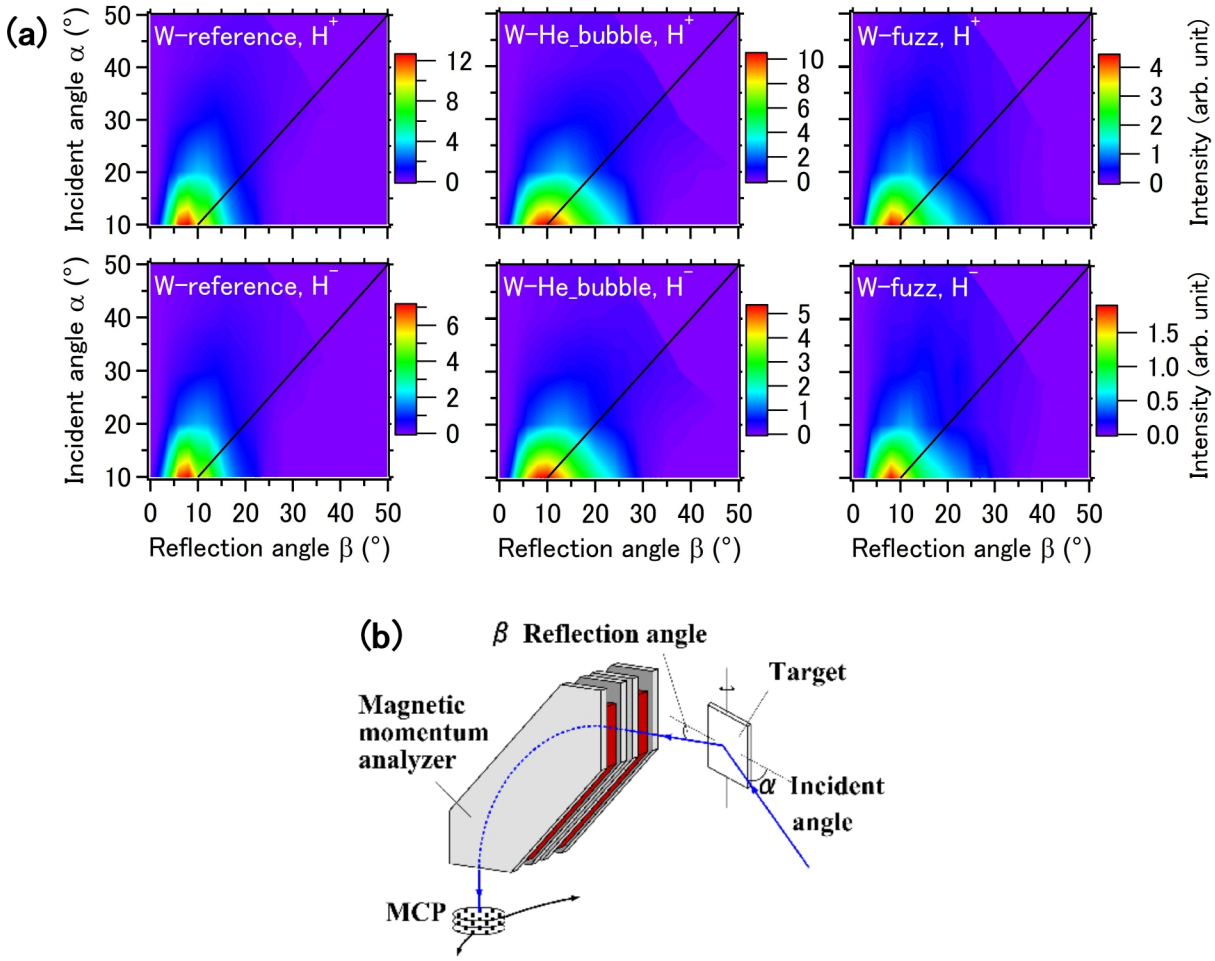

Figure 4.2. (a) Measured 2D contour intensity maps of H^+ and H^- ions reflected from W surfaces under the injection of H^+ ion beam at 1 keV energy. (b) The definition of incident and reflection angles. The solid lines correspond to specular reflection.

experiment. It can be assumed that reflected particles in the form of ions possess higher energy compared to those in the form of neutral atoms in accordance with the measured charge-state fractions of reflected atoms reported by W Eckstein (refer to Fig. 2.2 in Chapter 2). Considering this difference between the experiment and simulation, the reflected particles were collected at two energy ranges: $E_r > 400$ eV and $E_r > 700$ eV, where E_r denotes energy of a reflected particle. Certainly, the measured average energy of reflected H^+ ions was always in the range of 0.8 - 1 keV as shown in Fig. 4.4(d). Figure 4.3 (a) and (b) show the calculated 2D intensity contour maps of reflected hydrogen atoms from W with the normal density of 19.3 g cm^{-3} for two reflected particle energy ranges. Figure 4.3 also includes calculated results for the bulk W with the density set to be equivalent to the virtual surface density of W-fuzz. Note that the depth of the low density layer was not specified in the simulation and the density of entire amorphous W was assumed to be low. The virtual density of a typical fuzz layer can approximate 3.86 g cm^{-3}, which was estimated from the porosity of 0.8 [5, 6, 7]. The angular intensity distributions of reflected particles from the low density W became broader in both energy ranges compared to those of the normal density W. The calculated reflection coefficient

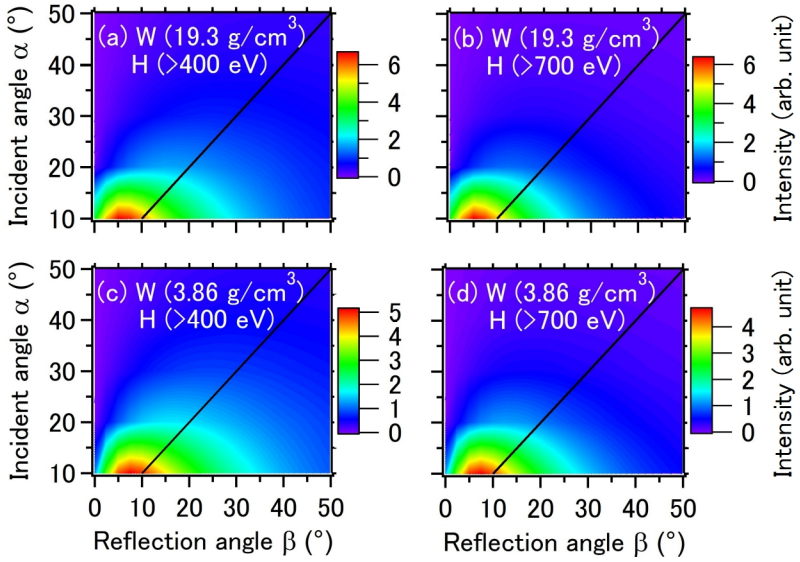

Figure 4.3. 2D contour intensity maps of hydrogen atoms reflected from a W surface simulated by the ACAT code. The hydrogen atoms at 1 keV energy were assumed to be incident onto W surfaces with the density of (a-b) 19.3 g/cm^3 and (c-d) 3.86 g/cm^3. The reflected atoms were collected at two energy ranges of $E_r > 400$ eV and $E_r > 700$ eV. The solid lines correspond to specular reflection. The definition of incident and reflection angles is shown in Fig. 4.2(b)

for the low density W shows 3% drop from that for the normal density W. Remarkable decrease of the reflection intensity occurred in the energy range of $E_r > 700$ eV compared to $E_r > 400$ eV. In both density cases, the deviation from the specular reflection is larger at higher incident angles at $E_r > 700$ eV compared to that at $E > 400$ eV, and the 2D intensity map at $E_r > 700$ eV seems to explain the experimental results well.

Figure 4.4 shows the ACAT-simulated reflection angle dependence of the intensity and average energy of reflected atoms obtained for a specific incident angle case at $\alpha = 10°$ together with the measured results. In the simulation, the intensities of reflected atoms were collected at the energy region of $E_r > 700$ eV, while the reflected particle energy in Fig. 4.4(d) corresponds to the average energy of all reflected atoms collected without the energy threshold. The intensity in the ACAT simulation is obtained as the number of reflected particles per solid angle normalized by the number of incident particles, *i.e.*, the reflectance per solid angle. As shown in Fig. 4.4(a), the ACAT-simulated reflection angle dependence of the reflectance also became lower in case of low density W corresponding to porous W-fuzz in the experiment. Porous surface makes the reflection coefficient lower. This is mainly caused by an increase of number of collisions as the virtual surface density decreases. The ACAT simulation calculated the average number of collisions to be 63.4 in normal density W and 174.8 in low density W, respectively. The ACAT simulation explained the decrease of reflection intensity from a porous surface quantitatively. Figure 4.4 (b) and (c) show the normalized reflection intensity versus the reflection angle (β) obtained by experiment and ACAT simulation, respectively. The low density W in the ACAT simulation made the angular distribution broader as same in the experiment where the angular distribution became broader in case of W-fuzz. The ACAT simulation results show wider angular distribution of the reflection intensity compared to the experiment. The simulation results include neutrals ejected from the surface with larger number of collisions in W. Certainly, the width of the angular intensity distribution became narrower as the energy of reflected atoms increases as seen in Fig. 4.4(c).

Figure 4.4(d) shows both measured and simulated reflection-angle dependence of energy of reflected particles. Reflected particle energy using analytical formula based on the

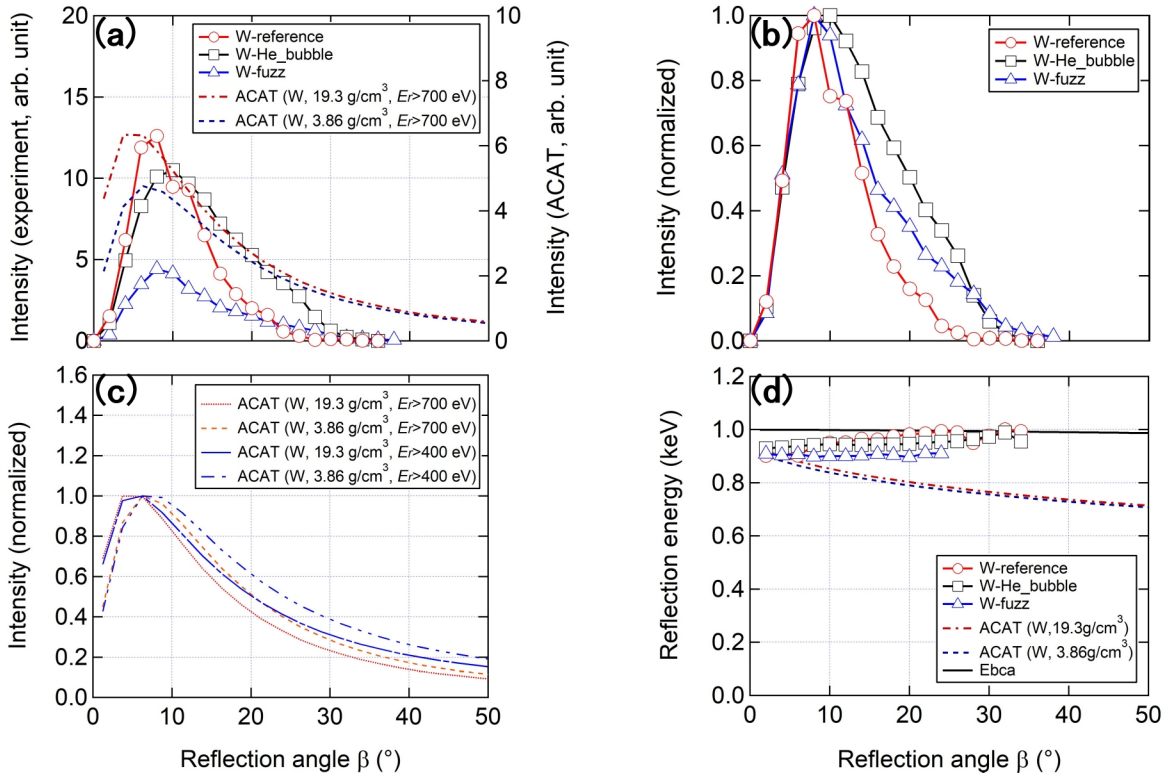

Figure 4.4. Reflection-angle dependence of (a) the intensity, (b) normalized intensity, and (c) ACAT simulation results for hydrogen atoms reflected from normal density W (19.3 g/cm^3) and low density W (3.86 g/cm^3) with two reflected particle energy thresholds, and (d) reflection-angle dependence of reflected particle energy obtained by the ACAT simulations for both low and normal density W together with the experimental results. The mean reflected particle energy was estimated from the peak position of the Gaussian-shaped energy distribution in the experiment. An analytical curve based on the binary collision approximation (E_{bca}), solid line is also displayed in (d). Data here were obtained under the hydrogen ion, in the experiment, or atom, in the simulation, bombardment at the incident particle energy of 1 keV and the incident particle angle of $\alpha = 10°$. The experimental results are shown only for the reflected positive hydrogen ions (H^+).

binary collision approximation [8] is also displayed. We can confirm the decrease of the reflected particle energy in case of porous W-fuzz as well as low density W in the simulation, showing small decrease of the reflected particle energy compared to the normal density W. This fact corresponds to the increase of number of collisions in a porous W. Experimentally, the reflected ion energy does not show a significant reflection angle dependence and the trend is rather described nearly by the single binary collision. The difference between the simulation and the experimental results suggests that the ion reflection may occur near the surface layer.

4.5 Summary

In this chapter, the effects of the W surface morphology upon the hydrogen ion reflection were examined in relatively high incident particle energy of 1 keV. The angular and energy distributions of H^+ and H^- ions reflected from fuzz and W-He_bubble were investigated. The intensity of the reflected ions for the W-fuzz was much lower, and angular distributions of the reflected ions for the W-fuzz and W-He_bubble samples were broader compared to that for the W-reference. Simulations indicated that these facts could be caused by actual low surface density and increase of number of collisions.

In reality, however, the incident particle energy is expected to be lower than several 100 eV in divertor of a fusion device, and most of the particles are reflected in the form of neutral atoms as discussed in Section 2.2. Reflection properties of neutral hydrogen atoms are required to be investigated in lower incident particle energy range. However, the ion beam diverges during the transport due to space charge effects especially in this low energy range of several 100 eV. Therefore, a new measurement technique for neutrals reflected from a solid surface in low incident particle energy needs to be established. First of all, the ion beam transport distance has to be much shorter than that of the ion beam based test stand apparatus in order to minimize the ion beam loss during the transport. In addition, another mechanism has to be introduced to detect reflected neutral particles, while the MMA only detect ions. In later chapters, a measurement technique based upon the optical Doppler spectroscopy is discussed. Before starting the discussion on the development of the Doppler-spectroscopic measurement technique, fundamental knowledge required to understand the optical spectroscopy is summarized in next chapters as follows – Chapter 5: principles of light emissions in plasma, and Chapter 6: principles of optical spectroscopic instruments.

References

[1] K. Doi, Y. Tawada, H. T. Lee, S. Kato, N. Tanaka, M. Sasao, M. Kisaki, M. Nishiura, Y. Matsumoto, T. Kenmotsu, M. Wada, Y. Ueda, and H. Yamaoka, "Reflection properties of hydrogen ions at helium irradiated tungsten surfaces," *Phys. Scripta*, vol. T167, p. 014044, Jan. 2016.

[2] H. T. Lee, Y. Ohtsuka, Y. Ueda, K. Sugiyama, E. Markina, and N. Yoshida, "Incident Ion Energy and Temperature Dependence of Helium Bubble Formation and Its Impact on D-Retention Under Simultaneous He-D Irradiation of Tungsten," *Fusion Sci. Technol.*, vol. 63, no. 1T, pp. 233–236, May 2013.

[3] Y. Yamamura, "Dynamical simulations of cascade damage in Cu, Ag and Au," *Nucl. Instr. Meth. Phys. Res. B*, vol. 51, no. 4, pp. 407–416, Oct. 1990.

[4] W. Eckstein, F. E. P. Matschke, and H. Verbeek, "Reflection of hydrogen from stainless steel and Nb," *J. Nucl. Mater.*, vol. 63, pp. 199–204, Dec. 1976.

[5] M. J. Baldwin and R. P. Doerner, "Formation of helium induced nanostructure 'fuzz' on various tungsten grades," *J. Nucl. Mater.*, vol. 404, pp. 165–173, Sep. 2010.

[6] D. Nishijima, M. J. Baldwin, and J. H. Yu, "Sputtering properties of tungsten 'fuzzy' surfaces," *J. Nucl. Mater.*, vol. 415, pp. S96–S99, Aug. 2011.

[7] S. Kajita, N. Yoshida, R. Yoshihara, N. Ohno, T. Yokochi, M. Tokitani, and S. Takamura, "TEM analysis of high temperature annealed W nanostructure surfaces," *J. Nucl. Mater.*, vol. 421, pp. 22–27, Feb. 2012.

[8] H. Niehus, W. Heiland, and E. Taglauer, "Low-energy ion scattering at surfaces," *Surf. Sci. Rep.*, vol. 17, no. 4–5, pp. 213–303, May 1993.

Chapter 5

Line-Emission Spectra from Hydrogen Plasma

5.1 Photon Emissions from Hydrogen Plasma

Excited atoms as well as molecules in a plasma radiate photons at certain wavelengths due to the energy level transitions. Figure 5.1 shows the emission spectra from a magnetized hydrogen plasma. The prominent sharp peaks originate from hydrogen atoms, while excited hydrogen molecules contribute to the low intensity band spectra around 600 nm, *i.e.,* H_2 Fulcher band. Later sections describes the basic principles of the spectral light emission of atoms and molecules.

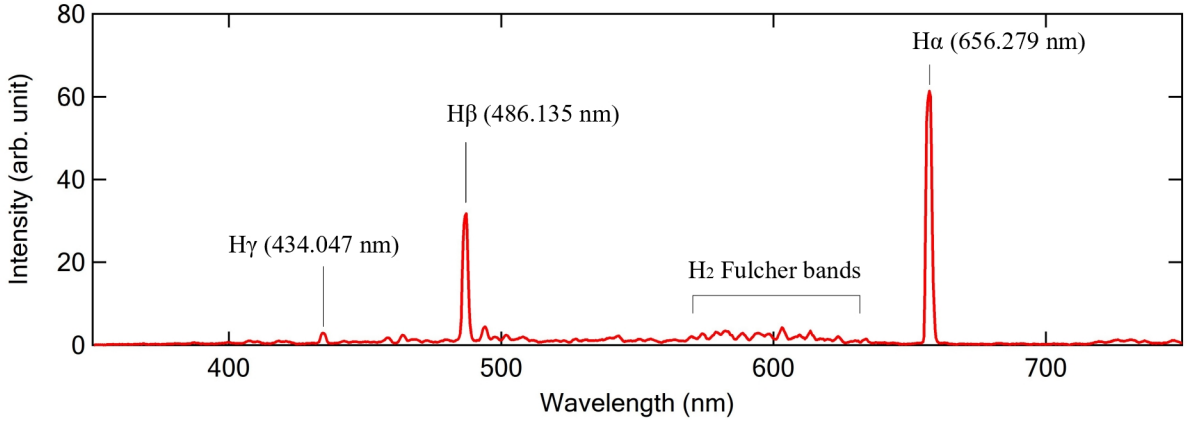

Figure 5.1. Spectra emitted from a magnetized plasma recorded by a wide wavelength range optical spectrometer.

5.1.1 Emission from Hydrogen Atoms

An atom emits a photon as a result of the energy level transition, which is defined as the transfer of an orbital electron from an arbitrary orbit to another. An electron in an atom belongs to a specific discrete energy level and exists within the corresponding orbit as shown in Fig. 5.2. This structure is called Bohr model [1]. Each discrete energy levels are characterized by the principal quantum number, $n = 1, 2, 3, \cdots$. The orbit radius at any n in a hydrogen-like atom of the atomic number Z is:

$$r_n = \frac{\epsilon_0 n^2 h^2}{\pi Z m_e e^2} \tag{5.1}$$

where m_e is the electron's mass; e is the charge of electron; ϵ_0 is the vacuum permittivity; and h is Planck's constant. The energy of the n-th level is determined by the orbital radius:

$$E_n = -\frac{Ze^2}{8\pi\epsilon_0 r_n} = -\frac{Z^2 m_e e^4}{8{\epsilon_0}^2 n^2 h^2}. \tag{5.2}$$

An orbital electron can transfer to a higher discrete energy level by collision with a particle or also a photon (*i.e.*, excitation). An atom in the excited state has the orbital electron in a higher discrete level, $n \geq 2$, than ground state, $n = 1$.

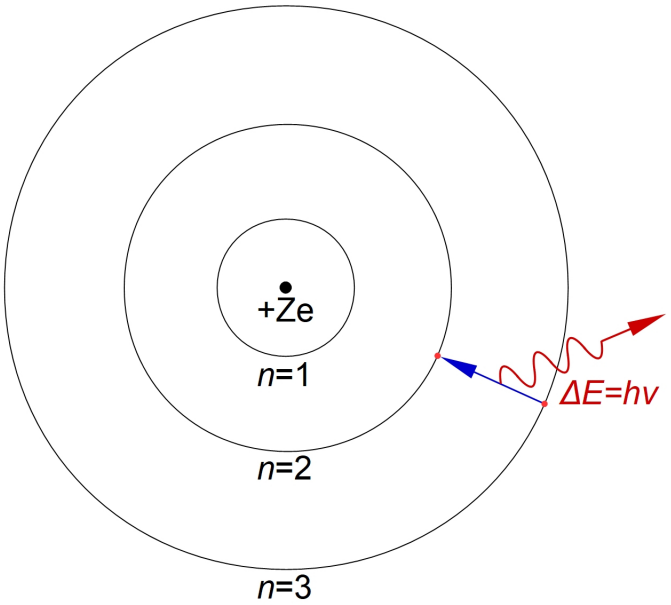

Figure 5.2. Energy levels of hydrogen-like atom in Bohr model [1].

A photon is emitted/absorbed in an energy level transition. Considering the energy conservation law, energy of the photon emitted/absorbed in a transition from an energy level n to another n' is given by:

$$E = |E_{n'} - E_n|. \tag{5.3}$$

If $E_{n'} - E_n > 0$, the transition is excitation, and the atom absorbs an photon. If $E_{n'} - E_n < 0$, on the other hand, the transition is deexcitation, and the atom emits an photon. The deexcitation takes place spontaneously once an atom is excited. The wavelength λ of the photon emitted can be calculated by:

$$E = h\nu = \frac{hc}{\lambda} = E_n - E_{n'} \tag{5.4}$$

where ν and c denote the frequency of the line and the speed of light, respectively. By rearranging Equation 5.4 and substituting Equation 5.2 in the rearranged equation, one obtains following equation:

$$\frac{1}{\lambda} = \frac{Z^2 m_e e^4}{8{\epsilon_0}^2 h^3 c}\left(\frac{1}{n'^2} - \frac{1}{n^2}\right). \tag{5.5}$$

This equation is called the Rydberg formula. It is important to notice that the Rydberg formula is only valid for hydrogen-like atoms and ions, *e.g.*, H, He^+, Li^{2+}, Be^{3+}, *etc.*, where only one electron is affected by an effective nuclear charge. The coefficient of the right side of Equation 5.5, $m_e e^4/(8{\epsilon_0}^2 h^3 c)$, is often denoted by R, so-called Rydberg constant, calculated to be $R = 1.097 \times 10^7\ \mathrm{m}^{-1}$, and we obtain the simplified Rydberg formula for a hydrogen-like atom of atomic number Z:

$$\frac{1}{\lambda} = Z^2 R\left(\frac{1}{n'^2} - \frac{1}{n^2}\right). \tag{5.6}$$

The Rydberg formula was first formulated by J Rydberg in 1888 and found to have a satisfactory fit to measured wavelength values of hydrogen Balmer series [2]. In 1913, N Bohr explained the Rydberg formula theoretically by introducing the Bohr model as

described above. For a hydrogen atom of $Z = 1$, the wavelengths of emissions in the Balmer series can be calculated using Equation 5.6 as follows: 656.3 nm for Hα ($n = 3 \rightarrow n' = 2$), 486.2 nm for Hβ ($n = 4 \rightarrow n' = 2$) and 434.1 nm for Hγ ($n = 5 \rightarrow n' = 2$).

Again, the transition from higher energy level $n = p$ to lower one $n' = q$ is spontaneous. The decay of the transition is described by [3]:

$$\left.\frac{dn(p)}{dt}\right|_{p\rightarrow q} = -A(p \rightarrow q)n(p) \tag{5.7}$$

where the energy levels p and q are arbitrary, and $n(p)$ is the number density of the atoms in the upper state $n = p$. $A(p \rightarrow q)$ denotes atomic transition probability or so-called Einstein A coefficient in the unit of s^{-1}. The inverse of the sum of $A(p \rightarrow q)$ in all possible spontaneous transitions gives the lifetime of the excited state at the energy level $n = p$ against the deexcitation [3]:

$$\tau_p = \frac{1}{\sum\limits_{q<p} A(p \rightarrow q)} = \frac{1}{A(p \rightarrow)}. \tag{5.8}$$

The lifetime of the $n = 3$ state resulting in the Hα line emitted by the transition $n = 3 \rightarrow n' = 2$ can be calculated to be ~10 ns from $A(n = 3 \rightarrow n' = 2) = 4.4101 \times 10^7$ and $A(n = 3 \rightarrow n' = 1) = 5.5751 \times 10^7$ [4]. It has to be noted that the presence of a strong external field varies the lifetime of excited atoms. For example, the Stark effect due to an external electric field can make the lifetime slightly longer [5]. It has been reported that the Stark lifetime of hydrogen atoms in the $n = 3$ level can be extended up to ~20 ns [5].

5.1.2 Emission from Hydrogen Molecules

Not only atoms, but molecules can also be excited by collisions in a plasma. Spectral emissions from molecules has more complex structure and richer number of spectral lines than those from atoms because of the additional quantum numbers: rotational and vibrational quantum numbers, denoted by $\jmath$ and v, respectively. Quantum-mechanically, the rotational and vibrational (ro-vibrational) motion of molecules is also treated as

eigenvalue problems, and thus the energy of the ro-vibrational motion is determined by the rotational and vibrational quantum numbers as discrete values. In diatomic molecules, the rotational energy is given by [6]:

$$E(\jmath) = B_v \jmath(\jmath+1) - D_v \jmath^2(\jmath+1)^2 + \cdots . \tag{5.9}$$

The coefficients B_v and D_v can be calculated using the rotational constants, B_e, α_e, D_e and β_e (in unit of cm^{-1}), to be [6]:

$$B_v = B_e - \alpha_e \left(v + \frac{1}{v}\right) + \cdots , \tag{5.10}$$

and

$$D_v = D_e - \beta_e \left(v + \frac{1}{v}\right) + \cdots . \tag{5.11}$$

The vibrational energy is given by [6]:

$$E(v) = w_e \left(v + \frac{1}{2}\right) - w_e x_e \left(v + \frac{1}{2}\right)^2 + w_e y_e \left(v + \frac{1}{2}\right)^3 + \cdots \tag{5.12}$$

where coefficients w_e, $w_e x_e$ and $w_e y_e$ are the vibrational constants (in unit of cm^{-1}). The total energy of a molecule including the electronic energy level E_e is simply described by the sum of three components [6]:

$$E = E_e + E(\jmath) + E(v). \tag{5.13}$$

The values of electronic energy, rotational and vibrational constants for specific states are summarized in Ref. [7].

In this study, H_2 Fulcher-α band spectra are used for the plasma characterization, *e.g.*, the degree of dissociation, as described later in Chapter 7. The Fulcher-α band spectra are emitted in the electronic transition of H_2 molecules from the electronic state $d^3\Pi_u$ ($3p\pi$) to $a^3\Sigma_g{}^+$ ($2s\sigma$). Considering the selection rule [6, 8] for the rotational-level transition, *i.e.*, $\Delta\jmath = 0, \pm 1$ (note that $\jmath = 0 \rightarrow 0$ is forbidden), three branches exist in the Fulcher-α band.

For $\Delta J = 0$, the resultant branch is called Q-branch. Other rotational-level transitions contributes to the emission band spectra of P-branch ($\Delta J = -1$) and R-branch ($\Delta J = +1$). Table 5.1 summarizes the wavelengths of spectra in the Fulcher-α band [9, 10].

Table 5.1. Wavelength table of H_2 Fulcher-α band spectra, originally compiled by S Kado [9].

Q-branch

Transition $(v' - v'')(\Delta J)J''$	Wavelength Air (nm)
(0 - 0)Q1	601.8299
(0 - 0)Q2	602.3757
(0 - 0)Q3	603.1909
(0 - 0)Q4	604.2716
(0 - 0)Q5	605.6091
(1 - 1)Q1	612.1787
(1 - 1)Q2	612.7246
(1 - 1)Q3	613.5395
(1 - 1)Q4	614.6186
(1 - 1)Q5	615.9565
(2 - 2)Q1	622.4815
(2 - 2)Q2	623.0258
(2 - 2)Q3	623.8391
(2 - 2)Q4	624.9150
(2 - 2)Q5	625.9565
(3 - 3)Q1	632.7060
(3 - 3)Q2	633.2482
(3 - 3)Q3	634.0575
(4 - 4)Q1	642.8119
(4 - 4)Q2	643.3510
(4 - 4)Q3	644.1498
(5 - 5)Q1	652.7355
(5 - 5)Q2	653.2644
(5 - 5)Q3	654.0525
(6 - 6)Q1	662.3842

P-branch

Transition $(v' - v'')(\Delta J)J''$	Wavelength Air (nm)
(0 - 0)P2	606.6631
(0 - 0)P3	609.5955
(0 - 0)P4	612.7648
(0 - 0)P5	616.1604
(0 - 0)P6	619.7721
(0 - 0)P7	623.5920
(1 - 1)P2	616.9639
(1 - 1)P3	619.9397
(1 - 1)P4	623.3004
(2 - 2)P2	627.1311
(2 - 2)P3	629.9423
(2 - 2)P4	632.9816
(2 - 2)P5	636.2479
(2 - 2)P6	639.7445
(3 - 3)P2	637.2212
(3 - 3)P3	639.9468
(3 - 3)P4	642.9310

R-branch

Transition $(v' - v'')(\Delta J)J''$	Wavelength Air (nm)
(0 - 0)R0	599.4072
(0 - 0)R1	597.5445
(0 - 0)R2	595.9825
(0 - 0)R3	594.7313
(0 - 0)R4	593.8022
(1 - 1)R0	609.8235
(1 - 1)R1	608.0783
(1 - 1)R2	606.7736
(1 - 1)R3	606.3283
(1 - 1)R4	606.2625
(2 - 2)R0	620.1185
(2 - 2)R1	618.2990
(2 - 2)R2	616.7732
(2 - 2)R3	615.5629
(2 - 2)R4	614.6901
(3 - 3)R0	630.3479
(3 - 3)R1	628.5384
(3 - 3)R2	627.3479

5.2 Line Broadening Mechanisms

As described above, an atom as well as a molecule in deexcitation emits a photon of certain wavelength determined by the energy difference of the transition. But measured spectral profiles actually have broadened shapes rather than single lines due to the resolution of the optical spectrometer and also broadening mechanisms.

5.2.1 Natural Broadening

The energy levels have dispersed uncertain layers due to Heisenberg's uncertainty principle [11]:

$$\Delta E \Delta t = \Delta E \tau_p \geq \frac{\hbar}{2}, \tag{5.14}$$

where τ_p is the finite lifetime of the energy level $n = p$. The dispersion of all energy levels is known to be Lorentz profiles. The Full width at half maximum (FWHM), $\Gamma_p = 2\Delta E(p)$, of the Lorentzian dispersion profile is determined by [11]:

$$\Gamma_p \tau_p = \hbar. \tag{5.15}$$

Since the energy levels are dispersed into the Lorentzian profile, the spectral lines emitted in energy transitions naturally have the Lorentzian shape. The halfwidth of the line emitted in a transition $n = p \rightarrow n' = q$ can be obtained in frequency units [11]:

$$\Delta\omega_{1/2} = \frac{\Gamma_p + \Gamma_q}{\hbar} = \frac{1}{\tau_p} + \frac{1}{\tau_q} = A(p \rightarrow) + A(q \rightarrow). \tag{5.16}$$

In wavelength units, one obtains [11]:

$$\frac{\Delta\lambda_{1/2}}{\lambda_{p\rightarrow q}} = \frac{\lambda_{p\rightarrow q}}{2\pi c}\{A(p \rightarrow) + A(q \rightarrow)\}. \tag{5.17}$$

For hydrogen Balmer-α (Hα) emission at 656.279 nm, the natural broadening width becomes $\sim$0.1 pm, which is normally negligible in laboratory plasmas due to much wider Doppler broadening described below.

5.2.2 Doppler Broadening

An emitter in kinetic motions shifts the wavelength of the observed light, resulting in the Doppler broadening of a spectrum. The wavelength shift, λ_D, on an emission of wavelength λ_0 due to an atom at kinetic energy of E is determined by:

$$\lambda_D = \lambda_0 \sqrt{\frac{2E\ (\mathrm{J})}{mc^2}} = 4.61 \times 10^{-5} \lambda_0 \sqrt{\frac{E\ (\mathrm{eV})}{A}}, \tag{5.18}$$

where m, c and A are the particle mass, light speed and mass number of the atom, respectively. In a plasma where number of atoms collectively exist, the wavelength shift on an emission spectrum is determined by the temperature T (K):

$$\lambda_D = \lambda_0 \sqrt{\frac{2k_B T}{mc^2}}, \tag{5.19}$$

where k_B is the Boltzmann's constant. As discussed earlier, dispersion of the energy levels contributes to the Lorentzian natural broadening of a line emission. On the other hand, Doppler broadening due to the thermal motion of atoms or molecules results in the Gaussian-shaped broadening of a spectrum if the emitters have a Maxwellian velocity distribution [12]. The halfwidth of the Gaussian Doppler-broadened profile in wavelength unit is given by [11]:

$$\frac{\Delta\lambda^G_{1/2}}{\lambda_{p\to q}} = \sqrt{8 \ln 2 \frac{k_B T}{mc^2}}. \tag{5.20}$$

For example, the with of a Gaussian Hα spectrum Doppler-broadened due to hydrogen atoms at temperature of 10 eV is calculated to be 0.16 nm, which is much broader compared to the natural broadening.

5.3 Fine Structure of Hα Emission Line

In the Bohr model, the Hα emission is described as a single line emitted in the energy level transition of $n = 3 \to n' = 2$. Indeed, an optical spectrometer observes one Gaussian-shaped spectrum in most cases of hydrogen-plasma spectroscopy because the thermal

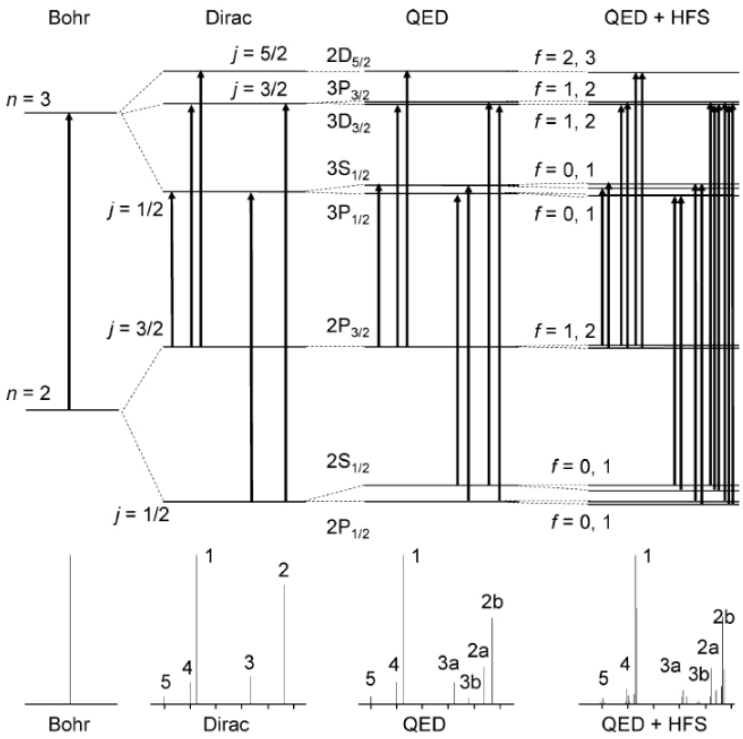

Figure 5.3. Structures of energy level transitions in the Hα emission illustrated by various theoretical approximations. From Kramida's work [13].

motion in plasma contributes to the Doppler broadening and a line emission is observed as convolution with the instrumental function of the optical spectrometer as discussed later in Chapter 6. However, atomic line emission spectra including Hα actually consist of multiple lines because of the fine-structured energy levels as shown in Fig. 5.3 [13]. The presence of a doublet in Hα was first discovered by high resolution spectroscopy. Subsequently, Dirac extended Bohr's theory by taking the special relatively into account. In the Dirac equation, an additional quantum number j is involved to describe the energy level $E(n, j)$ as follows [13, 14]:

$$\begin{aligned} E(n,j) &= 2\frac{R}{\alpha^2}\big\{f(n,j)-1\big\}, \\ f(n,j) &= \frac{1}{\sqrt{1+(\frac{\alpha}{n-\delta})^2}}, \\ \delta &= (j+\frac{1}{2})\left(1-\frac{1}{\sqrt{1-(\frac{\alpha}{j-\frac{1}{2}})^2}}\right). \end{aligned} \tag{5.21}$$

Here the quantum number j is called the total angular momentum quantum number, where both orbital angular momentum and spin angular momentum are taken into account.

The coefficient α is a dimensionless constant called the fine-structure constant given as $\alpha = e^2/(4\pi\epsilon_0\hbar c) = 7.2973525664(17) \times 10^{-3}$. The total angular momentum quantum number j is simply given by $j = l + s$, sum of the azimuthal quantum number l and the spin quantum number s, where $l = 0, 1, 2, \cdots, n-1$, and $s = \pm 1/2$. For the spin quantum number s, $+1/2$ is assigned to one electron in an orbital. If the orbital has plural electrons, -1/2 is assigned to the second electron. Namely, the spin quantum number s alternates $\pm 1/2$ for orbital electrons. Since hydrogen atom has only one orbital electron, the spin quantum number is $s = +1/2$. The energy levels $n = 2$ and $n = 3$ of hydrogen atom split in two and three separated levels, respectively. One has to note that the energy level transitions have to satisfy the following selection rules, $\Delta j = j - j' = 0, \pm 1$ (except $j = 0 \rightarrow j' = 0$) [15]. The Hα is separated into five discrete lines as shown in Fig. 5.3 [13] because of the forbidden transition $j = 1/2 \nrightarrow 5/2$.

To date, theoretical works based on Quantum Electrodynamics (QED) calculations [13, 16, 17, 18] have clarified the presence of further separated lines as shown in Fig. 5.3. Table 5.2 summarizes both observed and theoretically calculated wavelengths of the lines together with transition probabilities and energy levels [4, 13, 19].

Table 5.2. Wavelength table of fine-structured lines in hydrogen atomic Balmer-α spectrum [4, 13, 19]. Data were retrieved from NIST database [19].

Observed Wavelength Air (nm)	Ritz Wavelength Air (nm)	A_{ki} (s^{-1})	E_l (cm^{-1})		E_k (cm^{-1})	Lower Level	Upper Level
656.2709699	656.2709702	5.3877E+07	82 258.9191133	-	97 492.319433	$2P_{1/2}$	$3D_{3/2}$
	656.2714						
	656.2722						
656.2724827	656.2724827	2.2448E+07	82 258.9543992821	-	97 492.319611	$2S_{1/2}$	$3P_{3/2}$
	656.2751807	2.1046E+06	82 258.9191133	-	97 492.221701	$2P_{1/2}$	$3S_{1/2}$
	656.2767009		82 258.9543992821	-	97 492.221701	$2S_{1/2}$	$3S_{1/2}$
	656.2770						
656.2771534	656.2771533	2.2449E+07	82 258.9543992821	-	97 492.211200	$2S_{1/2}$	$3P_{1/2}$
656.279*	656.2819*	4.4101E+07	82 259.158	-	97 492.304	2	3
	656.2795						
656.285175	656.2851769	6.4651E+07	82 259.2850014	-	97 492.355566	$2P_{3/2}$	$3D_{5/2}$
	656.28533						
	656.2854						
	656.2867336	1.0775E+07	82 259.2850014	-	97 492.319433	$2P_{3/2}$	$3D_{3/2}$
	656.2909442	4.2097E+06	82 259.2850014	-	97 492.221701	$2P_{3/2}$	$3S_{1/2}$

References

[1] N. Bohr, "On the Constitution of Atoms and Molecules," *Philos. Mag.*, vol. 26, pp. 1–24, 1913.

[2] N. Bohr, " Rydberg's discovery of the spectral laws," *Proceedings of the Rydberg Centennial Conference on Atomic Spectroscopy*, Lund University Annals, N. F. Avd. 2. Bd. 50. Nr 21, pp. 15–21, 1955.

[3] H.-J. Kunze, "Chapter 6: Radiative Processes in Plasmas," in *Introduction to Plasma Spectroscopy*, Berlin, Heidelberg: Springer-Verlag, 2009, pp. 85–114.

[4] W. L. Wiese and J. R. Fuhr, "Accurate Atomic Transition Probabilities for Hydrogen, Helium, and Lithium," *J. Phys. Chem. Ref. Data*, vol. 38, no. 3, pp. 565–719, Jan. 2009.

[5] J. R. Hiskes, C. B. Tarter, and D. A. Moody, "Stark Lifetimes for the Hydrogen Atom," *Phys. Rev.*, vol. 133, no. 2 A, pp. 424–426, Jan. 1964.

[6] G. Herzberg, "Chapter 4: Elementary Discussion of Electronic States and Electronic Transitions," in *Molecular Spectra and Molecular Structure - I. Spectra of Diatomic Molecules, second ed.*, New York: Van Nostrand Reinhold, May 1950, pp. 146–211.

[7] G. Herzberg, "Appendix: Vibrationl and Rotational Constants for the Electronic State of All Known Diatomic Molecules," in *Molecular Spectra and Molecular Structure - I. Spectra of Diatomic Molecules, second ed.*, New York: Van Nostrand Reinhold, May 1950, pp. 146–211.

[8] G. Herzberg, "Chapter 5: Finer Details about Electronic States and Electronic Transitions," in *Molecular Spectra and Molecular Structure - I. Spectra of Diatomic Molecules, second ed.*, New York: Van Nostrand Reinhold, May 1950, pp. 212–314.

[9] S. Kado, "Anomaly in the P- and R- Branches in the Spectra of Hydrogen Fulcher Band Emission (in Japanese)," *J. Plasma Fusion Res.*, vol. 80, no. 9, pp. 783–792, Sep. 2004.

[10] H. M. Crosswhite, Ed., *The hydrogen molecule wavelength tables of Gerhard Heinrich Dieke*, New York: Wiley, 1972.

[11] H.-J. Kunze, "Chapter 9: Line Broadening," in *Introduction to Plasma Spectroscopy*, Berlin, Heidelberg: Springer-Verlag, 2009, pp. 153–178.

[12] J. Cooper, "Plasma spectroscopy," *Reports Prog. Phys.*, vol. 29, pp. 35–130, 1966.

[13] A. E. Kramida, "A critical compilation of experimental data on spectral lines and energy levels of hydrogen, deuterium, and tritium," *At. Data Nucl. Data Tables*, vol. 96, no. 6, pp. 586–644, Nov. 2010.

[14] P. A. M. Dirac, *The Principles of Quantum Mechanics, fourth ed.*, Oxford: Clarendon Press, 1958, p. 272.

[15] I. I. Sobelman, *Atomic Spectra and Radiative Transitions*, Berlin, Heidelberg: Springer-Verlag, 1979, p. 14.

[16] J. D. Garcia and J. E. Mace, "Energy Level and Line Tables for One-Electron Atomic Spectra," *J. Opt. Soc. Am.*, vol. 55, no. 6, pp. 654–685, Jun. 1965.

[17] G. W. Erickson, "Energy levels of one-electron atoms," *J. Phys. Chem. Ref. Data*, vol. 6, no. 3, pp. 831–870, 1977.

[18] W. R. Johnson and G. Soff, "The lamb shift in hydrogen-like atoms, $1 \leq Z \leq 110$," *At. Data Nucl. Data Tables*, vol. 33, no. 3. pp. 405–446, Nov. 1985.

[19] National Institute of Standards and Technology, 'NIST Atomic Spectra Database Lines Form', 2009. [Online]. Available: `https://physics.nist.gov/PhysRefData/ASD/lines_form.html`. [Accessed: 16- Nov- 2017].

Chapter 6

Spectroscopic Instruments

6.1 Principles of Optical Spectrometers

There are various types of optical spectrometers from a pocket-size low resolution spectrometer to a high resolution monochromator with several meter focal length. In this study, a high-resolution monochromator with 1 m focal length is used in order to observe the detail structure of Doppler-broadened Hα emission from energetic hydrogen atoms. Figure 6.1 shows the structural configuration of the monochromator used in this study. Grating is the key optical element to separate light into spectral components of their intrinsic wavelengths based upon the wavelength-dependent diffraction angles. Mirrors in the monochromator guides the light to the grating, and the diffracted light is recorded as spectral profiles by the charge-coupled device (CCD) detector array mounted at the image plane.

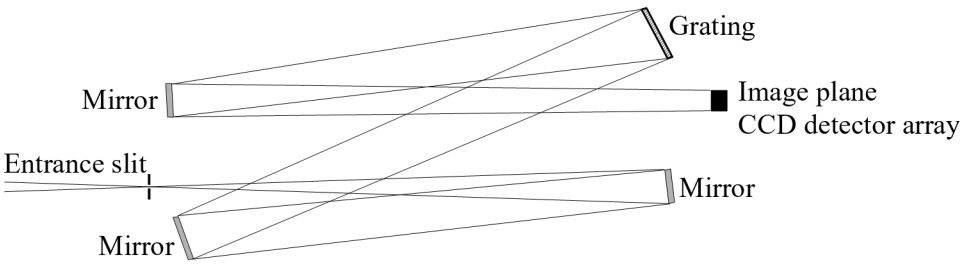

Figure 6.1. Mounting configuration of optics in the monochromator used in this study.

6.1.1 Grating

A diffraction grating has a micro-sized periodic structure on the surface, which splits light into spectral components with their wavelength-dependent diffraction angles. A typical schematic image of the diffraction grating is shown in Fig. 6.2 [1, 2]. Line grooves are arranged periodically at regular intervals of d. When light is incident with angle α, the grating diffracts the incident light in accordance with the grating equation [1, 2]:

$$m\lambda = d(\sin\alpha + \sin\beta), \ \ m = 0, \pm1, \pm2, \cdots . \tag{6.1}$$

Here λ is the wavelength of diffracted light; β is the diffraction angle; and m is the diffraction order. One has to note that α and β are defined as angles from the grating normal in anticlockwise. For example, α and β in Fig. 6.2 are $\alpha > 0$ and $\beta < 0$, respectively. At $\beta = -\alpha$, the grating acts as a mirror, and thus the diffracted light is not wavelength-resolved. The line of the diffracted light at $\beta = -\alpha$ is called zero order because the diffraction order m becomes $m = 0$ in Eq. 6.1. At $-\beta < \alpha$, m becomes positive and a spectrum appearing in this angle region is called the inside spectrum. On the other hand, the outside spectrum is observed at $-\beta > \alpha$, where it gives negative m. Figure 6.3 shows the schematic image of the light diffraction at the grating as calculated by Eq. 6.1. For the optical spectroscopy in a wide wavelength region, we have to pay attention to the

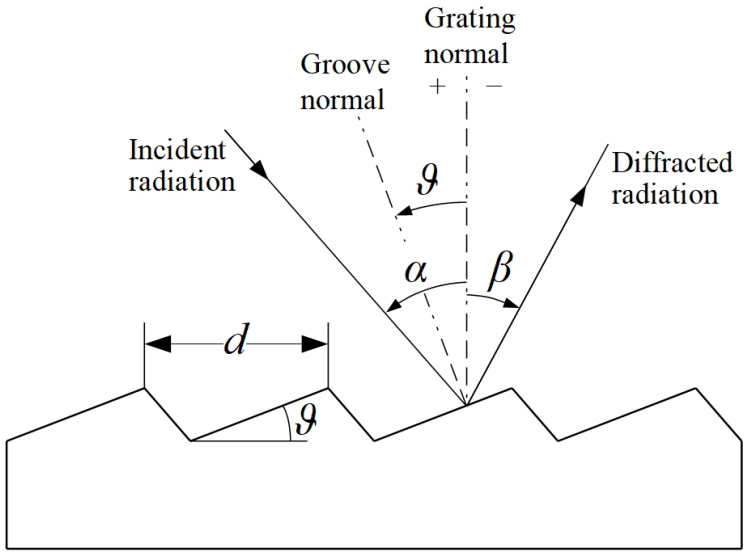

Figure 6.2. Schematic drawing of a grating and definition of angles [1, 2].

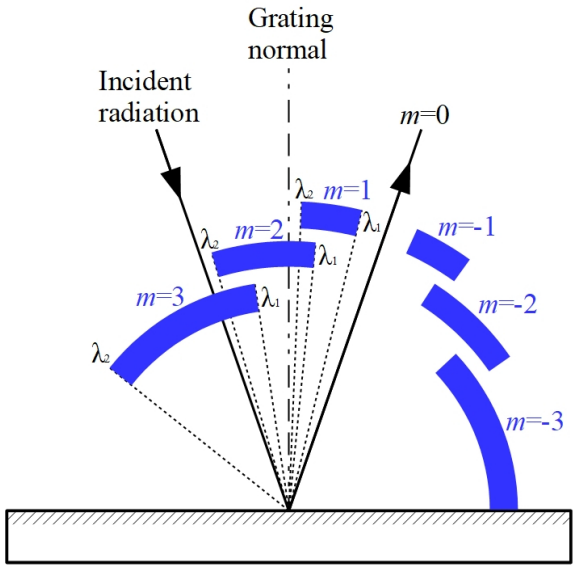

Figure 6.3. Schematic drawing of light diffraction at a grating and free spectral range [3].

overlapping from adjacent orders. The free spectral range is the wavelength region where spectra from other orders are not superimposed, and can be calculated by [3]:

$$\Delta\lambda = \lambda_{2,m} - \lambda_{1,m+1} = \frac{\lambda_1}{m}, \tag{6.2}$$

where $\lambda_{2,m}$ and $\lambda_{1,m+1}$ represent the m-th order of the wavelength λ_2 and the $(m+1)$-th order of the wavelength λ_1, respectively. For the Hα (656.28 nm) emission spectroscopy at the first order, radiations at wavelength of $\lambda < 350$ nm can overlap from the diffraction group at $m = 2$. This overlapping is negligible in the experimental setup in this study because the radiations in the wavelength region of $\lambda < 350$ nm have extremely low emission intensity compared to those around 656 nm. If the overlapping of spectra is not negligible, an optical filter can be used to cut the short wavelength spectra to prevent the overlapping from the other orders.

All gratings have the efficiency curve as a function of wavelength, *i.e.*, ratio of the diffracted power against the incident power. The efficiency curve takes the maximum at the wavelength λ_B corresponding to the specular reflection with respect to the groove normal:

$$\alpha - \vartheta = \vartheta - \beta. \tag{6.3}$$

By substituting this angular relation to Eq. 6.1, we obtain the grating equation for the specular reflection [1]:

$$m\lambda = 2d \sin\vartheta \cos(\alpha - \vartheta). \tag{6.4}$$

For $m = 1$ and $\alpha = 0$,

$$\lambda_B = d \sin 2\vartheta. \tag{6.5}$$

Here λ_B is so-called blaze wavelength, and ϑ is the blaze angle [1]. The efficiency curve of a grating normally takes the maximum around the blaze wavelength, and manufactures recommend the use of a grating in wavelength $\lambda_B/2 \leq \lambda \leq 2\lambda_B$ considering the efficiency curve.

6.1.2 CCD Detector

The radiation diffracted by grating can finally be recorded as spectra by an array detector equipped on the image plane of the monochromator. In this study, a CCD array is employed as the detector. The pixels of a CCD array consist of metal oxide semiconductor (MOS) capacitors. Figure 6.4 shows the structure of CCD detector [4]. A positive voltage applied to the metal gate electrode forms a potential well beneath the p-type silicon layer. The transparent photosensitive gate electrodes made of polysilicon are exposed to the light diffracted from the grating. The potential well formed by the voltage applied to the polysilicon gate accumulates photoelectons for the duration of the integration time of the measurement as shown in Fig. 6.4(a). Once the exposure ends, the accumulated charge in the potential well is transferred to the read-out circuit by alternatingly applying the positive voltage to the adjacent polysilicon gate as shown in Fig. 6.4(b) [4]. The CCD signal transfer methods are classified into four types: frame transfer (FT), full frame transfer (FFT), interline transfer (IT) and frame interline transfer (FIT) [4]. The CCD array used in this study transfers the signals based upon FFT. Figure 6.4(c) shows the structure of a FFT CCD. Alternatively, a photomultiplier tube (PMT) can also be used as a detector to record spectra. In use of a PMT, the grating mount angle needs to be scanned in order to record a spectral profile. An exit slit is employed to separate the

spectral light, and the PMT converts the light signal passing through the exit slit to electric signal while scanning the grating mount angle.

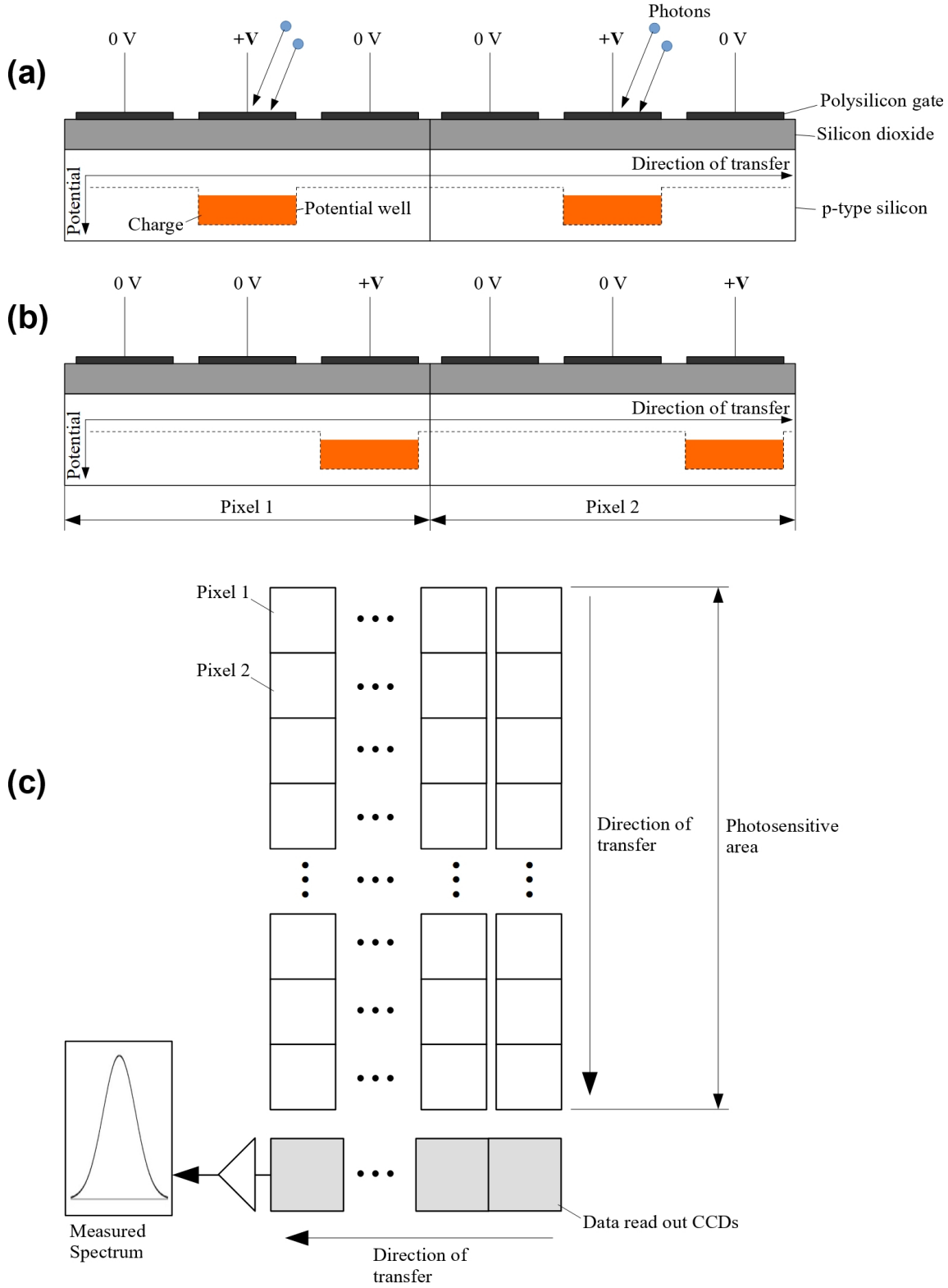

Figure 6.4. Basic structure of a CCD detector array and its operation principles [4]: (a) the data acquisition mode, (b) data transfer mode, and (c) structure of full frame transfer CCD.

6.2 Optics

6.2.1 Window

In this study, the monochromator observes visible light emission spectra from a hydrogen plasma formed in a vacuum vessel. The emissions are measured through a transparent window of the vacuum vessel. The selection of a material for the window is important considering the wavelength dependence of the light transmittance; light from the plasma can be cut off by the window in inappropriate choice of a window material. Figure 6.5 shows the light transmittance of several vacuum-window materials as functions of wavelength [1]. All of the window materials compiled in Fig. 6.5 transmit lights in the visible wavelength region (400 - 700 nm). In this study, BK7 (borosilicate crown glass) is chosen for the vacuum window because of its low unit cost as well as its sufficient transmittance for the visible light.

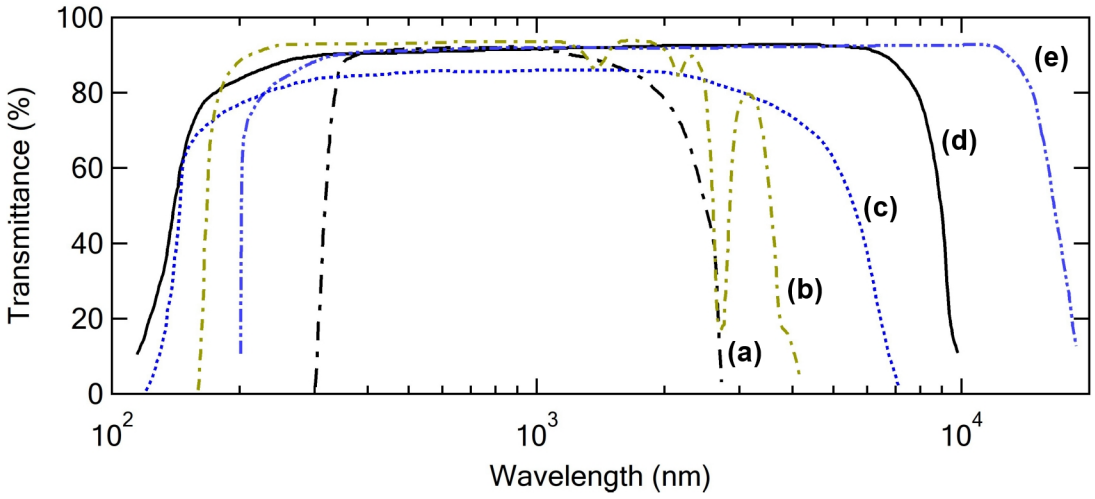

Figure 6.5. Wavelength dependence of light transmittance of several window materials at normal incidence: (a) BK7 ($d = 10$ mm), (b) Suprasil ($d = 10$ mm), (c) Sapphire ($d = 1$mm), (d) CaF_2 ($d = 10$ mm), and (e) NaCl ($d = 10$ mm). This graph was originally compiled by H.-J. Kunze, and the graph data were digitized from his book [1].

6.2.2 Mirror

An optical path consisting of mirrors and lenses, or alternatively an optical fiber, guides light to the entrance slit of a monochromator. As well as the vacuum window material, an

appropriate mirror material has to be chosen with attention considering the wavelength dependence of the reflectance. Figure 6.6 shows the reflectance of metal-coated mirrors [1]. The aluminum-coated mirror is featured with sufficient reflectance for the visible light (400 - 700 nm) and low unit cost. Therefore, aluminum-coated mirrors are used in this study.

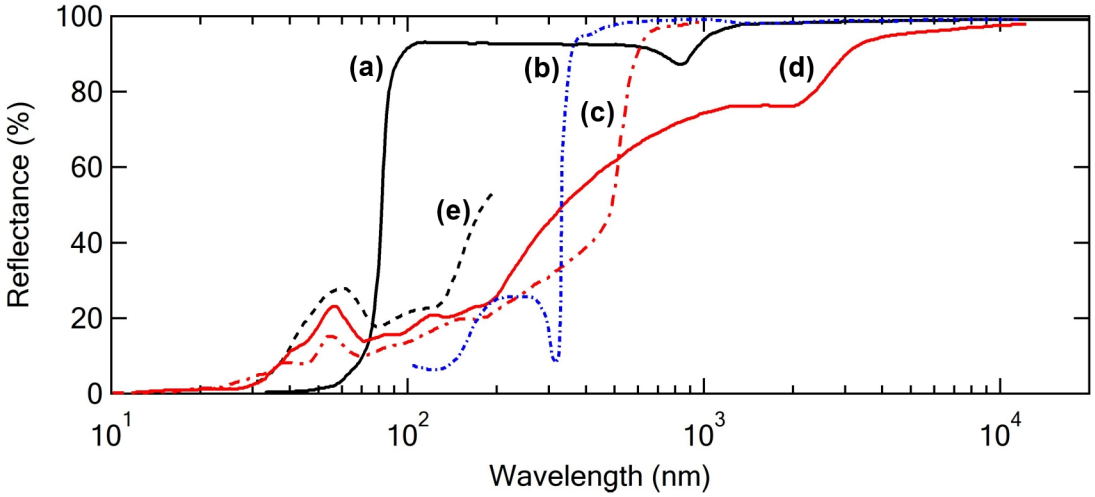

Figure 6.6. Wavelength dependence of light reflectance of metal-coated mirrors at normal incidence: (a) aluminum, (b) silver, (c) gold, (d) platinum, and (e) osmium. This graph was compiled by H.-J. Kunze, and the graph data were digitized from his book [1].

6.3 Optical System Setup and Specifications in This Study

Figure 6.7 shows the optical system constructed for the plasma spectroscopic measurements together with the schematic drawing of the magnetized plasma bombardment device. Both (a) top view and (b) side view of the system are included. Features of the plasma bombardment device are described later in Chapter 7. Three plane mirrors of 40 mm in diameter (aluminum coated, S-TFA-40C06-10 of Sigma Koki) and two plano-convex lenses of 25.4 and 25 mm in diameter (BK7 with anti-reflection coating, Lens1: SLB-25.4-500PM and Lens2: SLB-25-200PM of Sigma Koki) are utilized for the optical system in order to guide the plasma emission light to the entrance slit of the monochromator (MC-100N of Ritsu Oyo Kogaku). An actively-cooled CCD detector, S7034-1007S of Hamamatsu Photonics, is mounted at the image plane of MC-100N to record the spectral

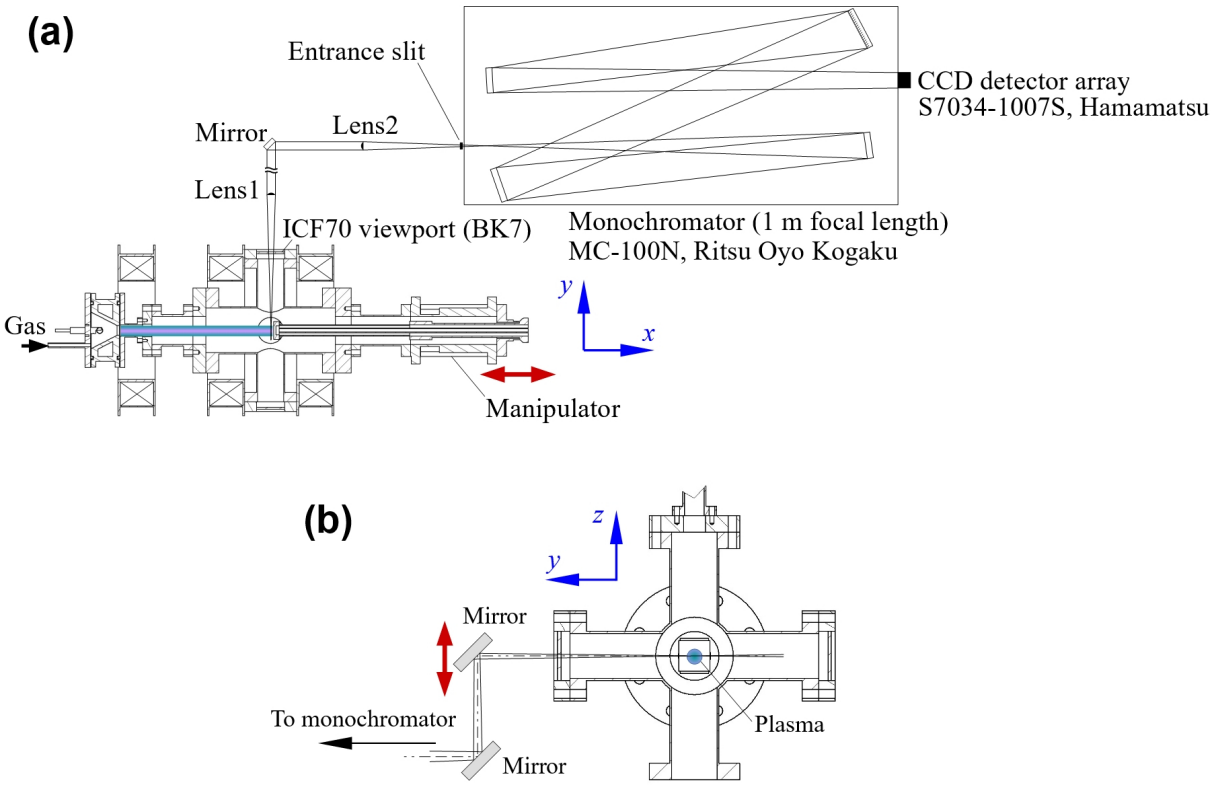

Figure 6.7. Optical system setup for the plasma spectroscopy together with the plasma-bombardment device designed for this study: (a) top view and (b) side view.

profiles. The optical system including the monochromator is constructed on a vibration controlling optical table. Two lenses, Lens1 and Lens2, are utilized to focus the light. The effective diameter of the lenses is Φ =22 mm, determined by the outer diameter of the lens holder. The focal lengths of Lens1 and Lens2 are f =500 and 200 mm, respectively. One has to pay attention to the F value which is defined as f/Φ. To prevent stray light into the monochromator, the F value of Lens2 has to be larger than that of the monochromator. The F value of the monochromator is 8.5, while that of Lens2 is calculated to be $F = 200/22 = 9.1$. In the optical path between Lens1 and Lens2, the guided light is converted into parallel light. The plane sides of the plano-convex lenses have to always face on the light source and the entrance slit of the monochromator, *i.e.*, the sides of focuses; otherwise the spherical aberration is increased dramatically. Finally, a diffraction grating (53-025BK01-300H of Richardson Gratings) mounted in the monochromator separates the plasma emission light into each spectra. The grating consists of 1800 grooves/mm, and its blazing wavelength is set at 250 nm. While the efficiency of the grating drops

in the wavelength region around 656 nm due to its short blazing wavelength as shown in Fig. 6.8(d), the Hα emission spectrum is still detectable and accurate measurements are performed with long signal integration time in this study. The focal length of the monochromator is 1 m.

As mentioned above, each optical elements have the efficiency curves, *e.g.*, the transmittance of lens and the reflectance of mirror. Figure 6.8 summarizes the efficiency curves of each elements including those of the grating and CCD used in this study. The plano-convex lenses are made of BK7, which is also used for the vacuum window. The lenses have higher transmittance because of the anti-reflection coating. The transmittance of BK7 and the reflectance of aluminum coating are almost independent to the visible light wavelength region of 400 - 700 nm, while the efficiency curves of the grating and CCD have large wavelength dependence. The efficiency of the grating monotonically decreases by approximately 20% in the wavelength region from 400 nm to 700 nm. The quantum efficiency of the CCD has arch-shaped profile with respect to the wavelength and takes the maximum around 650 nm. Later in Chapter 7, the degree of dissociation is characterized from the measured spectral intensity ratio of the hydrogen molecular Fulcher-α band spectra and atomic Hγ line spectrum. The intensities of each measured spectra are calibrated by the efficiency values at the certain wavelengths of the spectra to obtain accurate results.

A monochromator observes an emission spectrum as a form of the convolution with its intrinsic instrumental resolution function. The wavelength resolution of a monochromator is normally defined by the full width at half maximum (FWHM) of the instrumental resolution function. To characterize the wavelength resolution, Hα emission spectra from a standard hydrogen discharge tube, Spectrum Tube of Electro-Technic Products, were measured. Since the Hα line consists of multiple lines due to the fine structure of the energy levels, the characterization of the wavelength resolution involves some simple technique. In this study, the instrumental function was assumed to be a Voigt function, which is given as convolution of Gaussian and Lorentzian profiles. The instrumental function was determined by minimizing the difference between the measured Hα spectrum

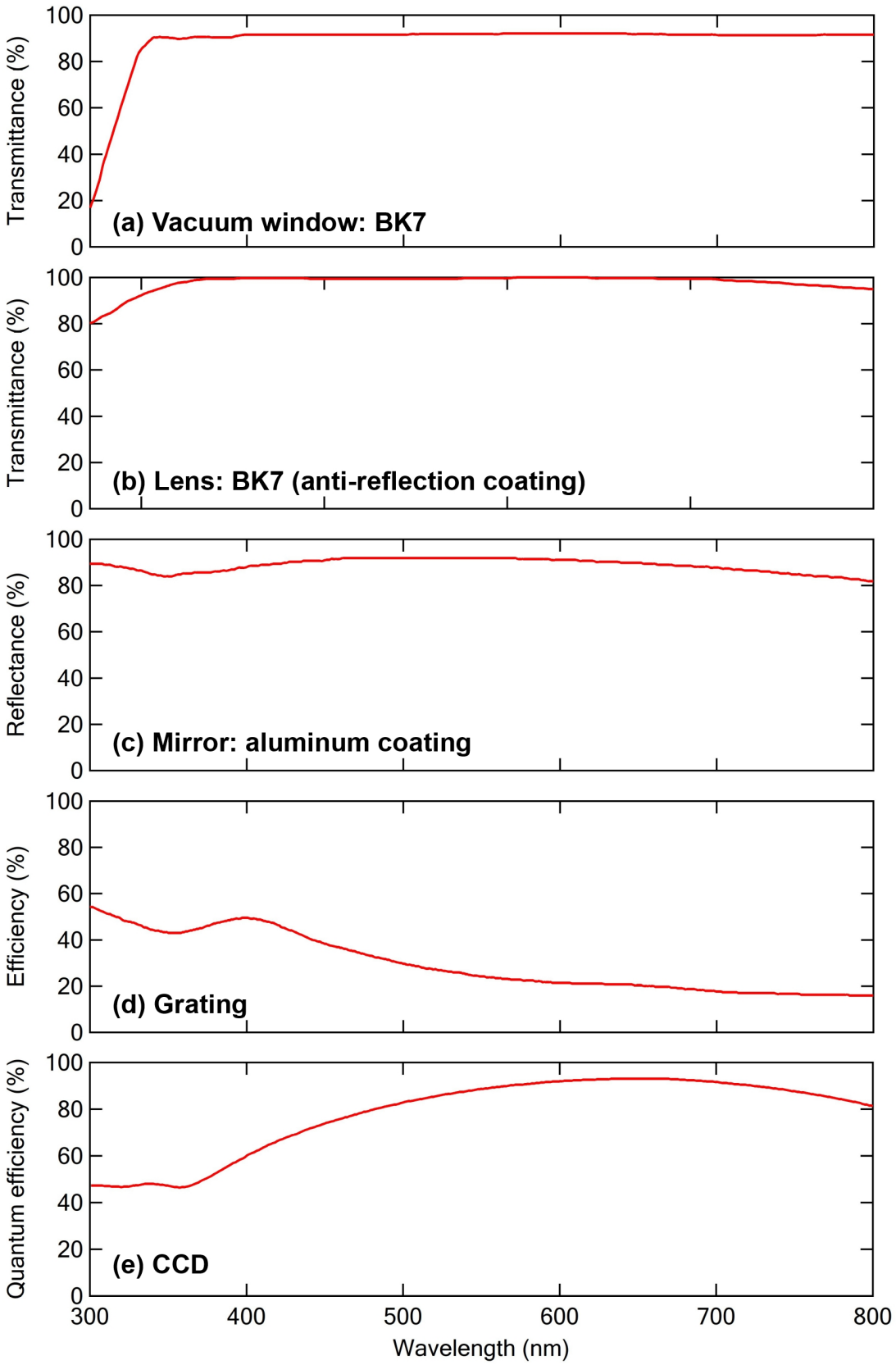

Figure 6.8. Transmittance, reflectance and efficiency curves of all optic elements comprising the optical system: (a) BK7 vacuum window, (b) BK7 lens with anti-reflection coating, (c) aluminum coating mirror, (d) grating, and (e) CCD.

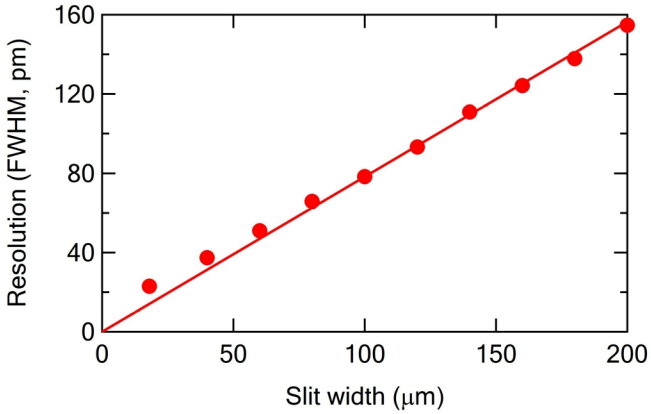

Figure 6.9. Wavelength resolution curve of the optical spectrometer, MC-100N of Ritsu Oyo Kogaku, coupled to an actively-cooled CCD detector, S7034-1007S of Hamamatsu Photonics.

and a calculated spectrum obtained from the convolution of the fine-structured lines given in Fig. 5.3 with an assumed arbitrary pseudo-Voigt function defined by a linear combination of Gaussian and Lorentzian profiles [5]. The line broadening due to the thermal motion of the hydrogen atoms was considered negligible because the optical axis of the monochromator was arranged perpendicular to the electric field in the hydrogen discharge tube. Figure 6.9 shows the entrance-slit width dependence of the wavelength resolution of the monochromator at 656.279 nm (Hα). The minimum wavelength resolution achieved was 23 pm with the slit width of 18 μm. This minimum resolution of 23 pm was selected for the Doppler spectroscopic measurement of the reflected hydrogen atoms in this study.

References

[1] H.-J. Kunze, "Chapter 3: Spectroscopic Instruments," in *Introduction to Plasma Spectroscopy*, Berlin, Heidelberg: Springer-Verlag, 2009, pp. 15–52.

[2] E. G. Loewen and E. Popov, "Chapter 2: Fundamental Properties of Gratings," in *Diffraction Gratings and Applications*, New York: Marcel Dekker, 1997, pp. 25–56.

[3] Shimadzu Corporation, 'Free Spectral Range', 2017. [Online]. Available: `http://www.shimadzu.com/opt/guide/diffraction/06.html`. [Accessed: 17- Nov- 2017].

[4] Hamamatsu Photonics K.K., Solid State Division, "Characteristics and use of FFT-CCD area image sensor," 2003.

[5] T. Ida, M. Ando, and H. Toraya, "Extended pseudo-Voigt function for approximating the Voigt profile," *J. Appl. Crystallogr.*, vol. 33, no. 6, pp. 1311–1316, Dec. 2000.

Chapter 7

Plasma-Bombardment Device for Spectroscopic Measurement of Particle Reflection at a Metal Surface

7.1 Introductory Remarks

In previous Chapter 5 and 6, the principles of the light emissions in a plasma and the optical spectroscopic instruments were provided. This chapter describes the general structure of the plasma bombardment device designed for the Doppler-spectroscopic measurement of the reflected hydrogen atoms in low incident particle energy range less than a few 100 eV. While the final device concept converged in use of a linear magnetized plasma, several other concepts had been examined during the phase for designing the plasma bombardment device. The attempt to spectroscopically detect the reflected atoms started with the concept of low energy ion beam bombardment using a hollow anode ion source as shown in Fig. 7.1. A stable hydrogen plasma can be formed by hot-cathode discharge in the multicusp magnetic chamber, and electrons in the plasma are attracted to the inside of the hollow anode, resulting in the ionization of H_2 gas in the hollow anode. The

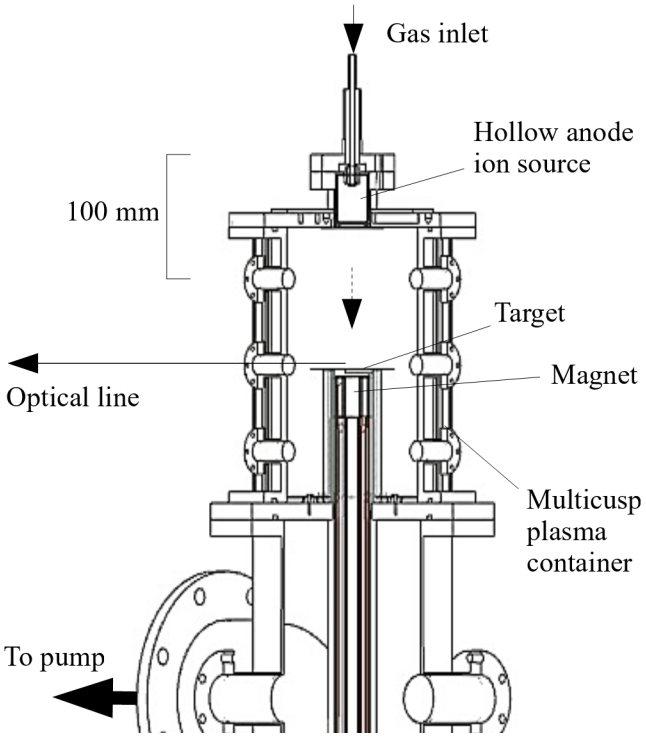

Figure 7.1. Design of the low-energy ion bombardment device.

hydrogen ions ionized in the hollow anode can be extracted with energy given by the applied positive potential of the anode and injected onto the W target. The space charge effects on the extracted ions could be expected to be small in the distance of ∼100 mm to the target surface. A monochromator observes Hα spectra in the vicinity of the target surface. However, the spectral component of reflected atoms in Hα emission spectrum could not be observed in this experiment. It was soon deduced that the ion flux extracted to the target surface was extremely low. Very few reflected atoms exist in the vicinity of the target surface compared to atoms in the plasma container; the background signal erased the contribution from the reflected atoms. To enhance the number of ions incident onto the target surface, the author devised a method based on the direct immersion of a target into a plasma. A negative bias potential on the target accelerates the ions across the sheath. This direct plasma bombardment finally resulted in the successful detection of the contribution from the reflected atoms. Following sections in this chapter present the general structure of the plasma bombardment device and characterizations of the plasma parameters.

7.2 Detailed Design of the Device

Figure 7.2 shows the magnetized-plasma bombardment device together with the electric-connection diagram. A spatially-constricted linear magnetized plasma can be formed in a vacuum chamber as shown in Fig. 7.2(b). The base pressure of 1.0×10^{-4} Pa is achieved in the plasma-bombardment chamber by use of a vacuum system consisting of a turbomolecular pump and an oil-sealed rotary pump. DC hot-cathode discharge using a W filament of ϕ0.4 mm in diameter produces a stable plasma. Two DC power supply

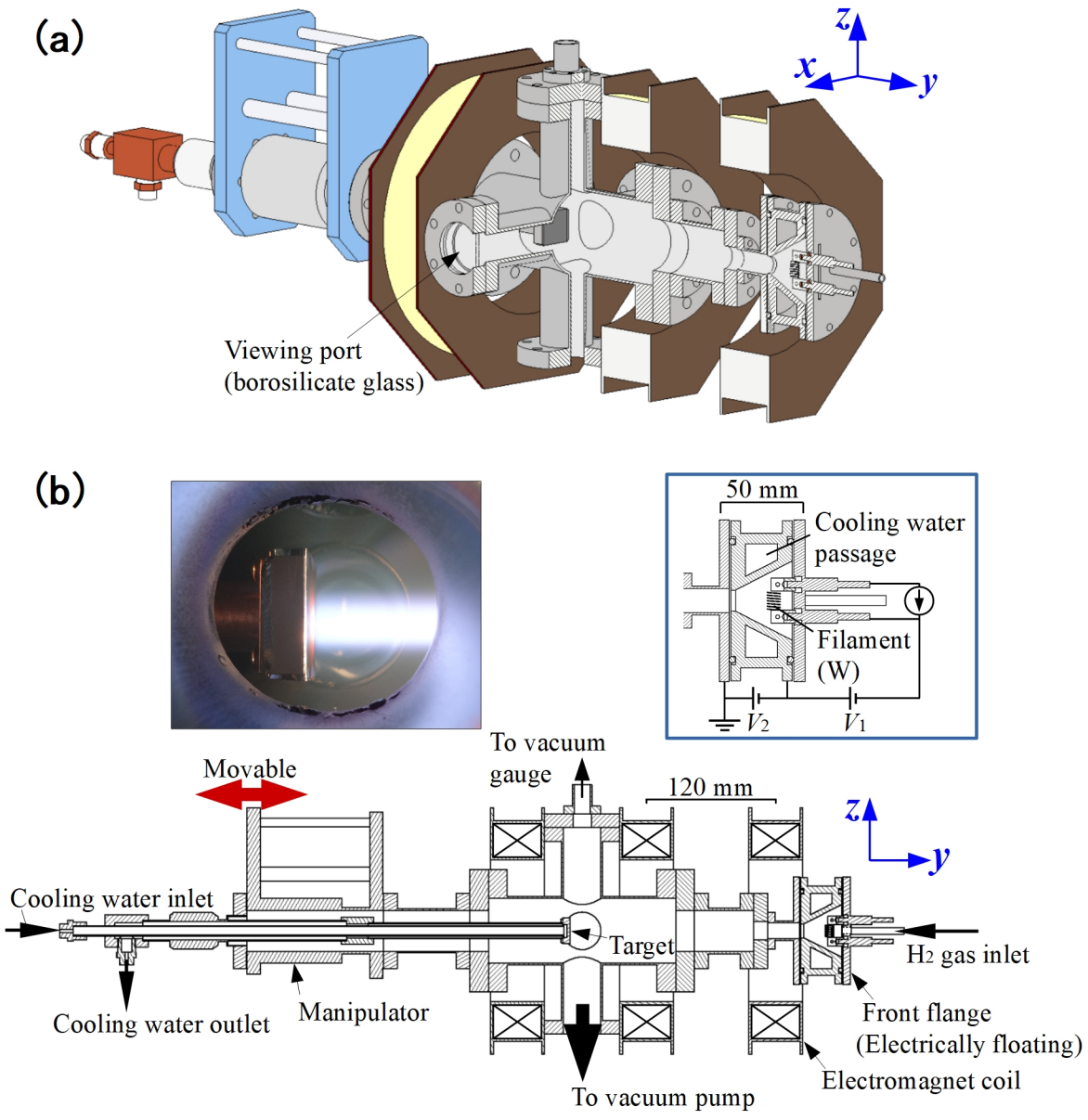

Figure 7.2. Design of the magnetized-plasma bombardment device in (a) 3D and (b) 2D sectioned views together with the electric-connection diagram.

are used to generate the hydrogen gas discharge and to extract the produced electrons to the plasma-bombardment chamber. Three electromagnet coils arranged in parallel form linear magnetic field lines which extend energetic electrons from the plasma cathode. The magnetic field intensity produced is represented by the relation $B = 5.6 \times I$ (mA), where I is current (A) in the series circuit of the electromagnet coils. A water-cooled target holder fixes a sample in the cylindrical-shaped magnetized plasma of ϕ15 mm in diameter. The target holder is equipped with a linear vacuum manipulator so that the target position in the plasma can be adjusted along the magnetic field lines. A viewing port of BK7 (borosilicate) is equipped on an ICF70 flange for the optical spectroscopic measurement.

7.3 Evaluation Methods for Plasma Parameters

7.3.1 Langmuir Probe

Langmuir probe is one of the fundamental and simplest methods to measure plasma parameters. Langmuir and Mott-Smith first proposed the plasma-diagnostic method based on an electrostatic probe in 1926 [1]. The Langmuir probe is a very small size electrode immersed and biased in a plasma to extract electron and ion currents. The electron and ion current dependence on the probe bias potential is so-called the I-V characteristic curve, which is determined by velocity and density of both electrons and ions attracted to the probe surface across the sheath. One can obtain plasma parameters, *e.g.,* electron temperature and density, from the analysis of the I-V characteristic curve. It is assumed that the bias potential on the probe does not affect the plasma density largely, and effects of the probe are limited within the probe vicinity, *i.e.*, sheath, because the probe current is always negligibly small in use of an ideal electrostatic probe.

The Langmuir probe used in this study has four-layer structure as shown in Fig. 7.3. The probe head is made of tungsten (W) wire of ϕ0.6 mm in diameter. An alumina (Al_2O_3) ceramic tube covers unexposed part of the W tube to define the surface area (S_p) of the probe head. The defined 2.4 mm end-top part of the W wire is exposed to the plasma. It is important to define S_p because it is one of coefficients in the electron density calculation

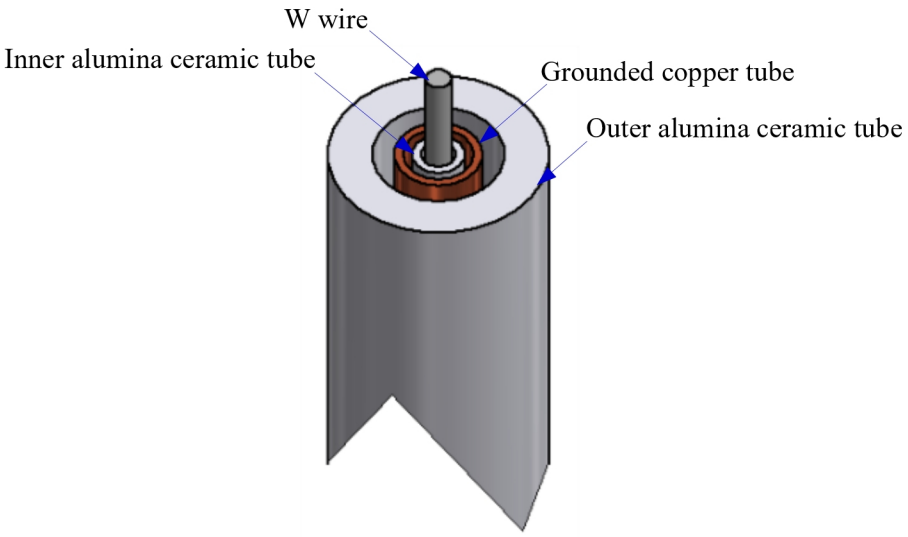

Figure 7.3. Structure of the Langmuir probe used in this study.

in Eq. 7.5 as described below. A grounded copper (Cu) tube shields the ceramic-covered W wire from electric noise due to the plasma. Another Al_2O_3 ceramic tube with larger diameter is used to protect the probe from the plasma particle radiation.

The probe current, I_p, is recorded when the probe voltage is swept linearly from -30 V to 30 V. A typical I-V characteristic curve measured in hydrogen plasma is shown in Fig. 7.4. The notations I_i and I_e represent the ion and electron currents, respectively. The floating potential, V_f, is literally defined as the voltage at $I_p = 0$. In $V < V_f$, the probe collects ions, I_i, from the plasma. The probe current, I_p, increases due to electrons in $V > V_f$ and saturates at the space potential of the plasma, V_s. Here, I_{e0} is so-called the electron saturation current. Theoretically, the electron current, I_e, at electron-repelling potential ($V_f \leq V_p \leq V_s$) can be written in the form [2]:

$$I_e(V_p) = \frac{en_eS_p}{4}\int_{eV}^{\infty}\left(1-\frac{eV_p}{E}\right)\sqrt{\frac{2E}{m_e}}F(E)dE, \tag{7.1}$$

where e, n_e, m_e are electron charge, density, and mass, respectively, and $F(E)$ is the electron energy probability function (EEPF). Normally, the EEDP is Maxwellian [2, 1]:

$$F(E) = \frac{2\pi\sqrt{E}}{\sqrt[3]{\pi kT_e}}\exp\left(-\frac{E}{kT_e}\right), \tag{7.2}$$

which allows for the determination of the electron density. One can substitute the

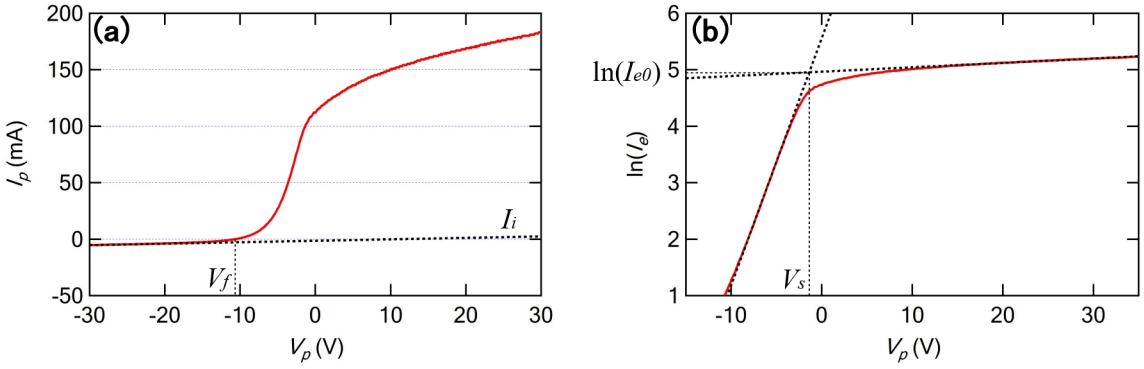

Figure 7.4. An example of probe I-V curve measured in a magnetized hydrogen plasma.

Maxwellian distribution function in Eq. 7.1 to obtain [2]:

$$I_e(V_p) = en_eS_p\sqrt{\frac{kT_e}{2\pi m_e}}\exp\left(-\frac{e(V_s - V_p)}{kT_e}\right). \tag{7.3}$$

Since $I_p = I_{e0}$ at $V_p = V_s$, the electron saturation current can be expressed in the form [2]:

$$I_{e0} = n_eeS_p\sqrt{\frac{kT_e}{2\pi m_e}}. \tag{7.4}$$

Finally, we get the electron density [3]:

$$n_e(\mathrm{cm}^{-3}) = 3.73\times10^{10}\frac{I_{e0}(\mathrm{mA})}{S_p(\mathrm{mm}^2)\sqrt{T_e}(\mathrm{eV})}. \tag{7.5}$$

Here, T_e is the electron temperature, which can be obtained from the analysis of $\ln(I_e) - V_p$ plot. At the electron-repelling potential ($V_f \le V_p \le V_s$), we have obtained an equation for I_e in Eq. 7.1. The derivative of $\ln(I_e)$ with respect to V_p is written in the form:

$$\frac{d\ln(I_e)}{dV_p} = \frac{e}{kT_e}. \tag{7.6}$$

The reciprocal of the slope of $\ln(I_e) - V_p$ plot at the electron-repelling region gives the electron temperature, kT_e/e (eV) [2, 3].

7.3.2 Spectroscopic Measurement of Degree of Dissociation

Plasma spectroscopy is the easiest method to measure the degree of dissociation of H_2 molecules in a plasma. Both atoms and molecules can be excited in plasma, resulting in radiations of line emission spectra as described in Chapter 5. The intensity ratio of atomic and molecular emission spectra well reflects the degree of dissociation [4, 5]. While atoms and molecules in a plasma radiate several spectral lines depending on the energy level transitions, Fantz *et al.* showed that the hydrogen atomic Hγ line and Q-branch of H_2 molecular Fulcher-α band are the most proper selection for the determination of the degree of dissociation because the ratio of the effective emission rate coefficients of Hγ and the Fulcher-α band is independent of T_e and its dependence on n_e is also negligibly small [5]. Figure 7.5 shows the Fulcher-α band spectra observed from the magnetized hydrogen plasma. The intensity of Q-branch of the Fulcher-α band, I_{FUL}, is given as the summation of integrated intensities of each spectra in Fulcher-α band for $v = 0 - 3$:

$$I_{FUL} = \sum_{v=0}^{3} \sum_{J=1}^{5} \int I_{a,v,J}^{d,v,J}(\lambda) d\lambda, \tag{7.7}$$

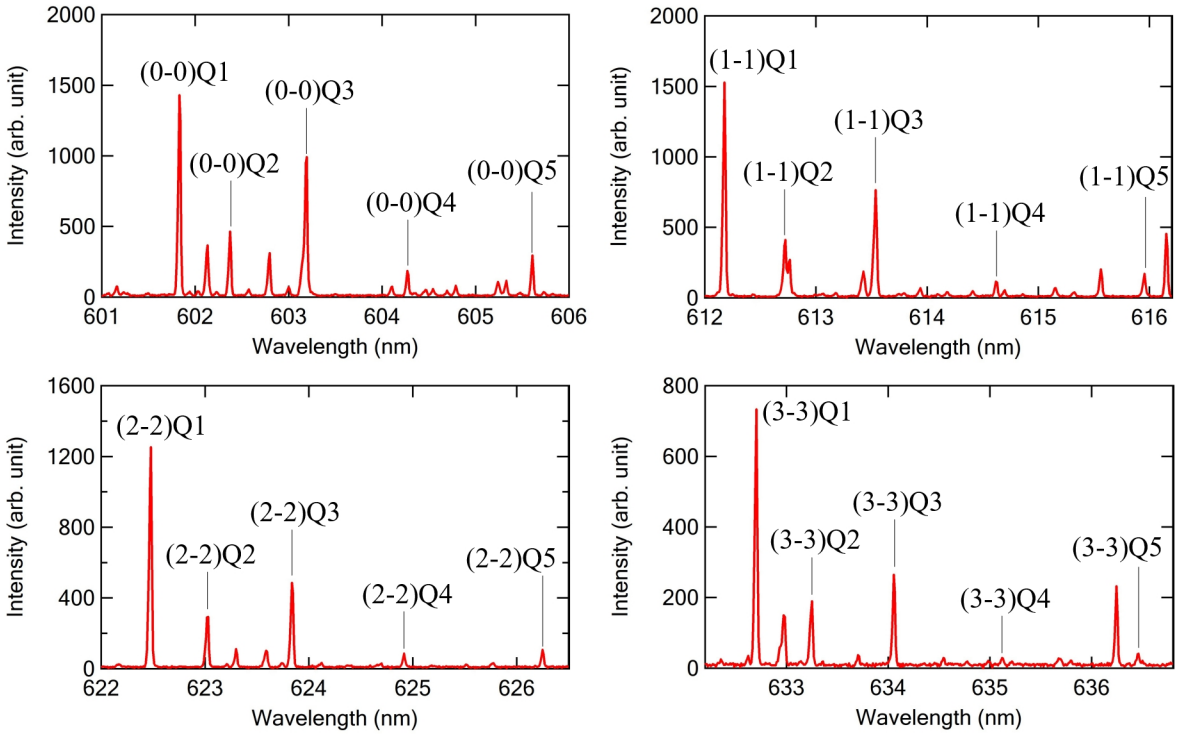

Figure 7.5. Fulcher-α band spectra measured in a magnetized hydrogen plasma.

where $I^{d,v,J}_{a,v,J}$ is an observed spectrum emitted in a molecular electric transition from $(d^3\prod_u^-, v, J)$ to $(a^3\prod_g^+, v, J)$. The ratio of the integrated intensity, I_γ, of Hγ and I_{FUL} is expressed in the relation [4]:

$$\frac{I_\gamma}{I_{FUL}} = \frac{X^{eff}_\gamma}{X^{eff}_{FUL}} \frac{n_H}{n_{H_2}} \tag{7.8}$$

with $X^{eff}_\gamma / X^{eff}_{FUL}$, which is the ratio of the effective emission rate coefficients of Hγ and Q-branch of the Fulcher-α band. The value of $X^{eff}_\gamma / X^{eff}_{FUL}$ is known to be ∼1.3 [4, 5]. So we can obtain the ratio of atom and molecule density, n_H/n_{H_2}, and the degree of dissociation is given by [4]:

$$(Degree\ of\ dissociation) = \frac{0.5 n_H/n_{H_2}}{1 + 0.5 n_H/n_{H_2}}. \tag{7.9}$$

7.4 Measured Plasma Parameters

In this study, the discharge voltage and power are fixed at $I_2 = 2.0$ A with $V_2 = 70$ V (140 W) and $V_1 = 70$ V, while the magnetic field intensity is set at $B = 28$ mT. It is reasonable to set the discharge voltage at ∼70 V because the electron impact ionization cross section of hydrogen atoms takes the maximum at the electron energy of ∼70 eV [6]. In order to find the most efficient gas pressure of H_2 with the discharge setting described above, the degree of dissociation was spectroscopically measured as a function of the gas pressure.

Figure 7.6 shows the degree of dissociation spectroscopically measured together with the intensity ratio of atomic Hβ and Hγ line emission spectra. It is known that the intensity ratio of atomic Hβ/Hγ well reflects the electron density [5]. Whereas Langmuir probe measurement yields electron density in the absolute unit (cm^{-3}), the gas pressure dependence of the electron density was characterized in relative unit from the intensity ratio of Hβ/Hγ. Energetic electrons from the plasma cathode heat the probe up to intolerable temperature causing W probe head melting or alumina ceramic tube sublimation in case of low gas pressure discharge, where the energetic electrons can reach the probe surface by exceeding the sheath formed in the vicinity of the probe surface without colliding with neutral gas molecules. In the magnetized plasma bombardment device shown in Fig. 7.2,

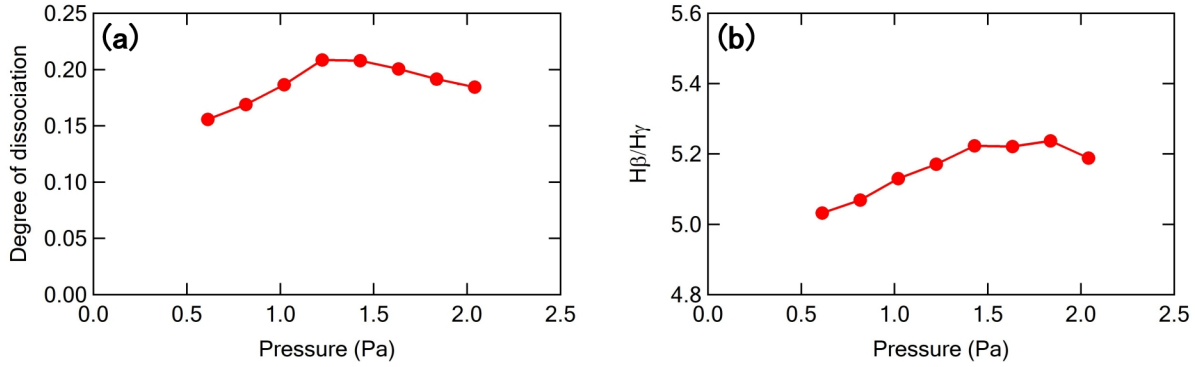

Figure 7.6. H_2 gas pressure dependence of (a) spectroscopically measured degree of dissociation and (b) hydrogen atomic line intensity ratio of Hβ/Hγ. It is known that the intensity ratio of Hβ/Hγ well reflects the electron density [5].

the Langmuir probe could be utilized for the plasma parameter measurement in high gas pressure discharge at greater than 1.0 Pa.

The measured results indicate that the degree of dissociation takes the maximum at ∼1.2 Pa, while the electron density takes the maximum at slightly higher gas pressure of ∼1.6 Pa. The electron-impact ionization of hydrogen atoms and molecules produces free electrons in the plasma. If the gas pressure is lower than the sufficient pressure where the ionization takes place most efficiently, highly energetic electrons extracted from the plasma cathode survive without colliding with the molecules. On the other hand, if the gas pressure is too high, collisions with gas molecules reduce the energy of extracted electrons soon at the immediate downstream of the plasma cathode. Both cases above result in less ionization and low degree of dissociation. The degree of dissociation needs to be as high as possible since the aim of this study is to investigate the reflection of single atomic hydrogen particles at a metal surface. Therefore, the gas pressure of 1.2 Pa is selected for the hydrogen reflection measurements discussed in later chapters. The discharge at 1.2 Pa produces a hydrogen plasma with the electron density of $n_e = 4 \times 10^{11}$ cm^{-3} at the electron temperature of $T_e = 3.0$ eV, obtained from the Langmuir probe measurement at the central axis of the plasma column.

References

[1] H. M. Mott-Smith and I. Langmuir, "The Theory of Collectors in Gaseous Discharges," *Phys. Rev.*, vol. 28, no. 4, pp. 727–763, Oct. 1926.

[2] H. Amemiya, M. Wada, H. Toyoda, K. Nakamura, A. Ando, K. Uehara, K. Oyama, O. Sakai, and K. Tachibana, "Probe Measurements: Fundamentals to Advanced Applications (in Japanese)," it J. Plasma Fusion Res., vol. 81, no. 7, pp. 482–525, Sep. 2005.

[3] J. Ishihara, " Ion gen kougaku [Ion source engineering]," Tokyo: Aionikusu, May 1986, p. 313.

[4] J.-J. Dang, K.-J. Chung, and Y. S. Hwang, "A simple spectroscopic method to determine the degree of dissociation in hydrogen plasmas with wide-range spectrometer," *Rev. Sci. Instrum.*, vol. 87, no. 5, p. 053503, May 2016.

[5] U. Fantz, H. Falter, P. Franzen, D. Wünderlich, M. Berger, A. Lorenz, W. Kraus, P. McNeely, R. Riedl, and E. Speth, "Spectroscopy—a powerful diagnostic tool in source development," *Nucl. Fusion*, vol. 46, pp. S297–S306, May 2006.

[6] R. K. Janev, W. D. Langer, K. Evans, Jr., and D. E. Post, Jr., *Elementary Processes in Hydrogen-Helium Plasmas*. Berlin, Heidelberg: Spinger-Verlag, 1987.

Chapter 8

Doppler-Spectroscopic Detection of Hydrogen Atoms Reflected from a Metal Surface under Plasma Bombardment

8.1 Introductory Remarks

The previous chapter presented general features of the plasma-bombardment device designed for the optical spectroscopic detection of the reflected atoms at a sample surface. Hα emission spectra originating from the reflected atoms are measured by using an optical spectrometer. Experimentally, however, a challenging matter is to detect the contribution from the particles reflected from a sample surface under the plasma bombardment. Bright optical emission from the background plasma can erase the faint signal from the reflected atoms. This chapter presents the signal-to-noise ratio enhancement for the detection of the contribution from the reflected hydrogen atoms in a Hα emission spectrum. The measured profiles are compared with reconstructed spectra by Monte Carlo simulations using the ACAT code [2]. This chapter has also been submitted for publication as Ref. [1].

8.2 Experiment

The plasma-bombardment device used for this experiment is shown in Fig. 8.1 with the line of sight of the monochromator and a coordinate system defined on the W target. A 15 mm diameter hydrogen plasma sustained by a linear magnetic field struck a W target. Three electromagnet coils formed the magnetic field of 28 mT in the center region of the vacuum vessel where the linear plasma was produced. The discharge parameters were kept constant at $I_2 = 2.0$ A with $V_2 = 70$ V (140 W) with the gas pressure of 1.2 Pa (H_2) throughout the measurements. The discharge voltage V_1 was also fixed at 70 V. A hydrogen plasma was produced with the electron density of 4×10^{11} cm^{-3} and the electron temperature of 3.0 eV measured by a Langmuir probe. The plasma potential ranged from 0 to 0.5 V depending on the bias potential of the target.

Two types of target holders were prepared for the plasma bombardment onto a W target as shown in Fig. 8.1(b-c). By using *Target Holder 1* (Fig. 8.1(b)), a 0.05-mm thick W target can be immersed into the plasma with the angle of the surface normal to the target at 0° to the magnetic field lines. Here, it is noted that *Target Holder 1* can fix a flexible film-form target only. By using *Target Holder 2* (Fig. 8.1(c)), on the other hand, a 0.2-mm thick W target can be exposed to the plasma with the angle of the surface normal to the target at 45° to the magnetic field lines. Negative bias was applied to the target in order to control the energy of hydrogen ions incident onto the surface from the magnetized plasma; the incident hydrogen ions were accelerated across the sheath. The target holder was water-cooled, but the surface temperature of the W target increased up to approximately 1080 K due to the intense heat flux from the magnetized plasma.

A Czerny-Turner type visible range monochromator, MC-100N of Ritu Oyo Kougaku, was used to observe the Hα spectra in the vicinity of the W surface. Arrangement of the optical axis looking into the target surface causes a serious increase of the background light due to the optical reflection at the target surface. Therefore, in this study, the line of sight was aligned parallel to the target surface so as to measure the symmetrical Doppler broadening of the spectra due to the velocity components of energetic reflected atoms along the line of sight. The monochromator viewed an area of 2 mm height with 30 μm width

as shown in Fig. 8.1(b-c). An actively-cooled CCD sensor, S7034-1007S of Hamamatsu Photonics, was used as a detector. The wavelength resolution was set to be 23 pm.

The spatial dependence of the intensities of the Doppler spectra could be measured by adjusting the target and mirror positions. Mirror1 was movable along the direction perpendicular to the magnetic field lines. The target holder was set on a linear manipulator and thus the target was also movable along the magnetic field lines.

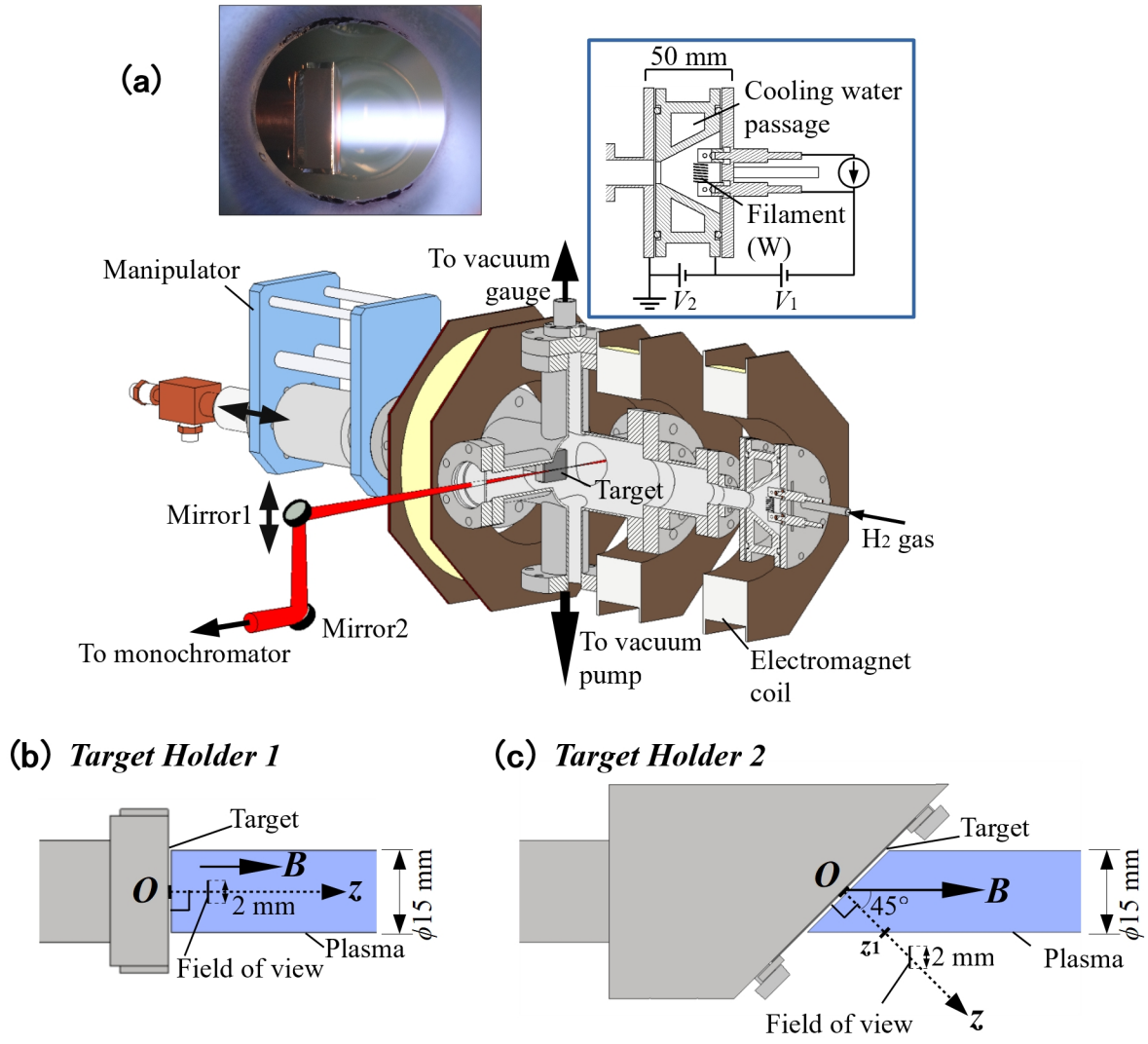

Figure 8.1. (a) Schematic drawing of plasma-bombardment device together with the line of sight of the monochromator. (b-c) Two different target holders with the angle of the surface normal to the target at (b) 0° and (c) 45° from the magnetic field lines. The monochromator viewed an area of 2 mm height with 30 μm width at an arbitrary point on the z axis. The edge point of the plasma, z_1 in (c), can be geometrically calculated from the plasma diameter, ϕ15 mm, to be $z_1 = 10.6$ mm

8.3 Results: Hα Spectra in the Vicinity of W Surface under Plasma Bombardment

Figure 8.2 shows Hα spectra measured at $z = 3$ mm vertically away from the W surface under the hydrogen-plasma bombardment with the bias potentials of (a) floating potential (-20 V), (b) $V_b = -150$ V, and (c) $V_b = -300$ V. The surface normal of the W target was set parallel to the magnetic field lines by using *Target Holder 1*. Dashed lines represent the full spectra and solid lines are the ordinate-scale enlarged spectra to see the weak Doppler-broadened signals originating from the reflected atoms.

A weak Doppler-broadened component appeared at the bottom of the measured Hα

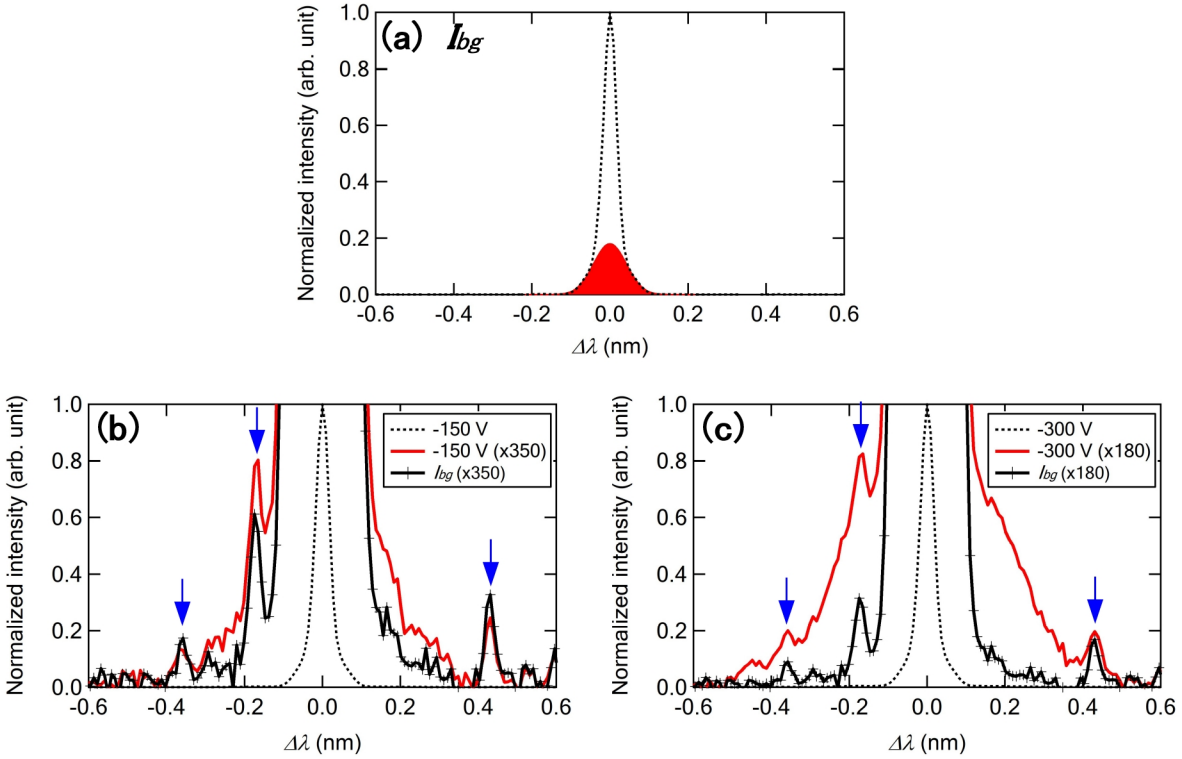

Figure 8.2. Measured Hα emission spectra in the vicinity of the W surface at $z = 3$ mm for several bias potentials: (a) floating potential (-20 V), (b) $V_b = -150$ V, and (c) $V_b = -300$ V. The W target was fixed in the plasma with the angle of the surface normal parallel to the magnetic field lines using *Target Holder 1*. Dashed lines represent the full spectra and solid lines correspond to the expanded views. Background spectrum, I_{bg}, measured at floating potential (-20 V) on the target is also displayed by solid lines with cross markers. Sharp peaks (arrowed) are emission lines of the excited-hydrogen molecules. The exposure time to record one spectrum was 2.5 s.

spectra when negative bias potentials were applied on the target (see solid lines in Fig. 8.2). This symmetrical Doppler broadening is considered to originate from the reflected atoms. Indeed, narrower broadening was observed for lower incident energy case of $V_b = -150$ V as seen in the comparison of Fig 8.2(b-c). However, the emissions from the plasma reduced the signal-to-noise ratio and complicated the evaluation of the pure contribution from the reflected atoms. A sharp prominent main peak at $\Delta\lambda = 0$ nm belongs to the hydrogen atoms excited in the plasma. It is known that electron impact dissociative excitation of H_2 molecules results in a symmetrical Doppler component due to fast atoms created via the repulsive state of H_2 molecules [3]. The measured spectra also contain this effects as shown in Fig. 8.2(a); it is represented by the solid area with the peak intensity less than 20% of the main peak. The intensity of the contribution from the reflected atoms accounts only for less than 1% of that of the background emission. Additionally, three other sharp peaks are superimposed on the contribution from the reflected atoms in Fig. 8.2. These spectra originate from excited H_2 molecules as shown in the data table by G. H. Dieke [4]. The spectra summarized in Dieke's data table were reconstructed by convolution with the instrumental resolution function of the monochromator used in this

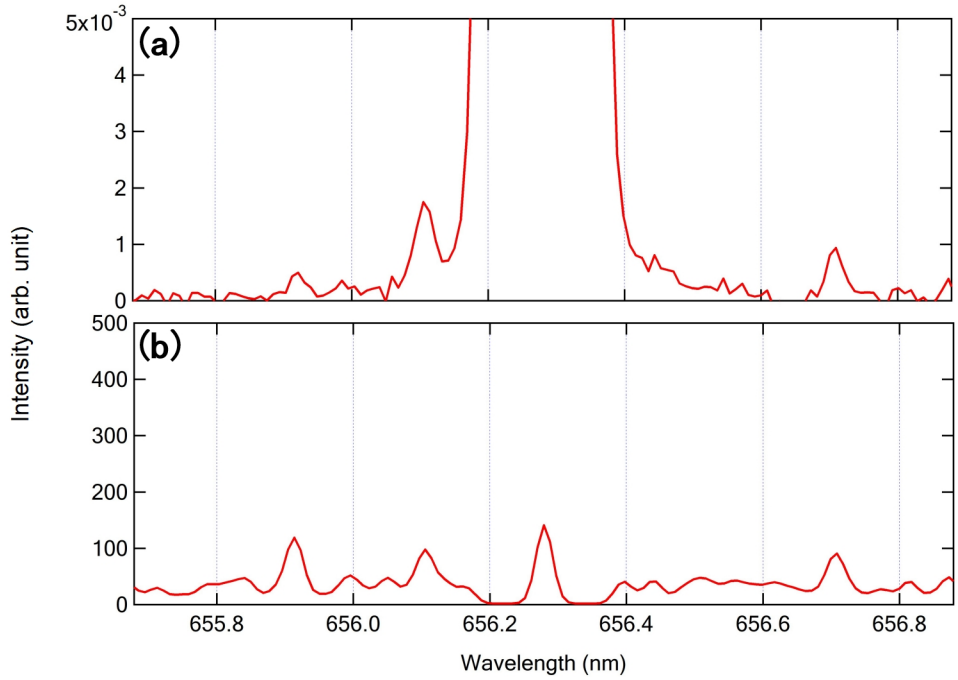

Figure 8.3. Comparison of (a) measured H_2 molecular emission lines near Hα peak and (b) reconstructed H_2 emission spectra from Dieke's wavelength table.

study. Figure 8.3 shows the comparison of the reconstructed spectra with the measured spectra at the floating potential on the target. One can confirm that the wavelength positions of the measured sharp peaks originating from H_2 molecules well agree with those obtained from the reconstruction of Dieke's data. Actually, the Doppler-broadened spectra in Fig. 8.2(b-c) contain two components resulted from the reflected atoms produced by both H^+ and $H_2{}^+$ ion incidence. These components can be distinguished clearly by the measurements with enhanced signal-to-noise ratio described later.

8.4 Discussion

8.4.1 Enhancement of the Signal-to-Noise Ratio

When the metal surface ejects an incident hydrogen particle, the backscattered hydrogen atom can be neutralized and even excited due to single-electron transfer from the surface [5]. The probabilities of the excited states depend on the solid materials and the velocity of the reflected atoms. Spectroscopic measurements performed by Tanabe *et al.* confirmed the presence of the reflected hydrogen atoms in the $n \geq 3$ energy levels in relatively high incident particle energy region [6]. H^+ ion beam at energy range from 5 to 25 keV was injected onto metal surfaces in vacuum, and the Doppler-broadened atomic radiations from the backscattered particles were observed [6]. The excited state distributions of the reflected hydrogen atoms at metal surfaces including W were calculated by numerical simulations by Kato *et al.* [7]. Their calculation results indicated that almost none of the reflected hydrogen atoms at W and Mo surfaces can be excited to the $n = 3$ level in the energy region less than 300 eV by the single-electron transfer from the surface. On the other hand, the Hα spectra observed in this study suggest that some part of the reflected was actually excited to the $n = 3$ level, resulting in the Doppler-broadened tail of the Hα spectra.

In this study, the spatial distribution of the contribution from the reflected hydrogen atoms was investigated by changing the W target surface position along the magnetic field lines in the plasma. The *Target Holder 1* was used for this measurement. A spectrum

measured at $z = 20$ mm away from the W surface is shown in Fig. 8.4 together with a spectrum at $z = 3$ mm and I_{bg}. The Doppler-broadened component at the bottom of the spectrum survived even at $z = 20$ mm with intensity approximately more than half of that at $z = 3$ mm. Here, one has to note that the hydrogen atoms in the $n = 3$ level with kinetic energy of 300 eV traverse relatively short distance of the order of ∼5 mm with the radiative lifetime of ∼20 ns [8]. The spatially extended Doppler-broadened component indicates that the reflected atoms are populated to the $n = 3$ level mostly by local excitations other than the single-electron transfer at the surface.

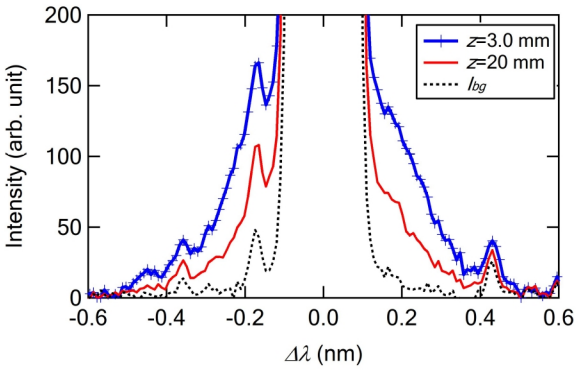

Figure 8.4. Measured Hα emission spectra in the vicinity of W surface at different positions from the target surface together with the background spectrum, I_{bg}, measured with floating potential (−20 V) on the target. The *Target Holder 1* was used. The target was negatively biased at $V_b = -300$ V. The exposure time to record one spectrum was 2.5 s.

The local excitation of the reflected atoms allows for the signal-to-noise ratio enhancement by the observation at the region outside of the plasma column which dramatically reduces the background signals. A new target holder, *Target Holder 2*, in Fig. 8.1(c) was introduced for the measurements outside of plasma. The surface normal of *Target Holder 2* is inclined at 45° with respect to the magnetic field lines (refer to Fig. 8.1(c)). Figure 8.5 shows Hα spectra measured at (a-b) $z = 2.8$ and (c-d) $z = 15.6$ mm vertically away from the target surface with different bias potentials of (a,c) $V_b = -150$ V and (b,d) $V_b = -300$ V. The Doppler-broadened component originating from the reflected atoms spatially extended to the outside of the plasma column. The local excitation most likely due to collisions with H_2 molecules maintained the emissions of the reflected atoms. Since less excitations of hydrogen atoms and molecules take place at the plasma peripheral region,

the signal-to-noise ratio of the contribution by the reflected atoms against the background signals was largely enhanced. Now the Doppler-broadened component of the reflected atoms accounts for ∼10% of the intensity of the central background peak. The measured

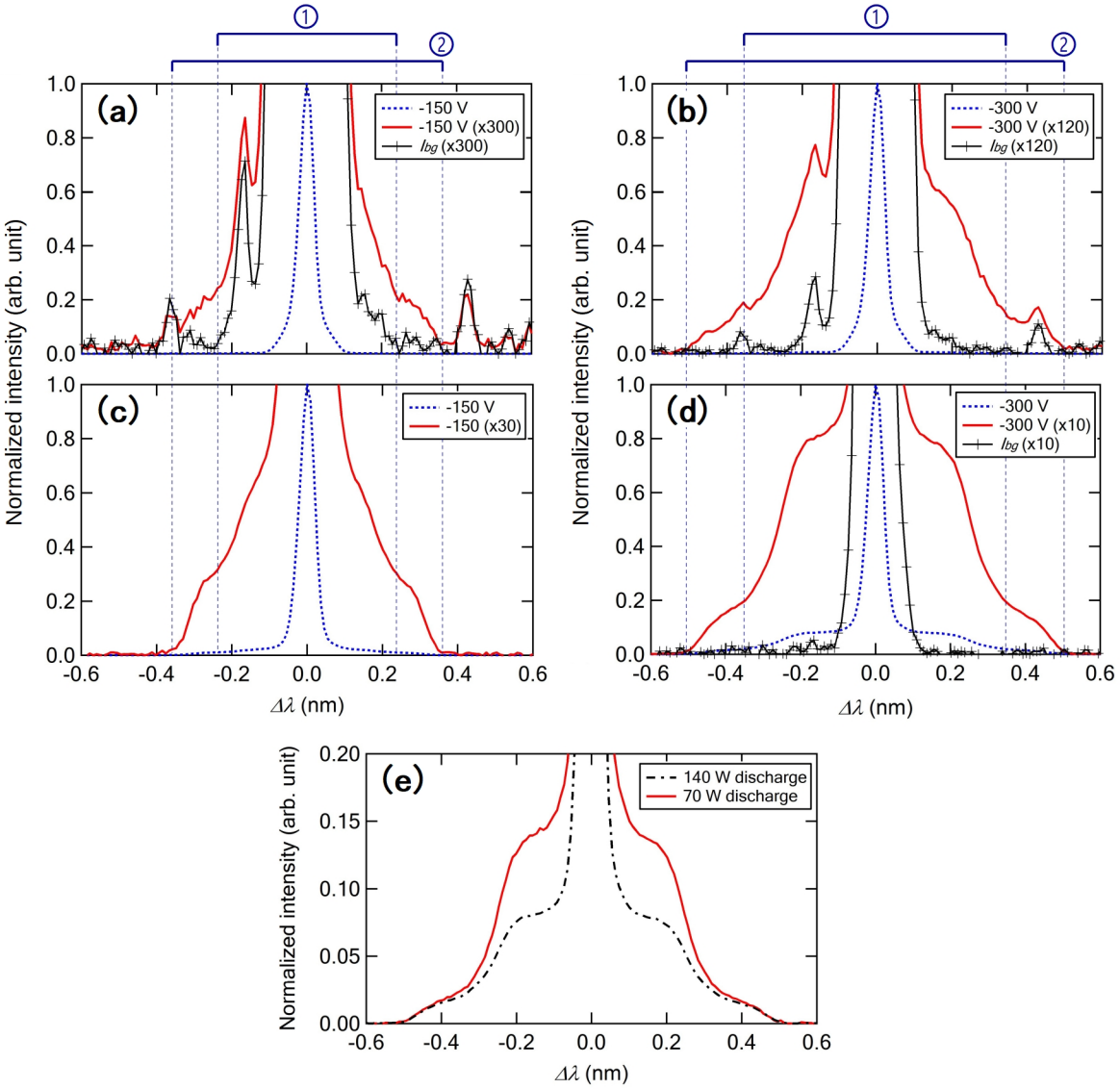

Figure 8.5. Measured Hα emission spectra in the vicinity of W surface at (a-b) $z = 2.8$ mm and (c-d) $z = 15.6$ mm. The W target was immersed in the plasma with the angle of the surface normal at 45° from the magnetic force lines using the *Target Holder 2*. Spectra measured at two different target bias potential are compared: (a,c) measured with $V_b = -150$ V, and (b,d) $V_b = -300$ V. Dashed lines represent the full spectra and solid lines correspond to the expanded views. Background spectrum, I_{bg}, measured at floating potential (−20 V) on the target is also displayed by solid lines with cross markers. (e) The Doppler-broadened Hα emission spectra at $z = 15.6$ mm with $V_b = -300$ V for the discharge powers of 70 and 140 W. The exposure time to record one spectrum was 2.5 s at (a-b) $z = 2.8$ mm and 60 s at (c-e) $z = 15.6$ mm.

spectra with high signal-to-noise ratio indicate that the Doppler-broadened components have bell-shaped structure which can be separated into two groups. Reflected atoms produced by $H_2{}^+$ ion incidence contribute to the inner part (①) of the bell-shaped component at $|\Delta\lambda| \leq 0.26$ nm for $V_b = -150$ V and $|\Delta\lambda| \leq 0.37$ nm for $V_b = -300$ V. The incident H_2^+ ions are normally dissociated at the surface and they are reflected as single atoms with less than a half energy of the incident H_2^+ ions because the initial incident energy of H_2^+ ions is divided into each fragments. Indeed, the proportion of this component, *i.e.*, correlated to the reciprocal of the degree of dissociation, increased with decreasing discharge power as shown in Fig. 8.4(e). The most outer part (②) of the Doppler-broadened profile at $0.26 \leq |\Delta\lambda| \leq 0.37$ nm for $V_b = -150$ V and $0.37 \leq |\Delta\lambda| \leq 0.52$ nm for $V_b = -300$ V was formed by the reflected energetic atoms produced by the H^+ ion incidence.

8.4.2 Comparison with ACAT Simulation Results

The ACAT code simulates the trajectories of projectiles with the Monte-Carlo method under a binary collision approximation [2]. The excitation processes either in solid or at surface are not taken into account. Figure 8.6(a-b) shows the calculated Hα spectra of hydrogen atoms reflected from a W surface using the ACAT code. The incident energy was set to be 300 eV. The spectra were calculated taking into account the energy and angle distributions of the reflected particles in the unit of wavelength (nm) and convoluted with the instrument function of the monochromator used in the measurements. Figure 8.6(c-d) show the (c) energy and (d) angular distributions of the reflected atoms. The ACAT calculation collected the particles (a) over the entire reflected particle energy and (b) above the energy thresholds indicated in Fig. 8.6(b). Reflected atoms at higher kinetic energy form a broader butterfly-wing shaped component, while low energy atoms contribute to a sharp-central component. As shown in Fig. 8.6(d), the higher energy part of the reflected atoms exhibits a characteristic broad butterfly-wing shaped angular distribution, which contributes to the broad spectral component. It is evident that the tail part of the measured spectra ($0.35 \leq |\Delta\lambda| \leq 0.5$ nm) mainly originates from the reflected hydrogen atoms with higher energy. The ACAT calculation confirmed that the reflected particles

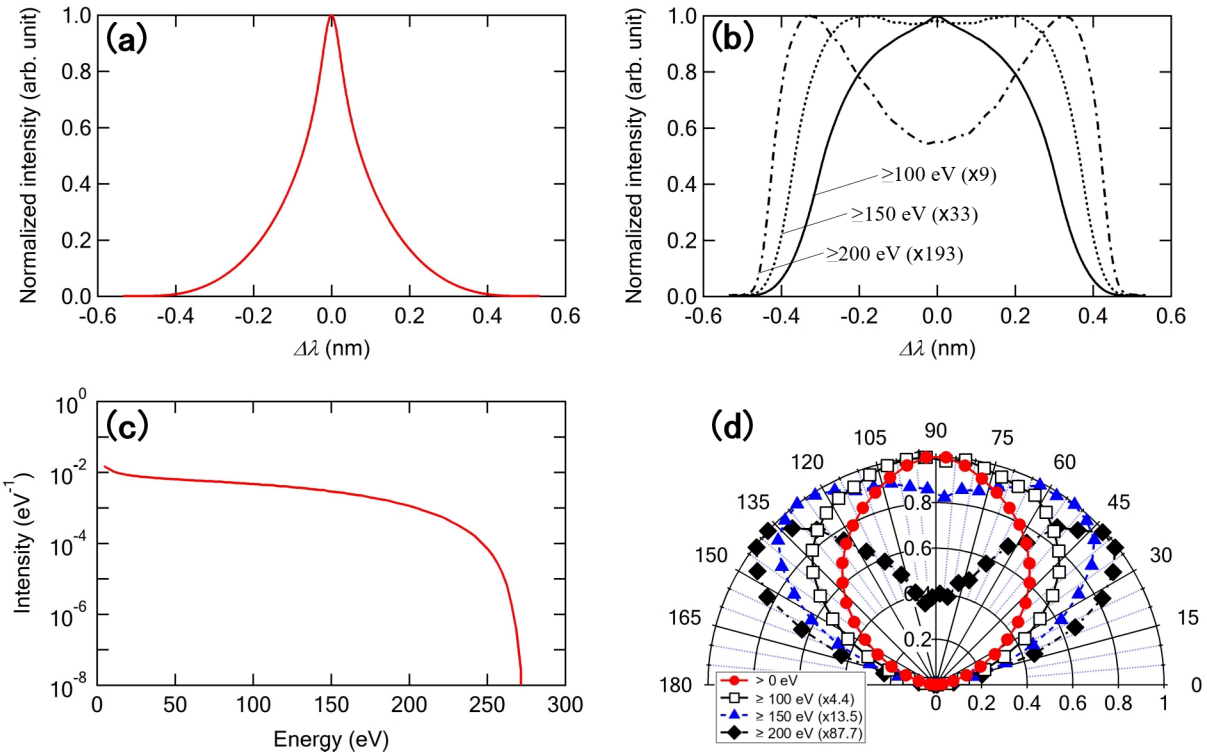

Figure 8.6. (a-b) Reconstructed Hα spectrum for the reflected hydrogen atoms from a W surface based on the calculations using the ACAT code. The incident energy was set to be 300 eV. The spectra were collected (a) over the entire reflected particle energy, $E_r > 0$ eV, and (b) above the energy thresholds of 100, 150 and 200 eV. Each intensity of the spectra is normalized to the peak intensity. (c) The energy and (d) angular distributions of the reflected hydrogen atoms at W surface calculated by the ACAT code. The calculated angular distributions were also collected above several energy thresholds for the reflected atoms corresponding to those for (b) the reconstructed spectra.

with higher reflection energy contribute to the tail broadening of the spectrum as shown in Fig. 8.6(b).

8.4.3 Spatial Distribution of the Doppler-Spectral Intensities

The spatial dependence of the Doppler-spectral intensities (component ② in Fig. 8.5) along the z axis was investigated. The quantitative characterization of the Doppler spectral intensities (component ②) was not straightforward due to the large background of the central peak intensity and the contribution to the broadened component due to the H_2^+ ion incidence. Here, a factor η ($0 < \eta \leq 1$) is introduced to characterize the relative change in the intensity of the contribution of the reflected atoms. η is defined as $\eta = I_z/I_{ref}$, which

is the ratio of the spectral intensity, I_z, at an arbitrary z to that of the reference, I_{ref}. I_{ref} signifies the reference Doppler spectrum measured at $z = 2.8$ mm where the Doppler -spectral intensity of the reflected atoms takes the maximum. In this study, η is calculated by minimizing $\int |i_z(\Delta\lambda) - \eta i_{ref}(\Delta\lambda)| d\Delta\lambda$ for the outer part of the Doppler-broadened component, *i.e.*, $0.26 \leq |\Delta\lambda| \leq 0.37$ nm for $V_b = -150$ V and $0.37 \leq |\Delta\lambda| \leq 0.52$ nm for $V_b = -300$ V, where neither the central peak nor the component of $H_2{}^+$ ion incidence is superimposed and pure contribution from reflected atoms due to H^+ ion incidence appears. Figure 8.7(b) shows the z dependence of η of spectra for $V_b = -150$ and -300 V together with the relative spectral intensity of the background central Hα peak. The intensity of the Doppler-broadened components took the maximum at $z = 2.8$ mm and decreased monotonically as leaving from the target surface, while the background central peak dropped by 91% at the plasma edge at $z = z_1 = 10.6$ mm. No remarkable difference was observed in the spatial distribution for two bias potentials. Figure 8.7(c) shows the ratio of η for $V_b = -300$ V against the relative peak intensity of the background (I_{bg}). The ratio η/I_{bg} increased considerably at $z > z_1$. The contribution from the reflected atoms was observed with the highest signal-to-noise ratio at $z = 15.6$ mm.

Hydrogen atoms in the $n = 3$ level with the kinetic energy of 150 and 300 eV traverse relatively short distance of the order of ∼3.4 and ∼4.8 mm, respectively, with the radiative lifetime of ∼20 ns [8]. On the other hand, the Doppler component of the reflected atoms spread spatially even beyond the plasma periphery. The Doppler component was still observed at $z = 18$ mm with the intensity more than 20% of the maximum value measured at $z = 2.8$ mm. The spatial distributions of η did not differ between two different incident energies of 150 and 300 eV as shown in Fig. 8.7(b). It has been reported that almost none of the reflected atoms were excited to $n \geq 3$ by single-electron transfer from the surface for the hydrogen atoms reflected from a molybdenum surface with velocity of 0.1 a.u. (approximately 250 eV), while approximately 14% of them was initially in the $n = 2$ level and a major part of the rest was in the ground state [7]. Our measured results suggest that the reflected atoms were excited to the $n = 3$ level when traversing plasma or plasma peripheral region after the reflection from the surface. Most of the reflected atoms were

considered to be in the ground state and a part of the reflected atoms of the order of 10% was in the $n = 2$ level just after the bombardment as described above [7]. The latter

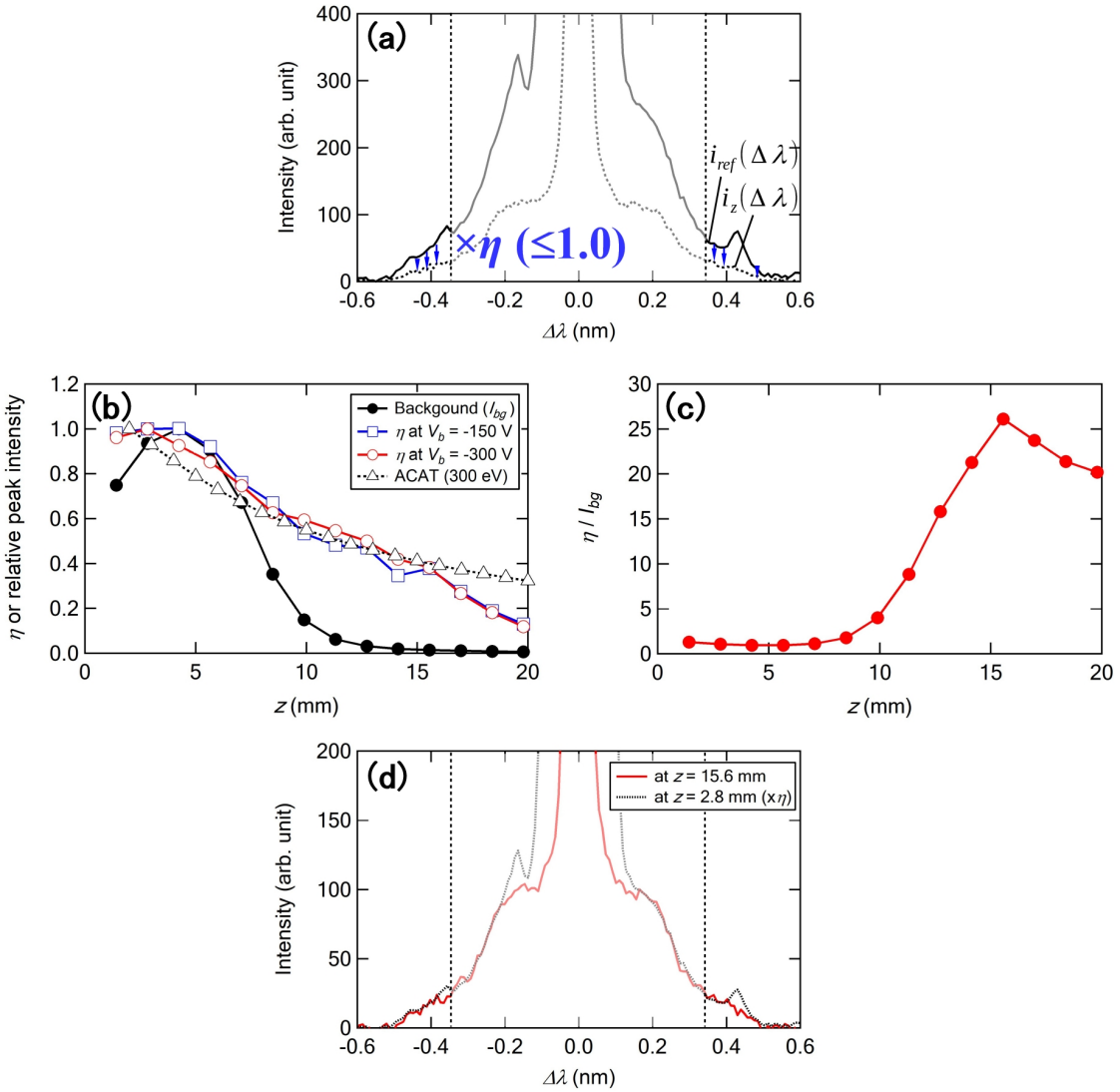

Figure 8.7. (a) A reference spectrum, $i_{ref}(\Delta\lambda)$, with a spectrum, $i_z(\Delta\lambda)$, at given z. The target was biased at $V_b = -300$ V. The intensity of the spectra at z is normalized to the reference spectra by a constant η $(0 < \eta \leq 1)$ so as to minimize $\int |i_z(\Delta\lambda) - \eta i_{ref}(\Delta\lambda)| d\Delta\lambda$ at $|\Delta\lambda| \geq 0.35$ nm. (b) z dependence of η for spectra obtained at bias potential of $V_b = -150$ V (open squares) and -300 V (open circles) on the target together with the relative peak intensity, I_{bg}, of the central background spectra obtained at floating potential (-15 V) on the target (closed squares). The relative intensity of the central background spectra are normalized at $z = 4.2$ mm. The edge position of plasma column is estimated to be $z_1 = 10.6$ mm (see text). The ACAT simulation results are also shown (open triangles). In the simulation, hydrogen atoms at 300 eV were incident onto a W target, and the reflected particles intersecting the assumed view field were recorded with the energy threshold of ≥150 eV. (c) The ratio of η against the relative peak intensity of the background (I_{bg}) at $V_b = -300$ V. (d) Comparison of spectra measured at $z = 15.6$ and 2.8 mm with intensity normalized by η.

atoms in the $n = 2$ level may be excited to the $n = 3$ level by collisions with H_2 molecules or electrons only around the target surface because of the short lifetime of the atoms in the $n = 2$ level. The lifetime of the atoms in the $n = 2$ level is $\sim$3 ns, [8] which is much shorter than that in the $n = 3$ level.

Accordingly, the Hα Doppler-broadened component observed in this study is considered to be resulted mostly from the local excitation of the reflected atoms in the ground state to the $n = 3$ level in plasma or plasma peripheral region. There are two possible mechanisms for the excitation of the reflected atoms to the $n = 3$ level: collisional excitations with electrons or H_2 molecules. Here, the collision with a H_2 molecule is most likely responsible for the excitation of the reflected atoms to the $n = 3$ level considering the shorter mean free path of the collisional excitation with a H_2 molecule than that with an electron. Indeed, contribution of the reflected atoms spatially extended to the plasma peripheral region where very few electrons exist. This result supports our conclusion that the collisions with H_2 molecules excited the reflected atoms to the $n = 3$ level. It is noted that the spectral width and shape of the measured Doppler-broadened component did not exhibit z-dependence at $z < 20$ mm as shown in Fig. 8.7(d). Thus, effects of the momentum transfer from the reflected atoms to H_2 molecules can be considered negligible in these measurements. Actually, the reflected atoms lose a small part of their kinetic energy for their excitation; but this energy loss is also negligible in the examined energy range of several 100 eV, and calculated to be only 12 eV from Eq. 5.2 and 5.3.

The list below shows the estimated mean free path for the collisional excitation with either an electron or a molecule.

- $H^0 + e \rightarrow H^*(n = 3) + e$

  Condition:

  $T_e = 3$ eV, $n_e = 4 \times 10^{11}$ cm^{-3}

  Rate coefficient for the excitation $n = 1 \rightarrow n = 3$:

  $\langle \sigma v_e \rangle = 8.0 \times 10^{-11}$ cm^3/s [9]

  Mean free path for the excitation of a H atom at 300 eV:

  $\lambda_{mfp} = v_H/(n_e \langle \sigma v_e \rangle) = 7.5 \times 10^5$ cm

• $H^0 + H_2 \rightarrow H^*(n = 3) + H_2$

Condition:

$T_{gas} = 300$ K, $n_{gas} = 2.9 \times 10^{14}$ cm^{-3} (1.2 Pa)

a) $n = 1 \rightarrow n =$ 3p+3d

Cross section for the excitation of a H atom at 300 eV:

$\sigma = 7.0 \times 10^{-18}$ cm^2 [10]

Mean free path:

$\lambda_{mfp} = 1/(n_{gas}\sigma) = 493$ cm

b) $n = 1 \rightarrow n =$ 3s

Cross section for the excitation of a H atom at 300 eV:

$\sigma = 3.5 \times 10^{-18}$ cm^2 [10]

Mean free path:

$\lambda_{mfp} = 1/(n_{gas}\sigma) = 986$ cm

The calculated minimum mean free path for the collisional excitation with a H_2 molecule is of the order of 500 cm, while the spatial distribution of the Doppler-spectral intensities, η, indicated a monotonic decrease even in the short distance of $\sim$2 cm. The reflected atoms diverge with broad reflection angles as shown in Fig. 8.6(d). This caused the significant decrease of the reflected particle flux as leaving from the surface, resulting in the monotonic decrease in the Doppler-spectral intensities, η, with increasing z.

The spatial distribution of the Doppler-spectral intensity of the reflected atoms calculated by the ACAT simulation agreed well with the measured result as shown in Fig. 8.7(b). In the calculations, hydrogen atoms at 300 eV were incident onto a W target, where the actual geometries of the ion bombardment and view field of the optical measurements in the experiments shown in Fig. 8.1(c) were taken into account. The simulated spatial distribution shown in Fig. 8.7(b) is plotted as the number of reflected particles which intersected the assumed view field at an arbitrary z, and normalized by the maximum value obtained at $z = 2$ mm. Namely, the number of the reflected particles was simply counted in accordance with the geometrical relations between the assumed view fields and the trajectories of the reflected particles after the ejection from the surface. The

collision process with H_2 molecules after the reflection was not taken into account. For the measured spectra, η was determined at the wavelength corresponding to the energy of the reflected atoms at $\geq$150 eV as shown in Fig. 8.7(a). Therefore, energy threshold was set at $\geq$150 eV for the reflected atoms in the simulation for comparison. The simulation reproduced the experimental results well; the intensity of the reflected particles decreased monotonically with z due to the diverging nature of the reflected atoms.

8.5 Summary

This chapter provided the details on the successful development of an optical spectroscopic measurement technique to investigate the reflection properties of low energy hydrogen particles at a metal surface in a plasma by reducing the large background from the plasma. The velocity component of the reflected atoms along the line of sight contributes to the Doppler broadening of Hα emission spectrum. It has been clarified that the reflected hydrogen atoms contributed to the outermost Doppler-broadened component of the Hα spectra. The Doppler component originating from the reflected atoms spread spatially beyond the region outside of the plasma column as leaving from the W surface. The observation of the spectra at the region outside of the plasma column improved the signal-to-noise ratio of the Doppler component against background from hydrogen atoms in the plasma and also reduced the contribution from the molecular hydrogen to the Doppler component. The collisional excitations with H_2 molecules are proposed to populate the reflected atoms to the $n = 3$ level, contributing to the emissions of the Doppler-broadened Hα spectral component. The developed spectroscopy method to detect the hydrogen atoms reflected from a metal surface presents a good possibility to clarify the recycling of low-energy hydrogen atoms in fusion plasmas.

References

[1] K. Doi, H. Yamaoka, T. Kenmotsu, and M. Wada, "Spectroscopy Study of Hydrogen Atoms Reflected From Tungsten Surface in a Magnetized Plasma," submitted for publication, 2017.

[2] Y. Yamamura, "Dynamical simulations of cascade damage in Cu, Ag and Au," *Nucl. Inst. Methods Phys. Res. B*, vol. 51, no. 4, pp. 407–416, Oct. 1990.

[3] R. S. Freund, J. A. Schiavone, and D. F. Brader, "Dissociative excitation of H_2: Spectral line shapes and electron impact cross sections of the Balmer lines," *J. Chem. Phys.*, vol. 64, no. 3, pp. 1122–1127, Feb. 1976.

[4] H. M. Crosswhite, Ed., *The Hydrogen Molecule Wavelength Tables of Gerhard Heinrich Dieke*, New York: Wiley, 1972.

[5] R. Brako and D. M. Newns, "Theory of electronic processes in atom scattering from surfaces," *Rep. Progr. Phys.*, vol. 52, no. 6, pp. 655–697, Jun. 1989.

[6] T. Tanabe, K. Ohya, and N. Otsuki, "Hydrogen reflection and Hα emission," *J. Nucl. Mater.*, vol. 220-222, pp. 841–845, Apr. 1995.

[7] D. Kato, T. Kenmotsu, K. Ohya, and T. Tanabe, "Excited state distribution of reflected hydrogen atoms at metal surfaces - Development of theoretical models," *J. Nucl. Mater.*, vol. 390-391, no. 1, pp. 498–501, Jun. 2009.

[8] J. R. Hiskes, C. B. Tarter, and D. A. Moody, "Stark Lifetimes for the Hydrogen Atom," *Phys. Rev.*, vol. 133, no. 2A, pp. 424–426, Jan. 1964.

[9] R. K. Janev, W. D. Langer, K. Evans, Jr., and D. E. Post, Jr., *Elementary Processes in Hydrogen-Helium Plasmas*. Berlin, Heidelberg: Spinger-Verlag, 1987.

[10] H. Tawara, Y. Itikawa, Y. Itoh, T. Kato, H. Nishimura, S. Ohtani, H. Takagi, K. Takayanagi, and M. Yoshino, "Atomic data involving hydrogen relevant to edge plasmas," Report IPPJ-AM-46, Institute of Plasma Physics, Nagoya University, 1986.

Chapter 9

Hydrogen Reflection at Helium-Induced W-Fuzz Surface Measured by Doppler Spectroscopy

9.1 Intoductory Remarks

A measurement technique based upon the Doppler spectroscopy of Hα emission spectrum was developed for low energy hydrogen reflection in a plasma. Chapter 8 discussed the methodology on the signal-to-noise enhancement for the weak signal from the reflected atoms by reducing the large background from the plasma. This chapter presents the experimental investigation of the effects of the W-fuzz surface morphology upon the hydrogen particle reflection based on the developed measurement technique. This chapter has also been submitted for publication as Ref. [1].

9.2 Experiment

9.2.1 W-Fuzz Samples

This experiment employed the same W-fuzz samples of which the hydrogen ion reflection property was investigated in Chapter 4. The samples were prepared and provided by Dr.

H T Lee of Osaka University. A 0.3-mm thick polycrystalline W sample (99.95% pure, Nilaco) was exposed to a He plasma for 3000 s. The surface temperature of the W target was maintained at ∼1200 K during the He-plasma bombardment in order to prepare a W-fuzz layer on the surface. The W target was negatively biased at -150 V in the He plasma. The He fluence onto the W target was of the order of 6-9×10^{24} He-particles m^{-2}. Three samples were prepared in the same manner. Photographs and FE-SEM images of the W-fuzz sample are shown in Fig. 9.1. A W-fuzz nanostructure was formed typically in an area of 20 × 12 mm^2 on the W surface as shown in Fig. 9.1(a). The W-fuzz surface appears black due to its low visible light reflectance. The FE-SEM image in Fig. 9.1(b) was observed at 45° from the surface with different magnifications.

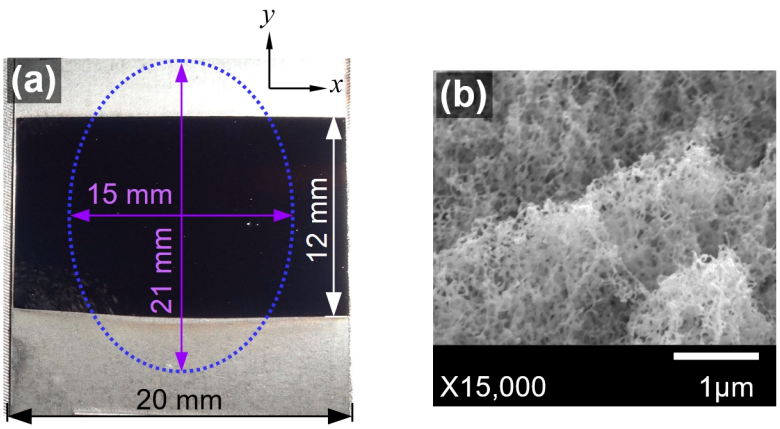

Figure 9.1. (a) A photograph and (b) FE-SEM image of the W-fuzz sample. An ellipse indicated with a dotted line shows the region bombarded by the hydrogen plasma. The FE-SEM image was observed at 45° tilt angle from the surface.

9.2.2 Hydrogen-Plasma Bombardment and Spectroscopic Detection of Reflected Hydrogen Atoms

A prepared W-fuzz samples was attached to a holder in a vacuum chamber and exposed to a magnetized hydrogen plasma. The electromagnet coils form a magnetic field of 28 mT at the center of the vacuum vessel where a linear magnetized plasma of ϕ15 mm in diameter was produced by a hot-cathode discharge. The discharge was kept under the discharge current of $I_2 = 2.0$ A, the applied potentials of $V_2 = 70$ V (140 W) and $V_1 = 70$ V, and the gas pressure of 1.2 Pa (H_2) throughout the measurements. The electron density and

temperature were estimated to be $n_e = 4 \times 10^{11}$ cm^{-3} and 3.0 eV, respectively, from the Langmuir probe measurement. The plasma potential tanged from 0 to 0.5 V, depending on the target bias potential.

The W-fuzz sample was fixed on a water-cooled target holder for plasma bombardment. The angle of the surface normal to the target was set at 45° from the magnetic force lines by using *Target Holder 2* (refer to Chapter 8 for target holders). Figure 9.2 shows a photograph of the W-fuzz sample under the hydrogen-plasma bombardment together with a schematic drawing of the line of sight set on the z axis. The center of the W-fuzz sample was aligned to the central axis of the ϕ15-mm plasma column for the bombardment. The region of the W-fuzz target bombarded by the hydrogen plasma is illustrated as dotted ellipse in Fig. 9.1(a). A negative bias was applied onto the target to control the incident energy of atomic and molecular hydrogen ions from the plasma onto the sample. Plasma raised the sample temperature up to ∼920 K.

The Hα emission spectrum was measured using a monochromator with the resolution of 23 pm. The line of sight observed the axis parallel to the target surface which was drawn through $z = 17$ mm, outside of the plasma column, for the enhanced signal-to-noise ratio measurement. Here, the z-axis was defined to be perpendicular to the surface at the center of the W-fuzz target (see Fig. 9.2(b)). This line of sight observed symmetrically Doppler-broadened spectra due to the energetic atoms reflected from the W-fuzz surface. Usually, the weak Doppler-broadened signal of the reflected atoms cannot be measured

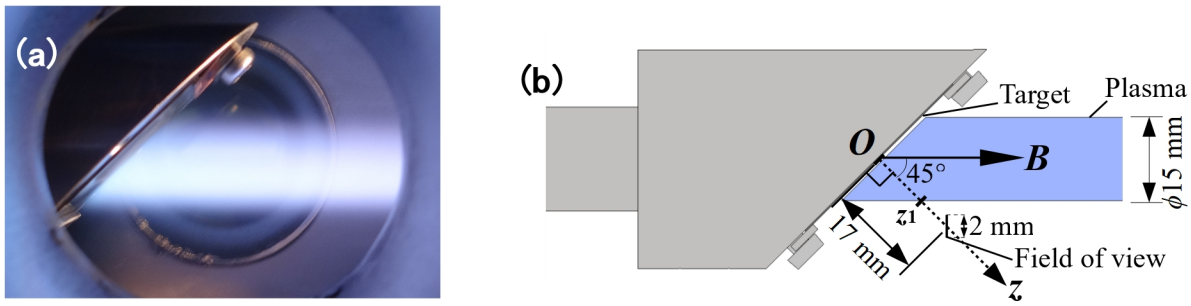

Figure 9.2. (a) A photograph of the W-fuzz sample under the hydrogen-plasma bombardment together with (b) a schematic drawing of the line of sight set on the z axis. The line of sight was set parallel to the target surface and fixed at $z = 17$ mm throughout measurements. The monochromator viewed an area of 2 mm height × 30 μm width.

with enough signal-to-noise ratio in a plasma environment, because the high intensity of the central peak saturates the detector. However, the intense central peak could be reduced remarkably by setting the observation line of sight in a region outside the plasma where $z > z_1$ in Fig. 9.1(b). This observation line of sight allows us to detect the spectral component mainly composed of the reflected atoms with enough signal-to-noise ratio by reducing the large background emission of the central plasma as discussed in Chapter 8.

This study originally aimed at quantification of the particle reflection coefficient of the W-fuzz surface at energy range less than 300 eV. However, the W-fuzz layer was expected to be gradually destructed during the hydrogen-plasma bombardment [2, 3, 4]. Therefore, in this study, the time evolution of the Doppler spectra from the reflected atoms was investigated. The Doppler spectroscopy is advantageous for investigating the time dependent changes in reflection yields because it can be expected that the intensity of the Doppler-broadened spectra strongly depends on the surface conditions. Indeed, the W-fuzz surface remarkably reduced the hydrogen ion reflection coefficient as discussed in Chapter 4. An actively-cooled CCD detector continuously recorded 99 spectra during 2450 s. The exposure time of each spectrum was 25 s. The time sequence of the measurement is illustrated in Fig. 9.3. The discharge was stabilized for 90 s before starting the continuous spectroscopy measurement.

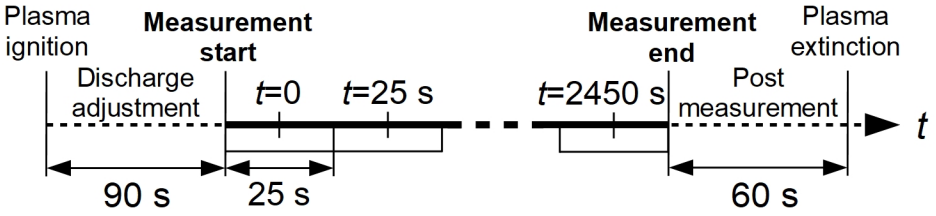

Figure 9.3. The time sequence of the Doppler-spectroscopic measurement for the hydrogen reflection at W-fuzz surface under the plasma bombardment.

9.3 Results and Discussion

9.3.1 Measured Hα Spectra

Figure 9.4 shows spectra measured at $z = 17$ mm vertically away from the W-fuzz sample surface biased at (a) $V_b = -200$ and (b) -300 V. The spectra at $t = 0$ and 2450 s are shown as dotted and solid lines, respectively. The intensities are normalized to that of the central peak, where thicker lines represent the expanded views to see the Doppler-broadened components originating from the reflected atoms. Bell-shaped components were observed at the bottom of the background central peak in the wavelength regions of $|\Delta\lambda| \leq 0.43$ nm at $V_b = -200$ V and $|\Delta\lambda| \leq 0.52$ nm at $V_b = -300$ V. As discussed in Chapter 8, the inner part of the bell-shaped component, *i.e.*, at $|\Delta\lambda| \leq 0.30$ nm for $V_b = -200$ V and at $|\Delta\lambda| \leq 0.37$ nm for $V_b = -300$ V, is considered to originate from the reflected atoms produced by H_2^+ ion incidence. The H_2^+ ions were separated once they enter the surface and reflected as single atoms with less than one half energy of the incident H_2^+ ions because the energy was divided into each of the fragments [5]. It has been clarified that the most outer part of the Doppler-broadened profile, *i.e.*, at $0.30 \leq |\Delta\lambda| \leq 0.43$ nm for $V_b = -200$ V and at $0.37 \leq |\Delta\lambda| \leq 0.52$ nm for $V_b = -300$ V, is formed by the reflected energetic atoms of the H^+ ion incidence. The intensity of the Doppler component from the reflected atoms increased with time during the plasma bombardment at both

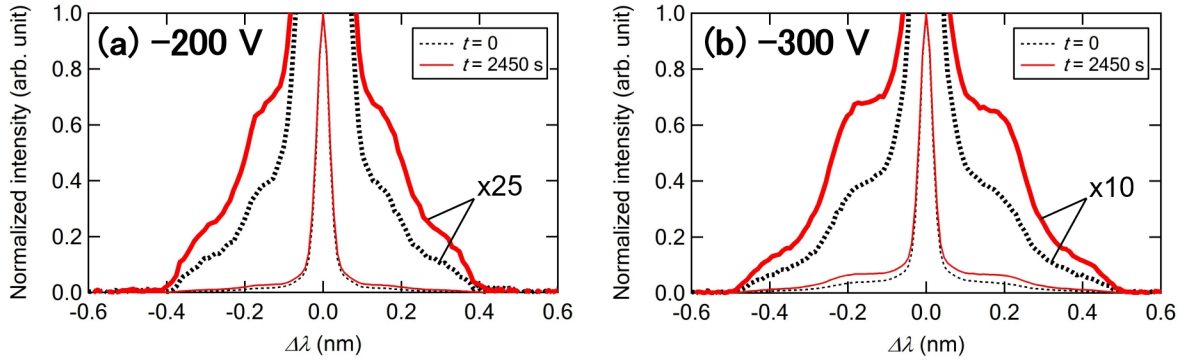

Figure 9.4. Doppler-broadened spectra of Hα emission measured at $z = 17$ mm from the W-fuzz surface biased at (a) $V_b = -200$ and (b) -300 V. The thicker lines represent the expanded views to see the bottom of the spectra where the contribution from the reflected atoms appeared. Spectra measured at $t = 0$ and $t = 2450$ s are shown. The signal integration time was 25 s.

$V_b = -200$ and -300 V, while no remarkable change in the spectral shape and width was observed.

9.3.2 Time Evolution of Spectral Intensity and W-fuzz Layer Destruction

The time evolution of intensity of the outer part of the Doppler-broadened component, *e.g.*, at $0.30 \leq |\Delta\lambda| \leq 0.43$ nm for $V_b = -200$ V and at $0.37 \leq |\Delta\lambda| \leq 0.52$ nm for $V_b = -300$ V, is shown in Fig.9.5 for the W-fuzz sample biased at $V_b = -200$, -250 and -300 V. The characterization of the intensities of the Doppler component purely contributed from the reflected atoms of H^+ ion incidence is not straightforward due to

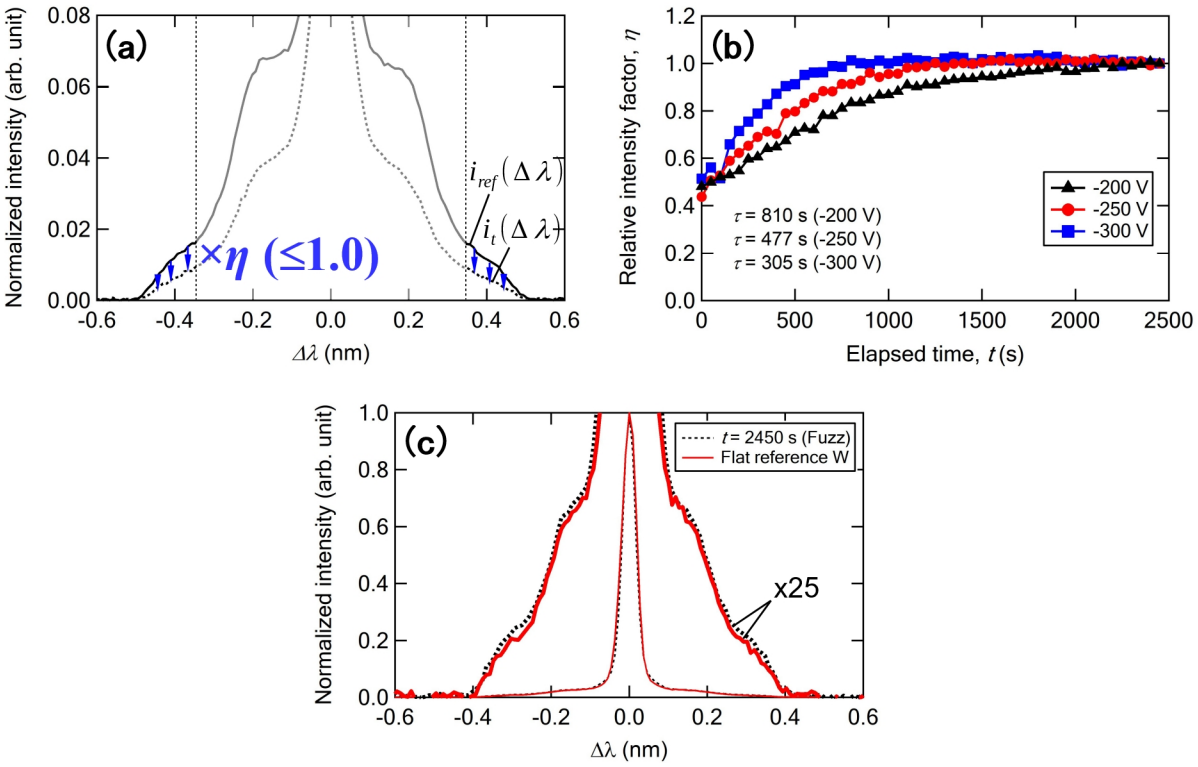

Figure 9.5. (a) A reference spectrum $i_{ref}(\Delta\lambda)$ measured at $t = 2450$ s with a spectrum $i_t(\Delta\lambda)$ measured at an arbitrary t (s). The W-fuzz target was biased at $V_b = -300$ V in the plasma. A factor η $(0 < \eta \leq 1)$ is introduced to characterize the contribution from the reflected atoms. The factor η is defined so as to minimize $\int |i_t(\Delta\lambda) - \eta i_{ref}(\Delta\lambda)| d\Delta\lambda$ at $|\Delta\lambda| \geq 0.37$ nm for $V - b = -300$ V. (b) The time evolution of the factor η for spectra measured at $V_b = -200$, -250 and -300 V. (c) Comparison of spectral profiles: $i_{ref}(\Delta\lambda)$, the spectrum measured at $t = 2450$ s, for $V_b = -200$ V and a spectrum measured for a flat reference W at $V_b = -200$ V.

the remaining larger intensity of the central peak and inner Doppler component produced by H_2^+ ion incidence. Here, a factor η ($0 < \eta \leq 1$) is introduced to characterize the relative change in the contribution from reflected atoms for the outer part of the Doppler component. η is defined as $\eta = I_t/I_{ref}$, which is the ratio of the spectral intensity, I_t, at an arbitrary t to that of the reference, I_{ref}. The coefficient η was calculated by minimizing $\int |i_t(\Delta\lambda) - \eta i_{ref}(\Delta\lambda)| d\Delta\lambda$ for the outer part of the Doppler component, *e.g.,* at $|\Delta\lambda| \geq 0.37$ nm for $V_b = -300$ V as shown in Fig. 9.5(a). Neither the central peak nor the component of H_2^+ ion incidence is superimposed, and pure contribution from reflected atoms due to H^+ incidence appears in the tail regions at $|\Delta\lambda| \geq 0.37$ nm for $V - b = -300$ V. The spectrum at $t = 2450$ s was used as a reference (I_{ref}). Both I_t and I_{ref} were normalized to the central peak intensity to obtain η.

The factor η increased and saturated exponentially with time during the hydrogen-plasma bombardment, indicating the increase of the contribution from the reflected atoms. The initial values of the factor η were approximately 0.5 for all bias potentials. The time evolution of η can be fitted with an exponential function. The time constants were estimated to be 305, 477, and 810 s for $V_b = -300$, -250, and -200 V, respectively, from the exponential function fittings. The time constants of the growth rate are smaller as the absolute value of target bias is higher; the contribution from the reflected atoms in the Hα spectrum increased to the asymptotic line more quickly at higher incident particle energy. It is known that the particle reflection coefficient of the incident ions in the fuzz surface was smaller than that of the flat W surface as discussed in Chapter 4. Therefore, the increase of the reflected hydrogen intensity indicates the removal of the fuzz surface structure. The intensity of the reflected hydrogen atoms from the W-fuzz sample for the incident particle energy less than 300 eV is about one half of the flat W surface following plasma-induced destruction of the fuzz layer. Non-significant change in the spectral shapes and widths suggests that the velocity distribution of the reflected atoms was not affected largely by the surface morphology.

One has to note that the hydrogen ions were incident onto the surface with the energy lower than the sputtering threshold for W. The threshold of the sputtering for W at

normal incidence of hydrogen was estimated to be 443 eV [6], and the incident angle dependence was small [7]. But the measured time evolution of intensity of the reflected hydrogen atoms suggests that the destruction of the W-fuzz structure occurred, and the resultant flat surface increased the particle reflection coefficient of the hydrogen atoms during the hydrogen-plasma bombardment, where the incident H^+ ion senergy was less than 300 eV. Indeed, the destruction of the W-fuzz structure has been confirmed in the FE-SEM images of the target surfaces after the hydrogen-plasma bombardment as shown in Fig. 9.6. Microstructures remained on the surface even after the hydrogen-plasma bombardment especially for lower incident energy cases at $V_b = -200$ and -250 V. The surface temperature under the magnetized plasma bombardment can be raised up to the level where the annealing effect on the W-fuzz layer takes place [4]. Normally, the plasma bombardment of a flat reference W using the magnetized plasma at the 140 W discharge power raises the surface temperature to ∼1030, ∼960 and ∼920 K for $V_b = -300$, -250

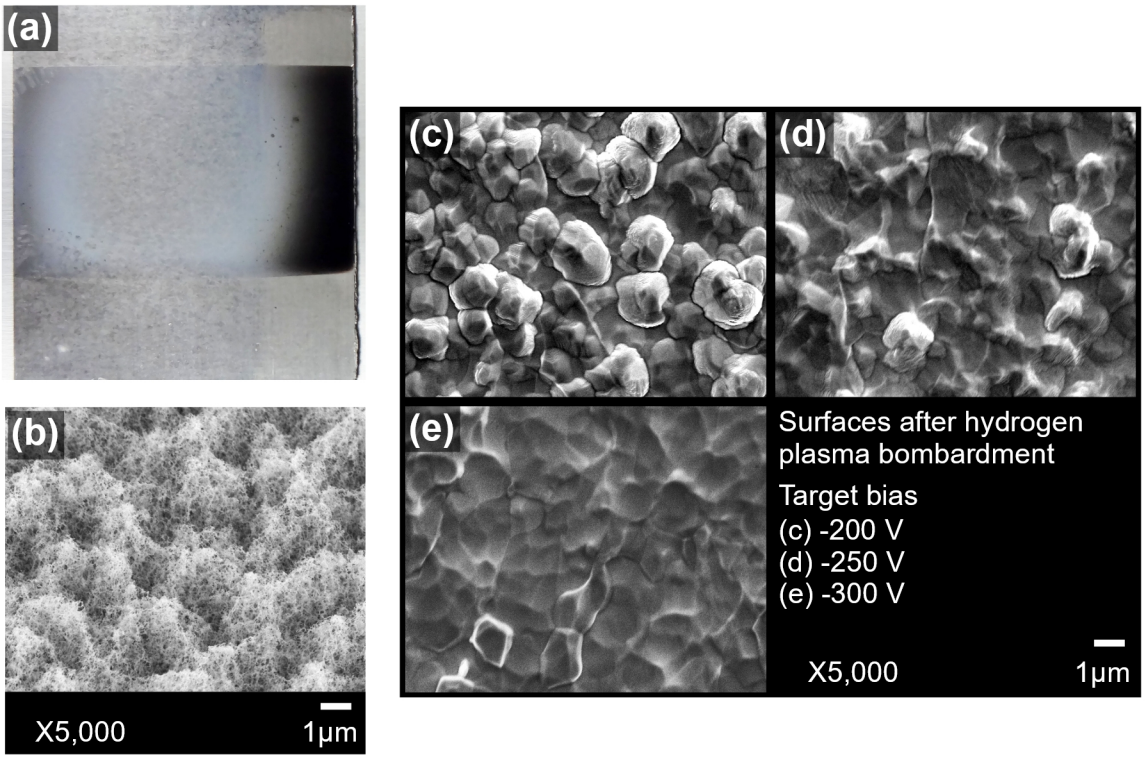

Figure 9.6. (a) A photograph of the W-fuzz sample after the hydrogen-plasma bombardment. (b) A FE-SEM image of the W-fuzz sample before the hydrogen-plasma bombardment observed at 45° tilt angle from the surface. (c-e) FE-SEM images of the W-fuzz samples after the hydrogen-plasma bombardment at different target bias potentials of (c) $V = -200$, (d) -250 and (e) -300 V. The total time of the hydrogen-plasma bombardment was approximately 2600 s.

and −200 V, respectively. The surface temperatures of the W-fuzz targets were also measured using a pyrometer which indicated 890, 916 and 920 at $V_b = -300$, −250 and −200 V, respectively, where the emittance was set at the value of bulk W, *i.e.,* 0.43 at 0.65 μm. However, accurate temperatures were not obtained because of the unknown emittance of the W-fuzz. The accumulation or resolidification of the agglomerated nanostructures due to the annealing effect most likely occurred on the surface as reported in Ref. [4], and contributed to the W-fuzz destruction.

Again, the intensity of the reflected atoms from the W-fuzz sample was about one half of the flat-W surface following plasma-induced destruction of the fuzz surface structure. Although the microscale structures remained on the surface for lower incident energy cases especially at $V_b = -200$ V, the spectral intensity originating from the reflected atoms reached the same level of that measured for an intrinsically flat reference W as shown in Fig. 9.5(c). This fact suggests that the remaining surface microstructures do not affect significantly on the particle reflection coefficient.

The angular and velocity distributions of the reflected atoms can also change following the rearrangement of the surface conditions during the hydrogen-plasma bombardment. Previously, the angular distribution of surface reflected H^+ ions at 1 keV incident energy was indeed found broader in case of W-fuzz surface compared to a flat W as discussed in Chapter 4. However, no change in the spectral width and shape appeared for the outermost Doppler-broadened component, *e.g.*, at $|\Delta\lambda| \geq 0.37$ nm for $V_b = -300$ V. It has to be noted that the monochromator observed the Doppler-broadened components mirrored by the velocity distributions of the reflected atoms along the line of sight of the optical measurements. The velocity components of the reflected atoms along the line of sight are determined by both angular and velocity distributions. Assuming that no significant change in the angular and velocity distributions of the reflected atoms was caused due to the different surface conditions following the destruction of the fuzz surface structure, the relative change in the particle reflection coefficient was characterized from the comparison of the Doppler-spectral intensities.

9.4 Summary

The time evolution of intensity of the Doppler-broadened Hα spectra emitted by hydrogen atoms reflected from the W-fuzz was investigated under hydrogen-plasma bombardment. The spectral intensity increased and saturated exponentially during the plasma bombardment. The destruction of the fuzz structure was confirmed by post bombardment sample characterization by FE-SEM. The results indicate that the destruction of the porous fuzz surface caused the increase of the particle reflection coefficient of the hydrogen atoms during the plasma bombardment. The contribution of the reflected atoms in Hα emission for the W-fuzz was reduced to be 50% of that for the flat W after the fuzz layer annihilation. This suggests that the formation of the W-fuzz layer reduces the particle reflection coefficient in the low incident energy range below 300 eV. While absolute values of the particle reflection coefficient are required as inputs for quantitative modeling studies, the magnitude of the observed relative change ($\sim$50%) in the hydrogen particle reflection coefficient due to the W-fuzz surface structure can be useful information in sensitivity studies to estimate the effects of nanostructured W surface upon the divertor plasma condition. The results suggest that it is easy to remove the W-Fuzz layer from the W surface in a hydrogen plasma. Further study may also be required to investigate an additional effect such as the change in the sputtering yield following the annealing of the W-fuzz layer.

References

[1] K. Doi, H. T. Lee, N. Tanaka, H. Yamaoka, Y. Ueda, and M. Wada, "Spectroscopic study of hydrogen reflection at modified tungsten surface," submitted for publication, 2017.

[2] Y. Ueda, K. Miyata, Y. Ohtsuka, H. T. Lee, M. Fukumoto, S. Brezinsek, J. W. Coenen, A. Kreter, A. Litnovsky, V. Philipps, B. Schweer, G. Sergienko, T. Hirai, A. Taguchi, Y. Torikai, K. Sugiyama, T. Tanabe, S. Kajita, and N. Ohno, "Exposure of tungsten nano-structure to TEXTOR edge plasma," *J. Nucl. Mater.*, vol. 415, pp. S92–S95, Aug. 2011.

[3] D. Hwangbo, S. Kawaguchi, S. Kajita, and N. Ohno, "Erosion of nanostructured tungsten by laser ablation, sputtering and arcing," *Nucl. Mater. Energy*, vol. 12, pp. 386–391, Aug. 2017.

[4] S. Kajita, N. Yoshida, R. Yoshihara, N. Ohno, T. Yokochi, M. Tokitani, and S. Takamura, "TEM analysis of high temperature annealed W nanostructure surfaces," *J. Nucl. Mater.*, vol. 421, no. 1–3, pp. 22–27, Feb. 2012.

[5] S. Kato, N. Tanaka, M. Sasao, M. Kisaki, K. Tsumori, M. Nishiura, Y. Matsumoto, T. Kenmotsu, M. Wada, and H. Yamaoka, "Angle-resolved intensity and energy distributions of positive and negative hydrogen ions released from tungsten surface by molecular hydrogen ion impact," *J. Nucl. Mater.*, vol. 463, pp. 351–354, Aug. 2015.

[6] W. Eckstein, J. Bohdansky, and J. Roth, "Physical sputtering," in *Atomic and Plasma-Material Interaction Data for Fusion, vol.1 (Supplement to journal Nuclear Fusion)*, R. K. Janev, Ed., Vienna: IAEA, Sep. 1991, pp. 51–61.

[7] W. Eckstein, C. Garciá-Rosales, J. Roth, and J. László, "Threshold energy for sputtering and its dependence on angle of incidence," *Nuclear Inst. and Methods in Physics Research, B*, vol. 83, no. 1–2. pp. 95–109, Oct. 1993.

Chapter 10

Conclusions

Hydrogen particle reflection property at the divertor plates determines the overall fusion reactor operational performance. In this study, effects of the He-induced W surface morphologies upon the particle reflection were experimentally investigated. The particle method using an ion beam based test stand apparatus clarified that a nanostructured W-fuzz surface remarkably reduces the particle reflection coefficient of incident H^+ ions at the incident particle energy of 1 keV. The H^+ ion reflection yield for a W-fuzz sample was of the order of 1/3 of that for a flat reference W.

The particle method can be applied only to the measurement of reflected ion properties at relatively high particle energy due to the difficulty in the low energy ion beam transport. On the other hand, the experimental characterizations of the reflected neutral particles at lower incident energy are required because most of the particles incident onto the divertor are backscattered as neutral atoms with their incident energy less than a few 100 eV. The properties of particles reflected at a plasma-facing wall as neutral atoms need to be investigated in lower particle energy region.

In this study, a Doppler-spectroscopic measurement technique for low energy hydrogen atoms reflected from a metal surface under a plasma bombardment was successfully developed with the significant reduction in background signals from the plasma. The most outer component of the Doppler-broadened Hα emission spectra was clarified to originate from the energetic atoms produced by surface reflection at a W surface under the plasma bombardment with negative target bias. The observation at the region outside of

the plasma column dramatically enhanced the signal-to-noise ratio by reducing the large background due to the plasma excitations. While the contribution from the reflected atoms accounted for only less than 1% of the background intensity with the line of sight in the plasma, the proportion of the contribution from the reflected atoms against the background was enhanced to 10%, approximately, at the plasma-peripheral region. Collisions with local H_2 molecules are proposed to excite the energetic atoms reflected from the W surface to the $n = 3$ level and to contribute to the sufficiently maintained signal intensity of the reflected atoms even beyond the plasma peripheral region. The developed technique may put an advantage to measure the property of hydrogen reflection including the velocity distribution of the reflected particles in the incident H^+ ion energy range below several 100 eV, which is indispensable for the prediction of fusion plasma fundamental processes including hydrogen recycling and plasma-boundary processes.

The developed measurement technique was applied to the investigation of effects upon the hydrogen reflection properties due to the He-induced W-fuzz surface morphology. The continuous hydrogen plasma bombardment resulted in the removal of the fuzz layer. The time evolution of the Doppler-spectral intensity originating from the reflected atoms exhibited an increase of the hydrogen particle reflection coefficient correlated to the continuous removal of the fuzz layer. The particle reflection coefficient of the W-fuzz surface was approximately one half of that of the flat surface after the fuzz layer removal in the incident particle energy range of 200 - 300 eV. There was no significant change observed in the spectral shapes and widths in the contribution from the reflected atoms, indicating that the effects on the velocity distribution of the reflected atoms due to the W-fuzz surface are negligibly small. In this study, the relative change in the particle reflection coefficient due to W-fuzz surface was investigated. While the reflection coefficient data in the absolute unit are required as input for the quantitative modeling studies, the obtained relative information is also useful to estimate the absolute value from available literature data. For example, it is known that the particle reflection coefficient of hydrogen at normal incidence onto W target is $\sim$0.6 at the incident particle energy of 300 eV (refer to Fig. 2.4 about the reflection coefficients calculated by W Eckstein). Considering the observed

relative change, the particle reflection coefficient of hydrogen atoms for the W-fuzz sample is estimated to be $\sim$0.3. This estimation can be useful for sensitivity studies to address the impact on the fusion plasma fundamental processes due to the formation of W-fuzz surface structure on the divertor surface.